

1-1-2005

Uncertainty analysis of radionuclide transport in the unsaturated zone at Yucca Mountain

Feng Pan

University of Nevada, Las Vegas

Follow this and additional works at: <https://digitalscholarship.unlv.edu/rtds>

Repository Citation

Pan, Feng, "Uncertainty analysis of radionuclide transport in the unsaturated zone at Yucca Mountain" (2005). *UNLV Retrospective Theses & Dissertations*. 1847.

<http://dx.doi.org/10.25669/kmm9-9bco>

This Thesis is protected by copyright and/or related rights. It has been brought to you by Digital Scholarship@UNLV with permission from the rights-holder(s). You are free to use this Thesis in any way that is permitted by the copyright and related rights legislation that applies to your use. For other uses you need to obtain permission from the rights-holder(s) directly, unless additional rights are indicated by a Creative Commons license in the record and/or on the work itself.

This Thesis has been accepted for inclusion in UNLV Retrospective Theses & Dissertations by an authorized administrator of Digital Scholarship@UNLV. For more information, please contact digitalscholarship@unlv.edu.

UNCERTAINTY ANALYSIS OF RADIONUCLIDE TRANSPORT
IN THE UNSATURATED ZONE AT YUCCA MOUNTAIN

by

Feng Pan

Bachelor of Engineering
Sichuan University, China
2000

A thesis submitted in partial fulfillment
of the requirements for the

Master of Science in Water Resource Management
Water Resource Management Program
College of Sciences

Graduate College
University of Nevada, Las Vegas
August 2005

UMI Number: 1429721

INFORMATION TO USERS

The quality of this reproduction is dependent upon the quality of the copy submitted. Broken or indistinct print, colored or poor quality illustrations and photographs, print bleed-through, substandard margins, and improper alignment can adversely affect reproduction.

In the unlikely event that the author did not send a complete manuscript and there are missing pages, these will be noted. Also, if unauthorized copyright material had to be removed, a note will indicate the deletion.

UMI[®]

UMI Microform 1429721

Copyright 2006 by ProQuest Information and Learning Company.

All rights reserved. This microform edition is protected against unauthorized copying under Title 17, United States Code.

ProQuest Information and Learning Company
300 North Zeeb Road
P.O. Box 1346
Ann Arbor, MI 48106-1346



Thesis Approval

The Graduate College
University of Nevada, Las Vegas

July 28, 2005

The Thesis prepared by

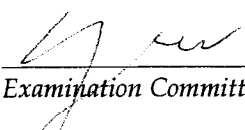
Feng Pan

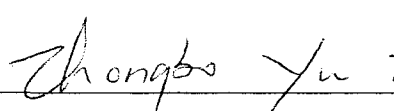
Entitled

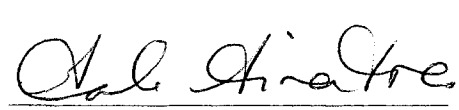
Uncertainty Analysis of Radionuclide Transport in the Unsaturated Zone
at Yucca Mountain

is approved in partial fulfillment of the requirements for the degree of

Master of Science in Water Resource Management.

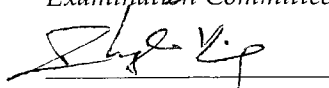
 7/28/05
Examination Committee Co-Chair

 7/28/05
Examination Committee Chair


Dean of the Graduate College

Examination Committee Member

 7/28/05
Examination Committee Member

 7/28/05
Graduate College Faculty Representative

ABSTRACT

Uncertainty Analysis of Radionuclide Transport in the Unsaturated Zone at Yucca Mountain

by

Feng Pan

Dr. Zhongbo Yu, Examination Committee Chair
Associate Professor of Hydrogeology
University of Nevada, Las Vegas

Dr. Ming Ye, Examination Committee Co-Chair
Assistant Professor of Hydrologic Science
Desert Research Institute

This study assessed parametric uncertainty of flow and transport parameters of the unsaturated zone at Yucca Mountain and its propagation in unsaturated flow and radionuclide transport using the Monte Carlo method. The random fields of hydraulic parameters (matrix porosity, permeability and sorption coefficient) were generated using the Latin Hypercube Sampling (LHS) method and used as inputs to a three-dimensional flow and transport code, TOUGH2 developed by the Lawrence Berkeley National Laboratory. By running TOUGH2 for multiple parameter realizations, means, variances, 5% and 95% percentiles of flow and radionuclide transport simulations were estimated to quantify the optimum predictions and associated predictive uncertainty. The results indicated that the parameter uncertainty in matrix porosity, permeability and sorption

coefficient had significant influences on the simulated groundwater flow and radionuclide transport in the unsaturated zone at Yucca Mountain.

TABLE OF CONTENTS

ABSTRACT.....	iii
LISTS OF TABLES.....	vii
LISTS OF FIGURES	viii
ACKNOWLEDGMENTS	xi
CHAPTER 1 INTRODUCTION	1
1.1 Introduction and Literature Review	1
1.2 Objective and Scope	10
1.3 Study Site	10
CHAPTER 2 RANDOM FIELD GENERATION OF HYDRAULIC PARAMETERS	15
2.1. Introduction.....	15
2.2 Determination of Hydraulic Parameter Distributions	17
2.2.1 Data Transformation and Lilliefors Test.....	17
2.2.2 Transformation and Distribution of Matrix Porosity	20
2.2.3 Transformation and Distribution of Matrix Saturated Hydraulic Conductivity	30
2.2.4 Transformation and Distribution of Matrix Sorption Coefficient.....	37
2.3 Random Field Generation of Hydraulic Parameters	40
2.3.1 Latin Hypercube Sampling	40
2.3.2 Random Field Generation of Hydraulic Parameters	42
2.3.2.1 Random Field Generation of Matrix Porosity	44
2.3.2.2 Random Field Generation of Matrix Permeability	48
2.3.2.3 Random Field Generation of Sorption Coefficient.....	53
2.3.2.4 Comparison of Multiple Random Fields.....	54
CHAPTER 3 UNCERTAINTY ANALYSIS OF UNSATURATED FLOW FIELDS...	57
3.1 Introduction.....	57
3.2 Procedures of Monte Carlo Flow Simulation	58
3.3 Results Analysis.....	59
3.3.1 Convergence of Monte Carlo Simulation	59
3.3.2 Comparisons of Simulated and Measured Data.....	65
3.3.3 Uncertainty Analysis of Unsaturated Flow Fields	68
CHPATER 4 UNCERTAINTY ANALYSIS OF RADIONULCIDE TRANSPORT IN THE UNSATURATED ZONE.....	79
4.1 Introduction.....	79
4.2 Simulation Procedure and Transport Parameters.....	80

4.3 Results Analysis.....	81
4.3.1 Convergence Analysis of Monte Carlo Simulation	81
4.3.2 Uncertainty Analysis of Transport Simulation	90
CHAPTER 5 CONCLUSIONS	107
APPENDIX A METHODOLOGY OF FLOW AND TRANSPORT SIMULATIONS	110
A.1 Convergence Analysis of Monte Carlo Simulation	110
A.2 TOUGH2.....	112
A.2.1 EOS9 Module.....	112
A.2.2 T2R3D Module	115
A.2.3 Numerical Scheme	118
REFERENCES	122
VITA.....	128

LISTS OF TABLES

Table 1.1	Lithostratigraphy used in geological framework model, unsaturated zone model layer, and hydrogeological unit correlation used in this thesis (Wu et al., 2004a).....	13
Table 2.1	Descriptive statistics for matrix porosity and saturated hydraulic conductivity.	22
Table 2.2	Statistical parameters of matrix porosity for distribution approximation.....	23
Table 2.3	Statistical parameters of matrix saturated hydraulic conductivity for distribution approximation.....	32
Table 2.4	Descriptive statistics for sorption coefficient of neptunium.	38
Table 2.5	Statistical parameters of sorption coefficient of neptunium for distribution approximation.	38
Table 2.6	Spearman rank correlation between transformed data of matrix porosity and saturated conductivity.	44
Table 2.7	Percentiles of measured and generated data of matrix porosity.	46
Table 2.8	Percentiles of measured and generated data of log permeability.....	52
Table 2.9	Percentiles of measured and generated data of sorption coefficient.....	53

LISTS OF FIGURES

Figure 1.1	Study area of the unsaturated zone at Yucca Mountain (Wu et al., 2004a)...	12
Figure 1.2	A typical cross section of geological profile at Yucca Mountain (Wu et al., 2004a).	12
Figure 2.1	Histograms of measured and generated data of matrix porosity for each model layer.	24
Figure 2.2	Empirical and theoretical distributions for transformed porosity in each model layer.	28
Figure 2.3	Histograms of measured and generated data of matrix log permeability for some model layers.	33
Figure 2.4	Empirical and theoretical distributions for transformed saturated conductivity in each model layer.	35
Figure 2.5	Histograms of measured and generated data of sorption coefficient of neptunium for devitrified, vitric and zeolitic tuffs.....	39
Figure 2.6	Empirical and theoretical distributions for transformed sorption coefficient of neptunium in Devitrified, Vitric and Zeolitic tuffs.....	39
Figure 2.7	Q-Q plot of matrix porosity for measured and generated porosity in some layers.	45
Figure 2.8	Comparison of measured data (Mean, Minimum and Maximum) and generated data (Mean, Minimum and Maximum) and model input data of Wu et al. (2004a) for Thermal domain of matrix log permeability in each model layer (Layer numbers from 1 to 39 represent the model layers shown in Table 1.1).	49
Figure 2.9	Q-Q plot of measured and generated matrix log permeability in some layers.	51
Figure 2.10	Q-Q plot of measured and generated sorption coefficient (K_d) for the three rock types.....	54
Figure 2.11	Histograms of generated random fields of matrix porosity with 100, 200, 500 and 1000 realizations in few layers.	55
Figure 2.12	Histograms of generated random fields of matrix saturated conductivity with 100, 200, 500 and 1000 realizations in few layers.	56
Figure 3.1	Sample mean and variance of simulated water saturation with 95% confidence interval at PTn bottom, Repository layer (TLL) and PV3 layer for three-dimensional domain.	62
Figure 3.2	Sample mean and variance of simulated capillary pressure with 95% confidence interval at PTn bottom, Repository layer (TLL) and PV3 layer for three-dimensional domain.	63
Figure 3.3	Sample mean and variance of simulated matrix vertical flux with 95% confidence interval at PTn bottom, Repository layer (TLL) and PV3 layer for three-dimensional domain.	64

Figure 3.4	Comparison to the simulated and observed matrix saturation for Borehole UZ-14 in three-dimensional domain.....	66
Figure 3.5	Comparison to the simulated and observed matrix saturation for Borehole SD-12 in three-dimensional domain.....	66
Figure 3.6	Comparison to the simulated and observed matrix saturation for Borehole SD-7 in three-dimension domain.....	67
Figure 3.7	Comparison to the simulated and observed Water Potentials for Borehole SD-12 in three-dimension domain.	67
Figure 3.8	Plan view of net infiltration distributed over the 3-D domain.....	69
Figure 3.9	Mean of simulated percolation fluxes at PTn Bottom for the 3-D domain. ..	72
Figure 3.10	Variance of simulated percolation fluxes at PTn Bottom for the 3-D domain.	73
Figure 3.11	5% percentile of simulated percolation fluxes at PTn Bottom for the 3-D domain.	73
Figure 3.12	95% percentile of simulated percolation fluxes at PTn Bottom for the 3-D domain.	74
Figure 3.13	Mean of simulated percolation fluxes at Repository level for the 3-D domain.	74
Figure 3.14	Variance of simulated percolation fluxes at Repository level for 3-D domain.	75
Figure 3.15	5% percentile of simulated percolation fluxes at Repository level for the 3-D domain.	75
Figure 3.16	95% percentile of simulated percolation fluxes at Repository level for the 3-D domain.	76
Figure 3.17	Mean of simulated percolation fluxes at water table for the 3-D domain.	76
Figure 3.18	Variance of simulated percolation fluxes at water table for the 3-D domain.....	77
Figure 3.19	5% percentile of simulated percolation fluxes at water table for the 3-D domain.	77
Figure 3.20	95% percentile of simulated percolation fluxes at water table for the 3-D domain.	78
Figure 4.1	Sample mean and variance of simulated cumulative fractional mass of a conservative tracer (Tc) arriving at water table after 0.1, 1.0, 10 and 100 years with 95% confidence interval for the three-dimensional domain.	83
Figure 4.2	Sample mean and variance of simulated cumulative fractional mass of a reactive tracer (Np) arriving at water table after 0.1, 1.0, 10 and 100 years with 95% confidence interval for the three-dimensional domain.....	85
Figure 4.3	Sample mean and variance of simulated travel time of a conservative tracer (Tc) arriving at water table at 50%, 75% and 95% breakthrough with 95% confidence interval for the three-dimensional domain.	88
Figure 4.4	Sample mean and variance of simulated travel time of a reactive tracer (Np) arriving at water table at 25%, 50% and 75% breakthrough with 95% confidence interval for the three-dimensional domain.	89
Figure 4.5	Simulated breakthrough curves of cumulative mass of a conservative tracer (Tc) arriving at water table for the three-dimensional domain.....	91
Figure 4.6	Simulated breakthrough curves of cumulative mass of a reactive tracer (Np) arriving at water table for the three-dimensional domain.....	93

Figure 4.7	Mean of simulated cumulative, normalized mass arrival contours of a conservative tracer (Tc) at water table after 1,000 years for the 3-D domain.	94
Figure 4.8	Variance of simulated cumulative, normalized mass arrival contours of a conservative tracer (Tc) at water table after 1,000 years for the 3-D domain.	95
Figure 4.9	5% percentile of simulated cumulative, normalized mass arrival contours of a conservative tracer (Tc) at water table after 1,000 years for the 3-D domain.	95
Figure 4.10	95% percentile of simulated cumulative, normalized mass arrival contours of a conservative tracer (Tc) at water table after 1,000 years for the 3-D domain.	96
Figure 4.11	Mean of simulated cumulative, normalized mass arrival contours of a conservative tracer (Tc) at water table after 1,000,000 years for the 3-D domain.	98
Figure 4.12	Variance of simulated cumulative, normalized mass arrival contours of the conservative tracer at water table after 1,000,000 years for the 3-D domain.	99
Figure 4.13	5% percentile of simulated cumulative, normalized mass arrival contours of a conservative tracer (Tc) at water table after 1,000,000 years for 3-D domain.	99
Figure 4.14	95% percentile of simulated cumulative, normalized mass arrival contours of a conservative tracer at water table after 1,000,000 years for 3-D domain.	100
Figure 4.15	Mean of simulated cumulative, normalized mass arrival contours of a reactive tracer (Np) at water table after 1,000 years for the 3-D domain.	101
Figure 4.16	Variance of simulated cumulative, normalized mass arrival contours of a reactive tracer (Np) at water table after 1,000 years for the 3-D domain.	101
Figure 4.17	5% percentile of simulated cumulative, normalized mass arrival contours of a reactive tracer (Np) at water table after 1,000 years for the 3-D domain.	102
Figure 4.18	95% percentile of simulated cumulative, normalized mass arrival contours of a reactive tracer (Np) at water table after 1,000 years for the 3-D domain.	102
Figure 4.19	Mean of simulated cumulative, normalized mass arrival contours of a reactive tracer (Np) at water table after 1,000,000 years for the 3-D domain.	103
Figure 4.20	Variance of simulated cumulative, normalized mass arrival contours of a reactive tracer (Np) at water table after 1,000,000 years for the 3-D domain.	104
Figure 4.21	5% percentile of simulated cumulative, normalized mass arrival contours of a reactive tracer (Np) at water table after 1,000,000 years for the 3-D domain.	104
Figure 4.22	95% percentile of simulated cumulative, normalized mass arrival contours of a reactive tracer (Np) at water table after 1,000,000 years for the 3-D domain.	105
Figure A.1	Space discretization and geometry variables in the integral finite-difference method (Pruess, et al., 1999; Wu et al., 2000).	118
Figure A.2	Schematic illustration of spatial weighting scheme for velocity fields (Pruess et al., 1999; Wu et al., 2000).	120

ACKNOWLEDGMENTS

This research project was supported by the U.S. Department of Energy through Desert Research Institute, under Grant Number DOE/UNLV-YM GEOSTAT&STOCHASTIC 6450-644-4450 and NSF EPSCoR ACES scholarship.

First of all, I would like to thank my advisors, Dr. Zhongbo Yu and Dr. Ming Ye, for their support, patience, encouragement, and invaluable guidance throughout my graduate studies. I am also grateful to their generous financial supports. Many thanks also go to my committee members, Dr. Lambis Papelis, Dr. Zhonghai Ding, Dr. Bill Hu, and Dr. Jichun Li.

I am grateful to Dr. Yushu Wu for his kind help. He provided the invaluable experiences in flow and transport simulation using TOUGH2 code. I would like to thank Dr. Keni Zhang and Craig Shirely, they gave me many help in vertical flux extraction and data collection.

Many thanks to my colleagues in University of Nevada Las Vegas and Desert Research Institute, who helped and supported me in many ways over the years. Special thanks to Dr. Weiquan Dong, who helped me overcome various difficulties including research and living problems.

Finally, thanks to my parents. They have provided long-distance love and support throughout.

CHAPTER 1

INTRODUCTION

1.1 Introduction and Literature Review

Yucca Mountain has been considered as a potential nuclear waste repository site because of various climatic, hydrologic, and hydrogeologic reasons such as low precipitation, high evaporation, and low-permeability rocks. It is indispensable to evaluate the possible effects of a nuclear waste repository on the groundwater system and environment in this area. Since the unsaturated zone acts as a critical natural barrier to delay the arrival of radionuclide at the saturated zone, it is also very necessary to understand flow and radionuclide transport in the unsaturated zone. The unsaturated zone at Yucca Mountain is a complex system consisting of various hydrologic units such as variably fractured and welded and nonwelded tuffs and their hydrogeologic properties are heterogeneous and of multi-scale (Zhou et al., 2003). The parameter uncertainty and heterogeneity in hydraulic properties has a significant influence on the unsaturated flow and radionuclide transport (Nichols and Freshley, 1993; Bodvarsson et al., 2001; Zhou et al., 2003). Due to parameter uncertainty and heterogeneity in hydraulic properties, hydraulic characterization is uncertain and the associated flow and radionuclide transport predictions are subject to uncertainty. Therefore, it is very important for the Yucca Mountain Project to assess the uncertainty of flow and radionuclide transport at the

unsaturated zone of Yucca Mountain and understanding the effects of parameter uncertainty on the simulation of flow and transport will improve the site characterization and decision making.

The uncertainty arises from various sources: (1) natural or irreducible uncertainty; (2) model uncertainty; and (3) parametric and data uncertainty. Uncertainty assessment has been an important issue in simulation of flow and radionuclide transport and several different assessment techniques have been developed such as fuzzy set theory, linear first-order, second-moment (FOSM) and Monte Carlo method (Dou et al., 1995; James and Oldenburg, 1997; Nichols and Freshley, 1993; Balakrishnan, 2005). Dou et al. (1995) developed a method based on the fuzzy set theory to capture the uncertainty in imprecise parameters and to implement them into a two-dimensional groundwater flow model. The imprecise aquifer parameters were characterized by fuzzy membership functions. The associated uncertainty of hydraulic heads caused by the imprecise parameters could be evaluated by fuzzy numbers solved by a developed fuzzy groundwater model. James and Oldenburg (1997) evaluated the uncertainty of trichloroethylene (TCE) concentrations by both linear FOSM and Monte Carlo analysis in subsurface contaminant transport simulations due to parameter uncertainty and conceptual model variation. Because the model predictions was required as a linear function of model parameters in linear FOSM analysis, the uncertainties in simulated results by linear FOSM analysis had more spurious oscillations in early time than ones by Monte Carlo method. The results also showed the uncertainty was more sensitive to conceptual model variation.

Monte Carlo method is conceptually straightforward. The basic steps of Monte Carlo simulations are: (1) to determine the input data by generating the random field of

required parameters with a large number of realizations; (2) to transform the input data to output data by solving the physical equations or running the models to obtain the output data for each realization; (3) to calculate the statistic variables such as mean, variance, and covariance to predict the results of output variables and to evaluate the uncertainty of the prediction.

Monte Carlo method has broad range of applications in linear and nonlinear flow and transport problems and thus has been used extensively for the uncertainty analysis in various fields (Balakrishnan, et al., 2005; James and Oldenburg, 1997; Kupfersberger and Deutsch, 1999; Lu and Zhang, 2003; Nichols and Freshley, 1993). For example, Naff et al. (1998a, b) examined the effects of hydraulic conductivity in heterogeneous media, as well as initial and boundary conditions, on the flow and conservative transport using Monte Carlo method. In contaminant transport simulations, the uncertainty in concentration predictions is always caused by the uncertainty in model parameters including permeability, porosity, diffusivity, chemical solubility and sorption coefficient. The predictive uncertainty can be evaluated using the Monte Carlo method (James and Oldenburg, 1997).

A major disadvantage of Monte Carlo method is that it is computationally expensive, since it requires a large number of model simulations to obtain sample statistics approximating their ensemble counterparts. Several methods based on Monte Carlo approach have been proposed to improve the computational efforts by reducing the number of model simulations at convergence. Kupfersberger and Deutsch (1999) proposed an approach to analyze the uncertainty with less computational effort. Because of limited computer resources, it was impossible to simulate the fine scale flow and

transport over all realizations. The method is to rank the coarse scale flow and transport simulation results with all realizations and to select a limited number of realizations from a number classes of divided ranges of coarse scale results randomly for fine scale flow and transport simulation. The improved approach was applied in the uncertainty assessment for aquifer response in Columbus aquifers, Mississippi. The results indicated the computational time measured by the workstation with a RISC R 5000 processor was reduced by running fine scale realizations selected according to their coarse scale aquifer response. Lu and Zhang (2003) introduced a new approach called importance sampling to improve the computational efficiency of conventional Monte Carlo simulation. The objectives of the method were to sample the values with more important impact on the results more frequently by importance density functions and to obtain the accurate estimate of results with fewer samples than ones in Monte Carlo method. The new approach was applied in two illustrative synthetic examples to evaluate the uncertainty of hydraulic head and particle's travel time for one-dimensional flow and transport. Their results indicated that the simulations with the importance sampling technique could be several orders of magnitude more efficient than the conventional Monte Carlo simulations in the two cases. Balakrishnan et al. (2005) compared the uncertainty assessment techniques among Stochastic Response Surface Method (SRS), High Dimensional Model Representation (HDMR) and Monte Carlo method by applying them into groundwater flow simulations in Savannah River Site General Separations Areas (GSA) using the subsurface Flow and Contaminant Transport (FACT) code. The objective of SRS was to reduce the number of model simulations for the adequate estimation of uncertainty by evaluating an SRS expansion of standard random variables

and outputs. The uncertainty analysis using HDMR was evaluated with an accurate reduced model with small realizations because HDMR could map out the relationships between sets of input and output model variables. The results showed that the methods of SRSM and HDMR for the uncertainty analysis required less computational time and more accurate output uncertainty assessment than the traditional Monte Carlo simulation.

Another disadvantage of the Monte Carlo method is that it is lack of criteria to determine if Monte Carlo simulations converge. Because the statistical distributions of output data are required truly representative of the parameter uncertainty in Monte Carlo simulation (Cowles and Carlin, 1996), it is difficult to decide how many realizations it could be at convergence. The moments of output data may be overestimated or underestimated because of the insufficient number of realizations. To solve the convergence problem, some diagnostic tools and criteria have been applied for the convergence of Markov Chain Monte Carlo simulation and Monte Carlo Simulation (Cowles and Carlin, 1996; Belli, et al., 1994; Hassan et al., 1998; Robert and Casella, 1999; Shapiro and Homem-de-mello, 2000; Ballio and Guadagnini, 2004). Cowles and Carlin (1996) applied 13 diagnostic tools to address the convergence problem for Markov Chain Monte Carlo method. After comparing their performance in two examples, it can be concluded that all diagnostic methods can fail to detect the sort of convergence they were designed to identify. Therefore, a combination of diagnostic tools was recommended. Bellin et al. (1994) proposed a convergence criterion based on the mean squared error averaged over the entire domain to check the convergence in transport modeling. When the mean squared error vanishes, it can be said that the results have reached the convergence. Hassan et al. (1998) employed the convergence criterion

proposed by Bellin et al. (1994) to check the convergence of Monte Carlo simulation for yielding accurate results in flow and transport simulations. Ballio and Guadagnini (2004) proposed a new methodology based on simple rules of statistical inference for convergence analysis of Monte Carlo simulation. The new method was implemented to examine the convergence in a typical steady state groundwater flow problem and can be extended to other statistical quantities in different fields.

The sources of uncertainties in the unsaturated zone at Yucca Mountain could be from various types such as parametric uncertainty, data uncertainty, scenario uncertainty in climate change, conceptual model uncertainty in hydrogeological models. Many uncertainty assessments have been evaluated for the Yucca Mountain project (Nichols and Freshley, 1993; Zhou et al., 2003; Wu et al., 2002; Wu et al., 2004a, 2004b). Nichols and Freshley (1993) applied Monte Carlo simulations to evaluate the uncertainty of hydraulic parameters on groundwater travel time and the results indicated that the uncertainty in recharge and matrix porosity accounted for nearly all of the variation in travel-time calculations. Wu et al. (2002, 2004a, b) evaluated the uncertainties of flow and transport caused by the infiltration, climate change, and different conceptual models in the unsaturated zone at Yucca Mountain. In Wu's study, mean, lower, and upper bounds infiltration rates were combined with present-day and two future climates to investigate the uncertainties of flow and transport. Zhou et al. (2003) investigated the effects of unsaturated flow parameter heterogeneity at different scales in the unsaturated fractured rock at Yucca Mountain on unsaturated flow and non-adsorbing tracer transport. Two-dimensional random fields of three hydraulic parameters were generated based on a simplified form of a random field representing multiscale heterogeneity, layer-

scale mean properties calibrated by inverse modeling and local-scale perturbations. The results indicated that the local-scale heterogeneity of matrix and fracture resulted in fast flow paths in fractures and high flux variation in matrix and had a considerable effect on tracer transport in the early time of tracer mass arriving at the water table.

Nevertheless, comprehensive and rigorous assessment of parametric uncertainty for three-dimensional unsaturated flow and radionuclide transport has not been conducted. Measurements of hydraulic properties in matrix and fractures at the unsaturated zone of Yucca mountain (Flint, 1998; Flint, 2003; Liu et al., 2003) provided the basis for our thorough analysis. Previous studies (Nichols and Freshley, 1993; Liu et al., 2003) assumed that flow and transport parameters follow normal or log-normal distributions, which however have not been tested rigorously based on the site measurements. In addition, the distributions of hydraulic properties had not been determined with scientific techniques for all layers in the unsaturated zone at Yucca Mountain. Moreover, correlations between hydraulic parameters had been ignored in the previous studies despite that the correlations reflected in site measurements may affect flow and transport simulations.

Scientific techniques exist to resolve the above problems and will be used in our study. The main objective of this study is to evaluate the uncertainties of unsaturated flow and radionuclide transport caused by parameter uncertainty in matrix hydraulic properties using Monte Carlo method and a three-dimensional model (TOUGH2) in the unsaturated zone at Yucca Mountain. In this study, Latin Hypercube Sampling (LHS) method is used to generate random fields of hydraulic parameters such as hydraulic conductivity and porosity. For each realization, the generated random fields are used as the input data to

TOUGH2 code and to simulate groundwater flow and radionuclide transport. Then the means and variances of flow and transport over all realizations can be estimated. Therefore, the prediction of unsaturated flow and radionuclide transport can be obtained and the uncertainty of the model can also be quantified. To solve the problem of assumed distributions of hydraulic parameters, Lilliefors Test for normality is applied in this study to determine the distributions of matrix porosity and matrix permeability by selecting the best fitted distributions from four Johnson transformations and three classic re-expressions based on the field data (Carsel and Parrish, 1988; Mallants et al., 1996). The spearman rank correlation is employed to calculate the correlations between hydraulic parameters from the measured data for each layer. The reasons that the rank correlation is used in this study are that the correlation coefficients based on original data may lose meaning and interpretation with non-normal data and the rank correlation can be quite meaningful in most cases (Iman and Conover, 1982). A newly developed convergence criterion by Ballio and Guadagnini (2004) is implemented to examine the convergence of Monte Carlo method.

TOUGH2, developed at Lawrence Berkeley National laboratory, is a numerical model for multi-dimension fluid and heat flows of multi-phase, multi-component fluid mixtures in porous and fractured media (Pruess et al., 1999). Wu and Pruess (2000) introduced a newly developed numerical method (TOUGH2) to simulate radionuclide transport through heterogeneous fractured rocks in a non-isothermal multiphase system. In TOUGH2, a dual-continua approach such as double- or multiple-porosity, or dual-permeability is supplemented into the model to handle the fracture-matrix interactions. Two examples of transport simulations were presented to demonstrate the application of

the TOUGH2 for modeling radionuclide transport in heterogeneous fractured porous media under multiphase and non-isothermal conditions. The model can have a wide range of applications in radionuclide transport simulations in the unsaturated zone at Yucca Mountain because of its advantages of the formulation and implemented code. Wu et al. (2002, 2004a, b) employed TOUGH2 to simulate unsaturated flow and radionuclide transport in the unsaturated zone at Yucca Mountain.

Yucca Mountain is a proposed nuclear waste repository and it is very important to understand how the nuclear waste affects the environment and groundwater systems around this area. In this study, generated random fields represent the parameter uncertainty of matrix porosity, permeability and sorption coefficient at Yucca Mountain. Monte Carlo method and TOUGH2 are used together to evaluate the effects of the parameter uncertainty in hydraulic properties on the simulation of flow and transport. The heterogeneous parameter fields are conceptualized as statistically homogeneous random fields with constant mean and variance for each model layer discussed below. The simulation results indicate the parameter uncertainty in matrix porosity, permeability and sorption coefficient has a significant influence on simulated unsaturated flow and radionuclide transport. Therefore, the research results will be helpful to understand how radionuclides transport in the subsurface and react in the unsaturated zone and also provide useful information for better evaluation of how the nuclear waste repository affects the groundwater and environmental systems around the area.

1.2 Objective and Scope

The objectives of this study are as follows:

- (1) Generate the random fields of hydraulic parameters based on the field data for each model layer;
- (2) Simulate the unsaturated flow and radionuclide transport in the unsaturated zone at Yucca Mountain using TOUGH2 code and Monte Carlo approach;
- (3) Evaluate the uncertainties of flow and transport caused by parameter uncertainty in hydraulic properties within each geologic unit in the unsaturated zone at Yucca Mountain.

This thesis is organized into five chapters and one appendix. Chapter 1 includes introduction, literature review and study site description. In chapter 2, the distributions of hydraulic parameters for each layer are determined and the random fields are generated. Chapter 3 analyzes the uncertainties of unsaturated flow caused by parameter uncertainty of matrix porosity and permeability. Chapter 4 simulates the two kinds of radionuclide transport (conservative and reactive tracers) and evaluates their uncertainties from the parameter uncertainty of matrix porosity, permeability and sorption coefficient (K_d). Chapter 5 offers the conclusions of this study. In appendix A, the basic principles of Monte Carlo method, TOUGH2 Code and the convergence criteria by Ballio and Guadagnini are described in detail.

1.3 Study Site

The unsaturated zone at Yucca Mountain has been selected as a high-level nuclear waste repository. It is necessary to understand the geologic, hydrologic and climatic

characteristics around Yucca Mountain. Since the middle of 1980s, the various geological settings, hydrological properties and geothermal conditions in the unsaturated and saturated zones have been investigated and a large number of models have been used to describe the geologic properties and hydrologic parameters at Yucca Mountain and to understand how the repository affects the groundwater flow system and environmental system around this area (Flint, 1998; Wu and Pruess, 2000; Fenelon and Moreo, 2002; Wu et al., 2002; Wu et al., 2004a).

The study site of the unsaturated zone encompassing an area of approximate 20 km² at Yucca Mountain is shown in Figure 1.1 with the domain, grids, repository blocks and borehole locations (Wu et al., 2004a). A refined mesh in the vicinity of the repository is used in this three-dimensional model grid. It consists of 980 mesh columns of both fracture and matrix continua, 45 computational grid layers vertically, 86,440 gridblocks, and 343,520 connections in a dual-permeability grid (Wu et al., 2004a).

The unsaturated zone is between 500 and 700 m thick. The proposed repository area is located in the center of the domain and a typical east-west cross section of subsurface geology is shown in Figure 1.2. There are several geologic units and layers in Figure 1.2, such as Tiva Canyon welded unit (TCw), Paintbrush nonwelded unit (PTn), Topopah Spring welded unit (TSw), Calico Hills nonwelded (CHn) unit and Crater Flat undifferentiated (CFu) unit in this study area. The repository area will be in the Topopah Spring welded unit (TSw) of densely welded tuffs with a low porosity and below the Paintbrush nonwelded unit (PTn) with a high porosity, low fractures and high storage capacity. Therefore, the distributions of porosity, permeability and sorption coefficients are totally different for each unit or layer. The highly heterogeneous nature of hydraulic

properties in these geologic units will have significant effects on unsaturated liquid flow and radionuclide transport in this study area.

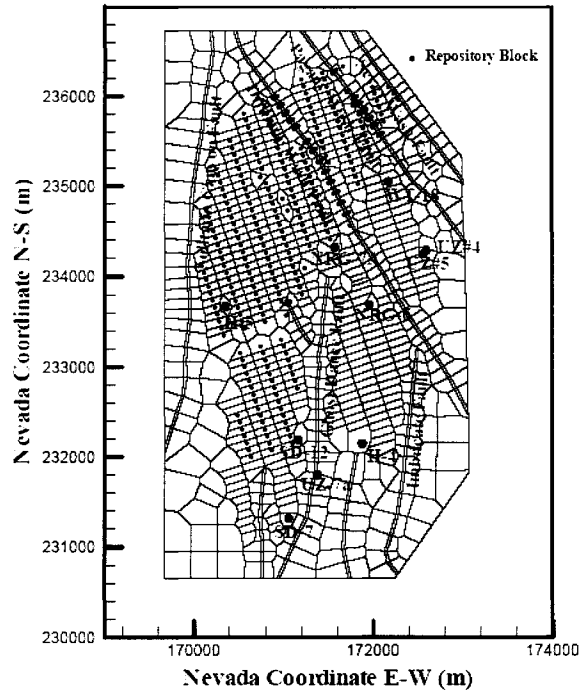


Figure 1.1 Study area of the unsaturated zone at Yucca Mountain (Wu et al., 2004a).

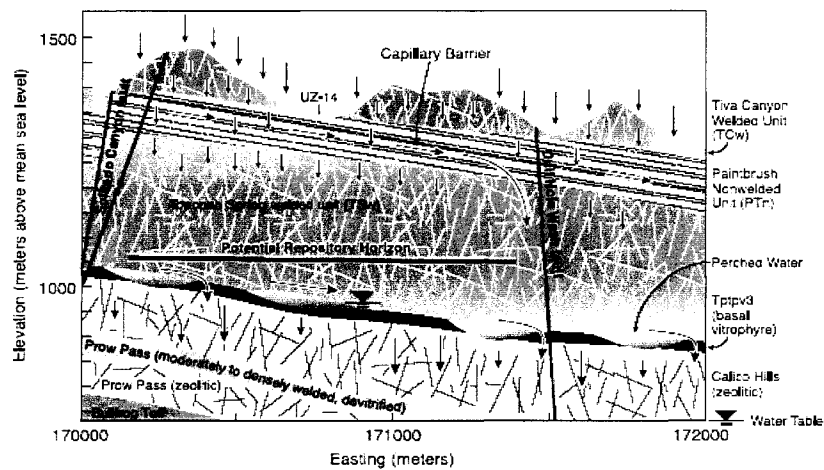


Figure 1.2 A typical cross section of geological profile at Yucca Mountain (Wu et al., 2004a).

Table 1.1 lists the geological units/layers for different hydrogeologic units and the associated unsaturated zone model (TOUGH2) numerical grid-layer information.

Table 1.1 Lithostratigraphy used in geological framework model, unsaturated zone model layer, and hydrogeological unit correlation used in this thesis (Wu et al., 2004a).

Major Unit	Lithostratigraphic nomenclature	Unsaturated Zone Model		Hydrogeological Unit (Flint, 1998)
		Unit/Layer	Number	
Tiva Canyon welded (TCW)	Tpcr	Tcw11	1	CCR, CUC
	Tpcp	Tcw12	2	CUL, CW
	TpcLD			
	Tpcpv3	Tcw13	3	CMW
	Tpcpv2			
Paintbrush nonwelded (PTn)	Tpcpv1	Ptn21	4	CNW
	Tpbt4	Ptn22	5	BT4
	Tpy (Yucca)	Ptn23	6	TPY
		Ptn24	7	BT3
	Tpbt3			
	Tpp (Pah)	Ptn25	8	TPP
	TPbt2	Ptn26	9	BT2
	Tptrv3			
	Tptrv2			
Topopah Spring welded (TSW)	Tptrv1	Tsw31	10	TC
	Tptm	Tsw32	11	TR
		Tsw33	12	TUL
	Tptrl, Tptf			
	Tptpul, RHHTop			
	Tptpmn	Tsw34	13	TMN
	Tptpll	Tsw35	14	TLL
	Tptpln	Tsw36	15	TM2 (upper 2/3 of Tptpln)
		Tsw37	16	TM1 (lower 1/3 of Tptpln)

Table 1.1 (Cont.) Lithostratigraphy used in geological framework model, unsaturated zone model layer, and hydrogeological unit correlation used in this thesis (Wu et al., 2004a).

Major Unit	Lithostratigraphic nomenclature	Unsaturated Zone Model		Hydrogeological Unit (Flint, 1998)
		Unit/Layer	Number	
Topopah Spring welded (TSW)	Tptpv3	Tsw38	17	PV3
	Tptpv2	Tsw39 (vit, zeo)	18(zeo), 19 (vit)	PV2
Calico Hills nonwelded (CHn)	Tptpv1	Ch1 (vit, zeo)	20(zeo), 21(vit)	BT1 or BT1a (altered)
	Tpbt1			
	Tac (Calico)	Ch2 (vit, zeo)	22(vit), 26(zeo)	CHV (vitric) or CHZ (zeolitic)
		Ch3 (vit, zeo)	23 (vit), 27(zeo)	
		Ch4 (vit, zeo)	24(vit), 28(zeo)	
		Ch5 (vit, zeo)	25(vit), 29(zeo)	
	Tacbt (Calicobt)	Ch6 (vit, zeo)	30(zeo), 31(vit)	BT
	Tcpuv (Prowuv)	pp4	32	PP4 (zeolitic)
	Tcpuc (Prowuc)	pp3	33	PP3 (devitrified)
	Tcpmd (Prowmd)	pp2	34	PP2 (devitrified)
	Tcplc (Prowlc)			
	Tcplv (Prowlv)	pp1	35	PP1 (zeolitic)
	Tcpbt (Prowbt)			
	Tcbuv (Bullfroguv)			
Crater Flat undifferentiated (CFu)	Tcbuc (Bullfroguc)	bf3	36	BF3 (welded)
	Tcbmd (Bullfrogmd)			
	Tcblc (Bullfroglc)			
	Tcblv (Bullfroglv)	bf2	37	BF2 (nonwelded)
	Tcbbt (Bullfrogbt)			
	Tctuv (Tramuv)			
	Tctuc (Tramuc)	tr3	38	Not Available
	Tctmd (Trammd)			
	Tctlc (Tramlc)			
	Tctlv (Tramlv)	tr2	39	Not Available
	Tctbt (Trambt) and below			

CHAPTER 2

RANDOM FIELD GENERATION OF HYDRAULIC PARAMETERS

2.1 Introduction

Heterogeneity of hydraulic parameters (e.g., porosity, saturated hydraulic conductivity, water retention parameters, and sorption coefficient) affects groundwater flow and solute transport. Parametric uncertainty inevitably arises due to the lack of parameter measurements of the heterogeneous parameter fields. In this study, the Monte Carlo method is employed to evaluate the propagation of parametric uncertainty in flow and solute transport in the unsaturated zone at Yucca Mountain. The general procedure of Monte Carlo simulation is as follows:

- (1) Generate numerous equally likely random fields for model parameter according to the parameter probabilistic distributions;
- (2) Conduct numerical simulation to estimate the quantities of interest for each parameter random field;
- (3) Calculate the statistics (e.g., mean and variance) of the quantities of interest to yield the optimum prediction and associated predictive uncertainty.

As the basis of the Monte Carlo simulation, generating the random fields of hydraulic parameters plays a critical role and it entails the determination of parameter probability distributions.

Some methods have been used to generate random fields and to determine the

parameter probability distribution based on measurements. For example, to generate the random fields in the unsaturated zone at Yucca Mountain, Zhou et al. (2003) assumed the distributions of matrix permeability, matrix van Genuchten α and fracture permeability follow lognormal distributions and the parameters were mutually independent. However, the justification for the lognormal distribution was weak and the correlation between the hydraulic parameters may not be ignored. Carsel and Parrish (1988) employed four transformations of Johnson system to soil hydraulic parameters and used the Kolmogorov-Smirnov (K-S) test to determine which transform yields the best normality fitting. Random fields of the parameters with correlations were generated based on selected transformations, fitted distributions and Pearson correlations for the transformed variables (Carsel and Parrish, 1988). Mallants et al. (1996) applied seven transformations including four Johnson transformations and three classical re-expressions to transform the measured data of van Genuchten α , n and other parameters and the normality of the transformed data was judged by Shapiro-Wilk test.

In this study, we first apply four Johnson transformations and three classic re-expressions (Carsel and Parrish, 1988; Mallants et al., 1996) to the measurements of matrix porosity, matrix saturated hydraulic conductivity and sorption coefficient and then apply the Lilliefors Test to select the transform that yields the best normality fit. The Spearman rank correlations are calculated for the transformed measurements in each model layer. Subsequently, the random fields of the hydraulic parameters are generated by Latin Hypercube Sampling method (LHS) based on the fitted distributions and Spearman rank correlations for each layer. The input data of numerical simulations for each realization are created based on these random fields. Other hydraulic parameters

(e.g., van Genuchten α and n) are treated as deterministic variables, as their distributions cannot be determined from their sparse measurements. By the same token, hydraulic parameters associated with fracture were also treated as deterministic variables.

In this study, the effects of the random matrix porosity, saturated hydraulic conductivity, and sorption coefficient on flow and radionuclide transport in the unsaturated zone at Yucca Mountain are evaluated. The matrix porosity affects the saturation conditions in flow simulations; the matrix saturated hydraulic conductivity affects flux estimates according to Darcy's Law; the matrix sorption affects the retardation time of radionuclide in the unsaturated zone.

2.2 Determination of Hydraulic Parameter Distributions

2.2.1 Data Transformation and Lilliefors Test

In general, one cannot determine the distribution and corresponding distribution characteristics of a random hydraulic parameter without proper transform and rigorous statistical test. In this study, the three distribution types of transformations (lognormal, log ratio and hyperbolic arcsine) from Johnson system (Johnson and Lotz, 1970) and four classical re-expressions ($1/X$, $X^{1/2}$, $X^{1/3}$, X^2) (Mallants et al., 1996) are selected to transform the samples. The lognormal (LN), log ratio (SB), and hyperbolic arcsine (SU) transforms are given as (Johnson and Lotz, 1970; Carsel and Parrish, 1988):

$$\text{LN: } Y = \ln(X) \quad (2.1)$$

$$\text{SB: } Y = \ln(U) = \ln\left(\frac{X - A}{B - X}\right) \quad (2.2)$$

$$\text{SU: } Y = \sinh^{-1}(U) = \ln(U + \sqrt{1 + U^2}) \quad (2.3)$$

where X is the untransformed variable value with limits of variation from A to B ($A < X < B$) and $U = (X-A)/(B-X)$.

Lilliefors Test, a variant of Kolmogorov-Smirnov (K-S) test, is used to test the goodness-of-fit of the transformed data to normal distribution. Lilliefors test is to test whether a certain set of data follow the normal distribution with unspecified parameters estimated from the observations. It differs from K-S test in that it does not require the hypothesized distribution with a completely specified cumulative distribution function (CDF) (Bowen and Bennett, 1988). The steps of Lilliefors test are as follows:

- (1) Standardize the sample values with sample mean and standard deviation estimated from the samples:

$$z_i = \frac{x_i - \bar{x}}{s} \quad (i = 1, 2, \dots, N) \quad (2.4)$$

where z_i and x_i are standardized and original sample values, respectively, \bar{x} and s are the sample mean and standard deviation, respectively, N is the sample size.

Generally, the sample size is at least 4 for Lilliefors test.

- (2) Calculate the empirical CDF $G(z)$ of the standardized z_i and the standard normal CDF $F^*(z)$;
- (3) Estimate the absolute maximum difference between the empirical CDF and the standard normal CDF for each z_i ;

$$T = \max |F^*(z_i) - G(z_i)|, \quad i = 1, 2, \dots, n \quad (2.5)$$

- (4) Select Lilliefors test statistic T^* corresponding to a level of significance α from Lilliefors Test Statistical Table (Bowen and Bennett, 1988) and judge whether the

hypothesis of normality is accepted or not. The test is rejected at α level of significance if T exceeds T^* .

In our study, one of the following eight transforms - Normal distribution (NO), LN, SB, SU, $1/X$, $X^{1/2}$, $X^{1/3}$, and X^2 – is selected for random field generation if it gives the minimum T value of Lilliefors test for each model layer. To get a better fitted distribution, outlying values are not used in estimating the mean and variance in few layers. Nevertheless, they are used in the Lilliefors test calculations to ensure objectivity (Carsel and Parrish, 1988). As discussed below, input parameters of the random field generator LHS are the values of the distribution at 0.01 and 0.99 percentiles. If the best fitted distributions of the parameters make the bound be non-physical meaning values in few layers, the second best fitted distributions of parameters are selected. For example, the best transform for matrix saturated hydraulic conductivity in BT4 layer was $X^{1/3}$ and its mean and variance are 0.0125 and 0.000069. The corresponding 1% and 99% percentiles are -0.00682 and 0.0318 and the negative 1% percentile of the saturated hydraulic conductivity has no physical meaning. Therefore, the best transform can not be selected in this case and the second best one is selected to generate random field.

By applying Johnson transformations, classical re-expressions and Lilliefors Test, the best fits corresponding to mean and variance of the distribution of transformed values are determined for each model layer. The procedures are as follows:

- (1) Determine the limits of variation of matrix porosity based on the minimum and maximum values of measured data for SB and SU transformations;
- (2) Transform the measured data according to seven types of transformations;

- (3) Implement Lillifors Test to select the best transformation and its corresponding probability characteristics for each layer.

2.2.2 Transformation and Distribution of Matrix Porosity

Measurements of matrix porosity for each layer in the unsaturated zone at Yucca Mountain are collected from Yucca Mountain database (DTNs: LB0207REVUZPRP.002, MO0109HYMXPROP.001) and their descriptive statistics (mean, standard variance, minimum, and maximum) is listed in Table 2.1. Spatial heterogeneity in matrix porosity is observed in each layer because of the large range of the measurements. For example, the matrix porosity varies from 0.228 to 0.633 in CNW layer and the range is from 0.137 to 0.578 in BT3 layer. Therefore, it is unreasonable to treat matrix porosity as deterministic values. The histograms of measured matrix porosity for each layer are shown in Figure 2.1, which also plots the histograms of the generated random fields for matrix porosity. Visually, matrix porosity follows a normal distribution in certain layers (e.g., CNW, TR, TUL and PP4) and lognormal distribution in some others (e.g., BT2, PV3, and BF3). However, the visual examination cannot quantify the matrix porosity distribution, which, instead, is determined by applying the transforms and Lilliefors Test discussed above.

The seven Johnson transformations and classic re-expressions (Carsel and Parrish, 1988; Mallants et al., 1996) are applied to the matrix porosity measurements and the transform giving the best normality fit is selected according to the Lilliefors test. The limits of variation for the original measurements, mean and variance of the transformed data, the Lilliefors test T value, and Lilliefors test criteria T^* corresponding to three significance levels ($\alpha = 0.1, 0.05, \text{ and } 0.01$) for matrix porosity in each model layer are

tabulated in Table 2.2. The empirical and fitted CDF of the transformed matrix porosity measurements in each model layer are shown in Figure 2.2. From Table 2.2 and Figure 2.2, the tests are accepted in most layers because the maximum difference (T) between the empirical and theoretical CDFs is less than the critical value (T^*) of Lilliefors Test at a level of significance α . The tests in 17 layers are accepted in the level of significance $\alpha = 0.1$; the ones in 8 layers are accepted in α of 0.05 or 0.01; and the ones in 4 layers are not accepted at any significance levels. In order to accept the test and fit a better distribution, the outlying values in the layers of CCR&CUC, BT2, CHV and BF3 are not used to calculate the mean and variance but are included for goodness of fit. For the layers of PV2a and BT1v, the fitting distributions are not the best ones but the second best one because the best one makes the generated random fields within an unreasonable range without physical meaning. For example, the best fit of the transformations in BT1v layer is X^2 and the corresponding mean and variance are 0.112 and 0.00272, respectively. The 1% and 99% percentiles of the transformation are -0.00931 and 0.233 and are used as the minimum and maximum of random field generation. Because the values of transformation X^2 of matrix porosity can not be negative, the best fit can not be selected in this case and the second one is selected to generate random field. The normality test fails in the four layers CUL&CW, TMN, TM2&TM1 and CHZ, because the values of T are larger than T^* at any level of significance. The large sample size in these layers leads to small values of T^* because the critical value T^* is inverse with square root of sample size. The transform, however, is still accepted in the study, due to the small difference between the empirical and theoretical CDFs (Figure 2.2).

Table 2.1 Descriptive statistics for matrix porosity and saturated hydraulic conductivity.

HGU	Porosity (Φ)					Saturated Hydraulic Conductivity (K_s , m/s)				
	Mean	SD	Min	Maxi	N	Mean	SD	Min	Max	N
CCR&CUC	0.241	0.073	0.038	0.431	124	5.80E-08	6.53E-08	2.03E-08	1.33E-07	3
CUL&CW	0.088	0.032	0.032	0.213	694	7.68E-10	3.02E-09	2.15E-13	1.25E-08	17
CMW	0.200	0.055	0.1	0.452	96	1.89E-08	4.21E-08	3.34E-12	9.41E-08	5
CNW	0.387	0.069	0.228	0.633	104	2.90E-07	3.38E-07	5.12E-12	8.79E-07	10
BT4	0.428	0.100	0.134	0.669	58	4.56E-06	7.59E-06	1.80E-10	2.54E-05	11
TPY	0.233	0.057	0.073	0.309	39	1.38E-08	1.52E-08	3.00E-09	2.45E-08	2
BT3	0.413	0.082	0.137	0.578	73	1.77E-06	2.03E-06	1.90E-09	7.30E-06	11
TPP	0.498	0.041	0.388	0.623	159	1.17E-06	5.76E-07	9.00E-08	1.74E-06	11
BT2	0.490	0.095	0.104	0.614	176	7.10E-06	6.87E-06	1.24E-09	2.06E-05	21
TC	0.054	0.036	0.012	0.273	75	3.21E-08	6.72E-08	1.70E-11	1.68E-07	6
TR	0.157	0.030	0.062	0.267	449	2.03E-07	1.37E-06	1.70E-11	9.37E-06	47
TUL	0.155	0.030	0.076	0.25	438	3.94E-08	2.33E-07	4.20E-13	1.42E-06	37
TMN	0.111	0.020	0.055	0.192	277	4.18E-11	1.72E-10	4.76E-13	1.23E-09	74
TLL	0.131	0.031	0.088	0.263	502	4.11E-09	1.31E-08	1.39E-12	7.65E-08	52
TM2&TM1	0.103	0.025	0.053	0.341	300	4.28E-07	2.00E-06	5.33E-13	9.39E-06	22
PV3	0.043	0.040	0.011	0.34	125	1.66E-10	5.45E-10	8.63E-14	2.25E-09	17
PV2a	0.275	0.096	0.11	0.415	13	B	B	b	B	b
PV2v	0.243	0.122	0.048	0.47	49	3.23E-06	3.69E-06	5.03E-11	1.20E-05	16
BT1a	0.285	0.051	0.158	0.4	46	1.90E-08	3.21E-08	1.83E-13	8.70E-08	10
BT1v	0.324	0.085	0.031	0.5	80	3.76E-06	5.77E-06	1.04E-10	2.20E-05	35
CHV	0.341	0.048	0.04	0.49	130	1.48E-05	1.89E-05	1.68E-12	7.20E-05	47
CHZ	0.322	0.048	0.099	0.433	520	1.19E-09	9.62E-09	3.88E-13	9.54E-08	99
BTa	0.271	0.046	0.181	0.418	73	4.05E-11	6.96E-11	2.08E-13	2.10E-10	9
BTv	a	a	a	a	a	B	B	b	b	b
PP4	0.327	0.050	0.216	0.44	56	4.62E-08	1.08E-07	8.44E-13	3.08E-07	8
PP3	0.318	0.032	0.246	0.395	168	6.91E-08	6.72E-08	4.20E-12	3.65E-07	51
PP2	0.221	0.058	0.099	0.333	127	1.56E-09	3.01E-09	3.75E-12	1.15E-08	35
PP1	0.297	0.043	0.164	0.426	280	9.63E-08	3.88E-07	1.70E-12	1.94E-06	28
BF3	0.142	0.075	0.059	0.369	105	1.31E-08	2.01E-08	6.90E-11	5.58E-08	7
BF2	0.234	0.049	0.16	0.329	40	B	B	b	B	b

NOTE: (a) Only one porosity data point is available for BTv;

(b) Only one saturated conductivity data point is available for Pv2a, BTv and BF2 respectively;

(c) SD is standard deviation of the sample; Min, Max are the minimum and maximum values of the sample; N is the sample size.

Table 2.2 Statistical parameters of matrix porosity for distribution approximation.

HGU	Limits of Variation		Trans-form	Estimated Distribution			Critical Values (T*)		
	A	B		Mean	Variance	T	$\alpha=0.10$	$\alpha=0.05$	$\alpha=0.01$
CCR&CUC ^b	0.037	0.432	X ²	0.063	6.58E-04	0.078	0.072	0.080	0.093
CUL&CW	0.031	0.214	1/X	12.63	14.20	0.072	0.031	0.034	0.039
CMW	0.099	0.453	1/X	5.300	1.49	0.085	0.087	0.090	0.105
CNW	0.227	0.634	NO	0.387	4.74E-03	0.057	0.079	0.087	0.101
BT4	0.133	0.670	SU	0.520	2.63E-02	0.117	0.106	0.116	0.135
TPY	0.072	0.310	X ²	0.058	5.84E-04	0.106	0.129	0.142	0.165
BT3	0.136	0.579	SU	0.585	2.50E-02	0.084	0.094	0.104	0.121
TPP	0.387	0.624	1/X	2.021	2.56E-02	0.060	0.064	0.070	0.082
BT2 ^b	0.103	0.615	SB	1.385	0.79	0.073	0.061	0.067	0.078
TC	0.011	0.274	X ^{1/3}	0.365	4.66E-03	0.059	0.093	0.102	0.119
TR	0.061	0.268	NO	0.157	8.75E-04	0.048	0.038	0.042	0.049
TUL	0.075	0.251	NO	0.155	9.28E-04	0.044	0.038	0.042	0.049
TMN	0.054	0.193	LN	-2.218	3.29E-02	0.070	0.048	0.053	0.062
TLL	0.087	0.264	1/X	8.012	2.55	0.044	0.036	0.040	0.046
TM2&TM1	0.052	0.342	1/X	10.11	3.23	0.082	0.046	0.051	0.060
PV3	0.010	0.341	SB	-2.728	2.04	0.060	0.072	0.079	0.092
PV2a ^c	0.109	0.416	SB	0.181	6.77	0.191	0.214	0.234	0.268
PV2v	0.047	0.471	SB	-0.311	3.79	0.123	0.115	0.127	0.147
BT1a	0.157	0.401	X ^{1/3}	0.656	1.58E-03	0.061	0.119	0.131	0.152
BT1v ^c	0.030	0.501	NO	0.324	7.20E-03	0.088	0.090	0.099	0.115
CHV ^b	0.037	0.491	1/X	2.944	0.079	0.061	0.071	0.078	0.090
CHZ	0.098	0.434	X ²	0.106	8.30E-04	0.068	0.035	0.039	0.045
BTa	0.180	0.419	1/X	3.791	0.40	0.064	0.094	0.104	0.121
BTv ^a									
PP4	0.215	0.441	NO	0.327	2.49E-03	0.049	0.108	0.118	0.138
PP3	0.245	0.396	NO	0.318	9.94E-04	0.054	0.062	0.068	0.080
PP2	0.098	0.334	NO	0.221	3.37E-03	0.066	0.071	0.079	0.091
PP1	0.163	0.427	X ²	0.090	6.21E-04	0.050	0.049	0.053	0.062
BF3 ^b	0.058	0.370	1/X	8.573	9.40	0.078	0.079	0.086	0.101
BF2	0.159	0.330	1/X	4.451	0.81	0.095	0.127	0.140	0.163

Note: (a) The sample size is less than 4 and can not fit the distribution using Lilliefors Test in the layers.
(b) The outlying values were discarding but were included for goodness of fit calculation in the layer.
(c) The distribution is not best fit in order to guarantee the reasonable ranges of random fields.

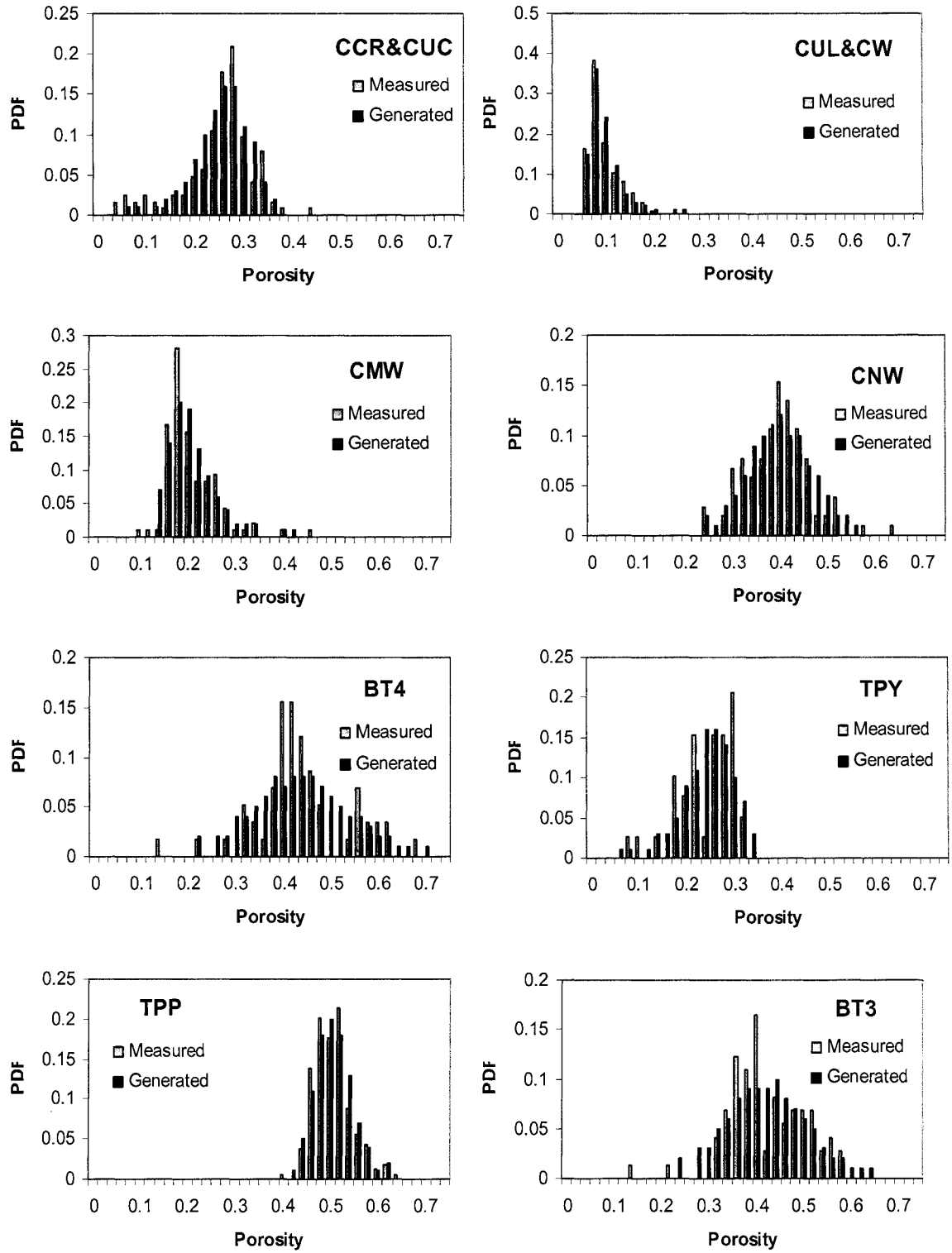


Figure 2.1 Histograms of measured and generated data of matrix porosity for each model layer.

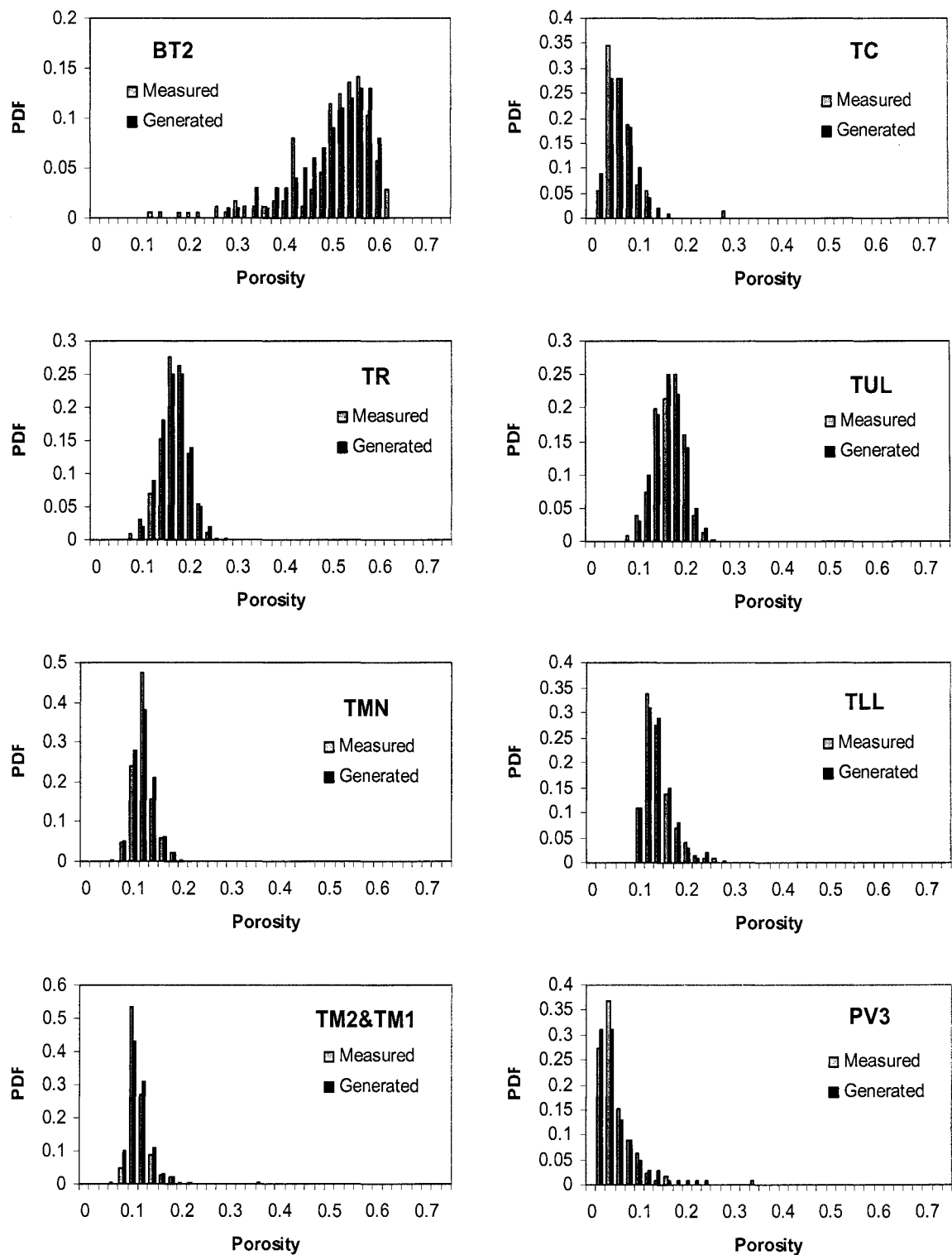


Figure 2.1 (Cont.) Histograms of measured and generated data of matrix porosity for each model layer.

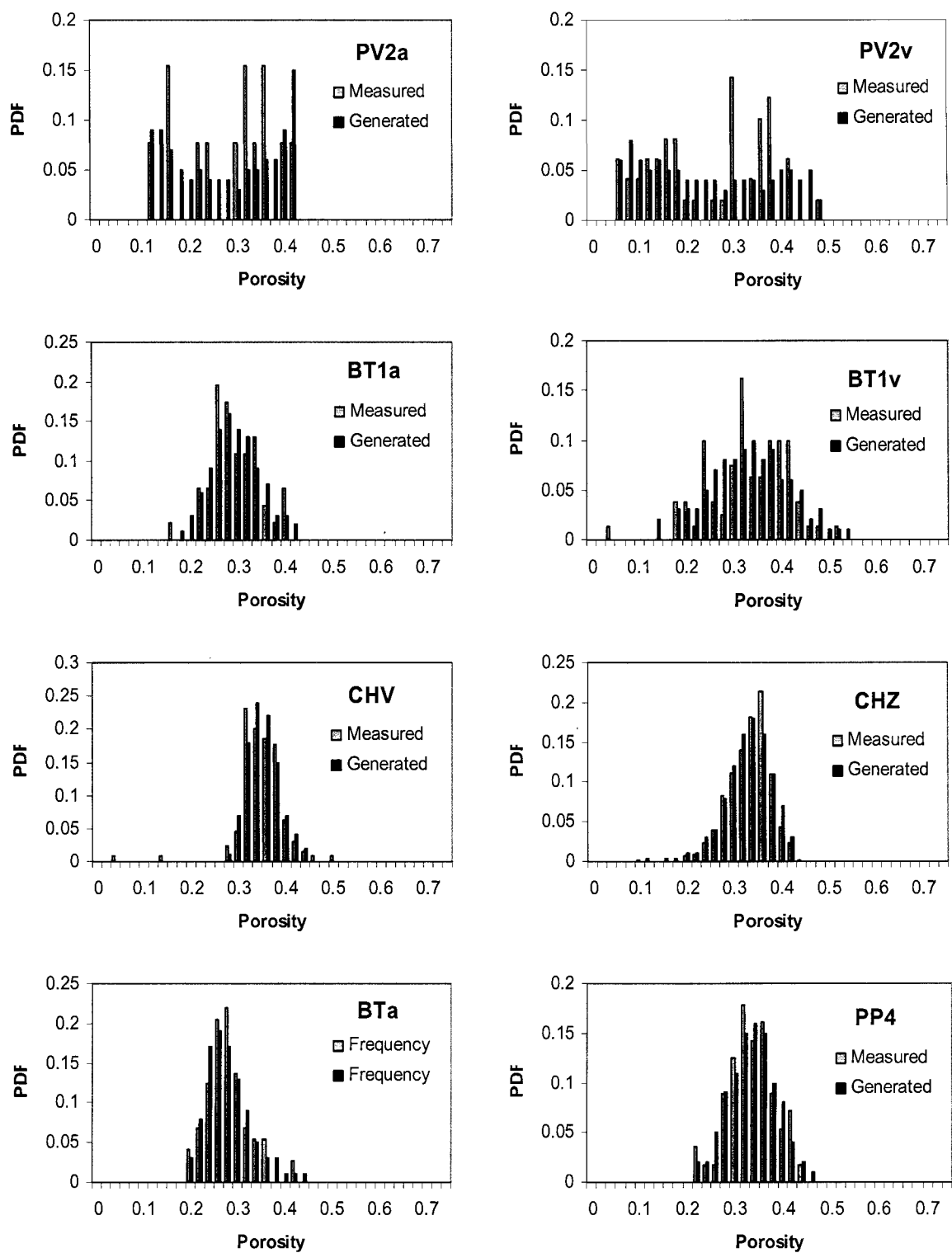


Figure 2.1 (Cont.) Histograms of measured and generated data of matrix porosity for each model layer.

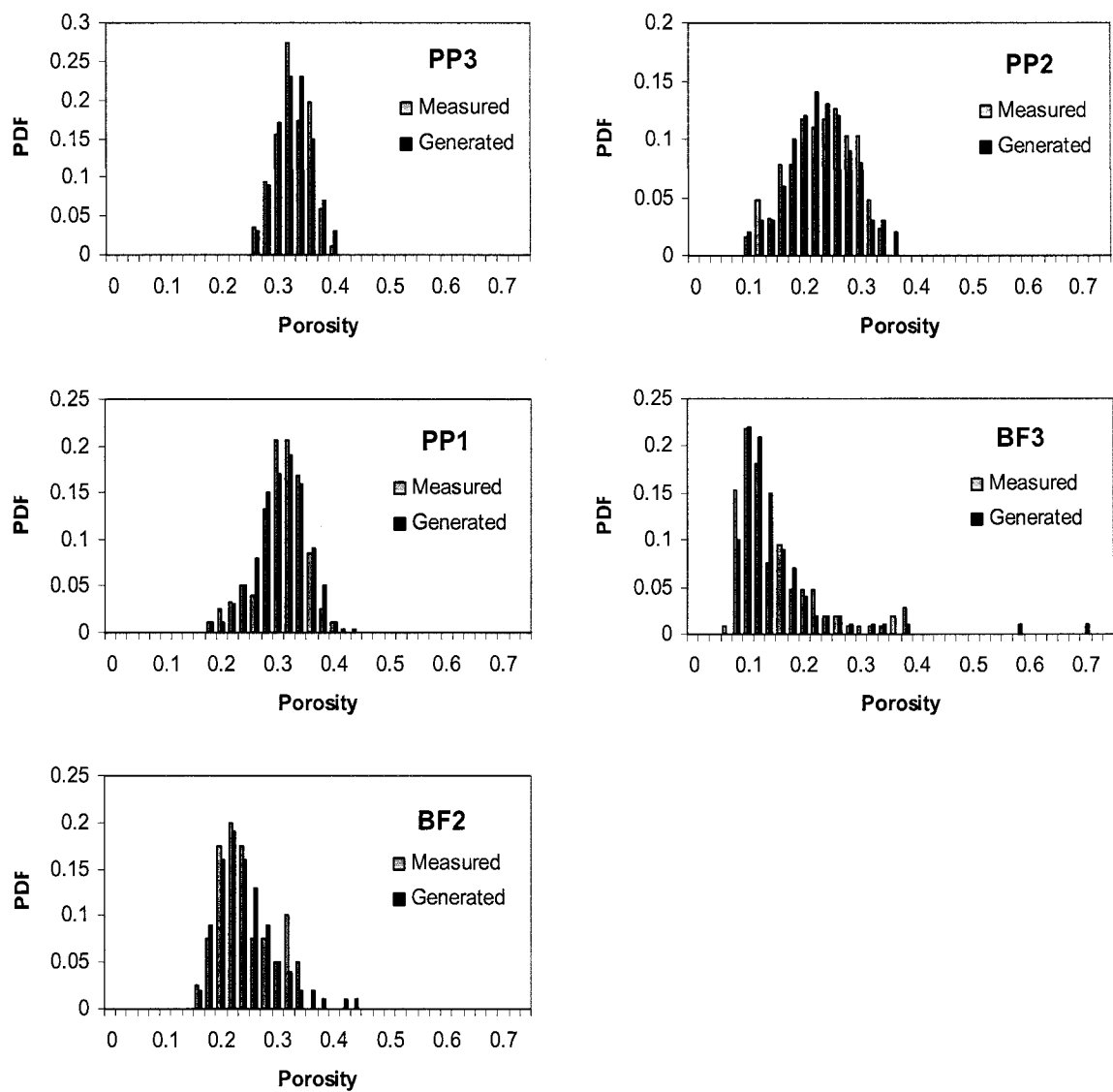


Figure 2.1 (Cont.) Histograms of measured and generated data of matrix porosity for each model layer.

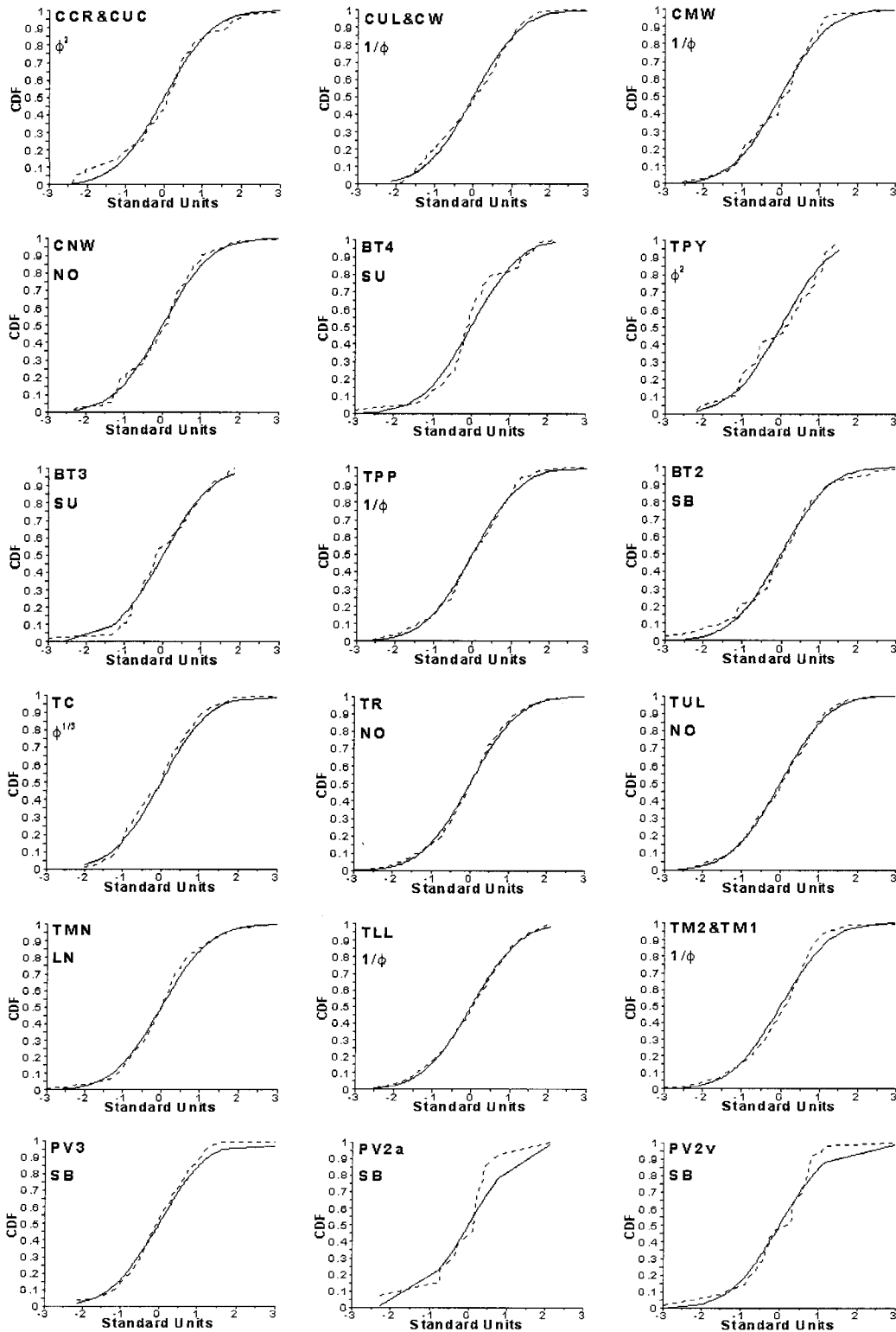


Figure 2.2 Empirical and theoretical distributions for transformed porosity in each model layer.

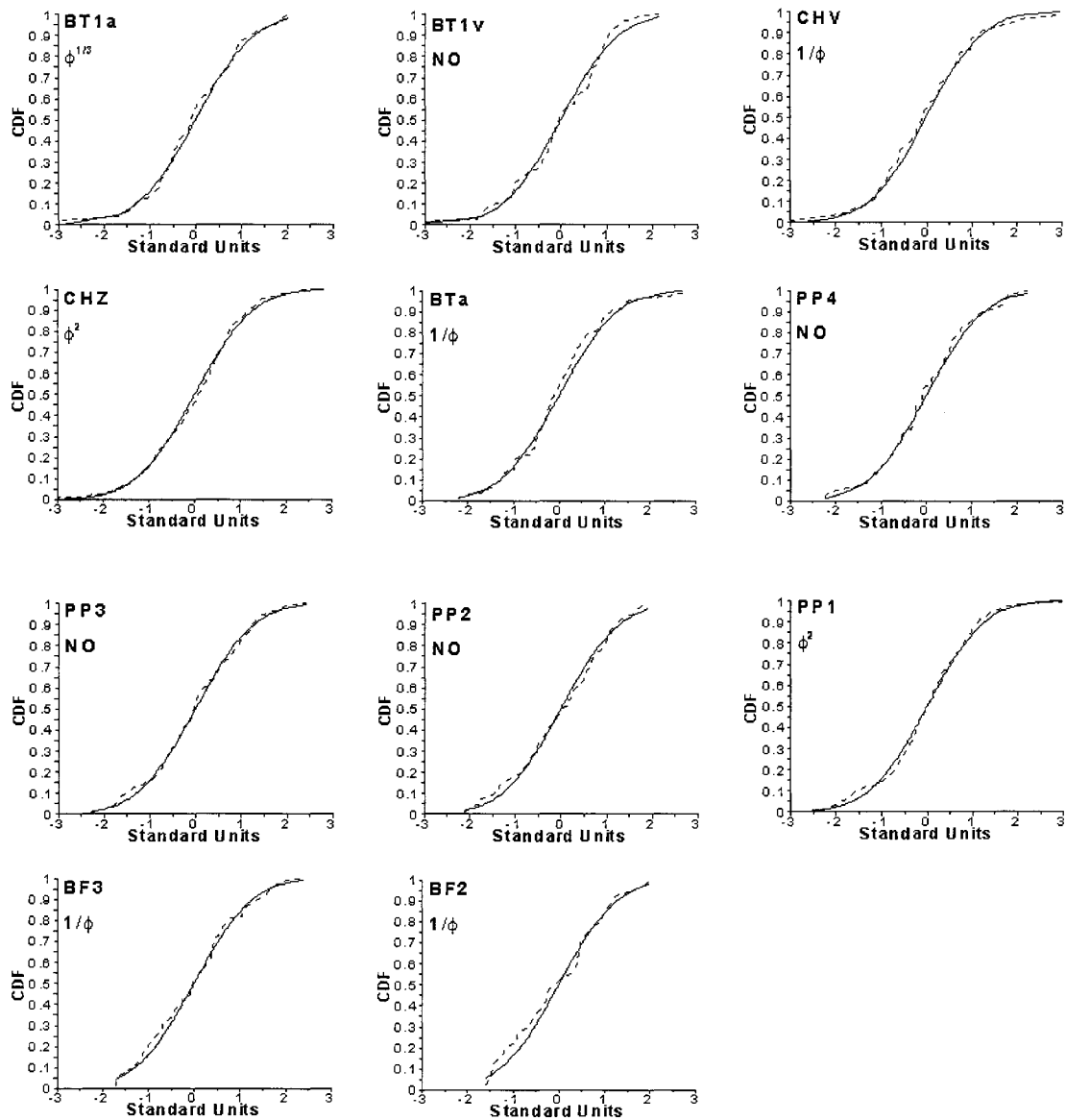


Figure 2.2 (Cont.) Empirical and theoretical distributions for transformed porosity in each model layer.

2.2.3 Transformation and Distribution of Matrix Saturated Hydraulic Conductivity

Measurements of matrix saturated hydraulic conductivity in the unsaturated zone at Yucca Mountain are also collected from Yucca Mountain database (DTNs: LB0207REVUZPRP.002, MO0109HYMXPROP. 001). The descriptive statistics of matrix saturated hydraulic conductivity are calculated in Table 2.1. The number of the measurements of matrix saturated hydraulic conductivity is significantly less than that of matrix porosity. It is not enough to apply Lillifors Test to select the best transformations in some layers such as CCR&CUC, TPY, PV2a, BTv and BF2 layers. From Table 2.1, one can see that there exists spatial heterogeneity in matrix saturated hydraulic conductivity in each layer because of the big difference of measured data. The conductivity has several orders of magnitude difference between the minimum and maximum measured values in all layers. For example it is from 5.12×10^{-12} m/s to 8.79×10^{-7} m/s in CNW layer. Therefore, the deterministic hydraulic conductivity cannot represent the real field and its heterogeneity should be assessed. The histograms of matrix saturated hydraulic conductivity for some layers are shown in Figure 2.3. These figures also plot the histograms of the generated random fields of matrix saturated hydraulic conductivity in corresponding layers. Because of the lacking measured data, the histograms of some layers whose sample sizes are less than 20 such as CUL&CW, CMW, CNW and BT4 etc. are not plotted here. One can see from Figure 2.3 qualitatively that matrix saturated hydraulic conductivity has a lognormal distribution in TR, TUL and TMN layers. For most layers, the distributions cannot be determined from the histograms of the parameter.

The Lillifors Test and transformations are also used to fit the distributions of matrix saturated hydraulic conductivity for most layers. The estimations of the mean and variance for appropriated transformed variables, limits of variation for the original variables, and the values of Lillifors test T for matrix saturated hydraulic conductivity in each model layer are tabulated in Table 2.3. The empirical and fitted CDF of the best fitting distribution for the parameter in some layers are shown in Figure 2.4. The distributions in the layers such as CCR&CUC, TPY, PV2a, BTv and BF2 are not fitted because the sample size of the layers are less than 4 and can not be tested using Lillifors Test. In the layers of CNW, BT4, BT3, BT2 and BF3, the second best fitting distributions are selected to guarantee the generated random fields in a reasonable range because the minimum values of random fields are negative and non physical meaning if the best fit is selected. And the outliers in PV2v, CHV and CHZ layers are also discarded in the mean and variance estimation to get the best fitting distributions. After applying the above methods and assumption, the tests in two-third layers are accepted in the level of significance $\alpha = 0.1$. But the tests in the layers of TMN and CHZ are rejected at any level of significance α because the sample sizes of TMN and CHZ are the largest among all layers. In this case, the transformations with the smallest values of T are selected as the distributions of parameters for those rejected layers. The transformations are still accepted because the small difference between the empirical and theoretical CDF in Figure 2.4. One can also know from Table 2.3, the main types of distributions for saturated hydraulic conductivity are LN and SB.

Table 2.3 Statistical parameters of matrix saturated hydraulic conductivity for distribution approximation.

HGU	Limits of Variation		Trans- form	Estimated Distribution			Critical value (T [*])		
	A	B		Mean	Variance	T	α =0.10	α =0.05	α =0.01
CCR&CUC ^a									
CUL&CW	2.48E-13	1.25E-08	LN	-25.40	8.37	0.140	0.189	0.206	0.245
CMW	3.33E-12	9.42E-08	SB	-6.06	67.5	0.323	0.315	0.337	0.405
CNW ^c	5.11E-12	8.80E-07	LN	-18.2	22.2	0.235	0.239	0.258	0.294
BT4 ^c	1.79E-10	2.55E-05	LN	-14.2	10.6	0.207	0.230	0.249	0.284
TPY ^a									
BT3 ^c	1.89E-09	7.31E-06	X ^{1/3}	1.04E-02	2.40E-06	0.236	0.230	0.249	0.284
TPP	8.99E-08	1.75E-06	SB	0.754	16.9	0.209	0.230	0.249	0.284
BT2 ^c	1.23E-09	2.07E-05	LN	-13	6.61	0.192	0.171	0.187	0.225
TC	1.69E-11	1.69E-07	SB	-5.23	42.8	0.172	0.294	0.319	0.364
TR	1.69E-11	9.38E-06	LN	-20.3	4.47	0.133	0.117	0.129	0.150
TUL	4.19E-13	1.43E-06	LN	-22.8	7.29	0.163	0.132	0.146	0.169
TMN	4.75E-13	1.24E-09	LN	-25.8	2.32	0.134	0.094	0.103	0.120
TLL	1.38E-12	7.66E-08	LN	-22.3	6.42	0.096	0.112	0.123	0.143
TM2&TM1	5.32E-13	9.40E-06	SB	-12.4	33.4	0.140	0.168	0.183	0.219
PV3	8.62E-14	2.26E-09	LN	-25.8	7.25	0.154	0.189	0.206	0.245
PV2a ^a									
PV2v ^b	5.02E-11	1.21E-05	X ^{1/3}	1.26E-02	1.26E-05	0.211	0.195	0.213	0.250
BT1a	1.82E-13	8.71E-08	SB	-7.16	59.2	0.189	0.239	0.258	0.294
BT1v	1.03E-10	2.21E-05	LN	-14.1	6.48	0.131	0.136	0.150	0.174
CHV ^b	1.67E-12	7.21E-05	X ^{1/3}	0.0168	1.34E-04	0.144	0.117	0.129	0.150
CHZ ^b	3.87E-13	9.55E-08	LN	-24.1	1.83	0.118	0.081	0.089	0.104
BTa	2.07E-13	2.11E-10	SB	-3.80	26.3	0.182	0.249	0.271	0.311
BTv ^a									
PP4	8.43E-13	3.09E-07	SB	-7.11	52.3	0.239	0.261	0.285	0.331
PP3	4.19E-12	3.66E-07	X ^{1/3}	3.72E-03	1.62E-06	0.114	0.113	0.124	0.144
PP2	3.74E-12	1.16E-08	LN	-22.2	5.05	0.101	0.136	0.150	0.174
PP1	1.69E-12	1.95E-06	LN	-22.6	10.4	0.149	0.152	0.167	0.195
BF3 ^c	6.89E-11	5.59E-08	LN	-20.0	7.32	0.191	0.276	0.300	0.348
BF2 ^a									

Note: (a) the sample size is less than 4 and can not fit the distribution using Lilliefors Test in the layers.
(b) The outlying values were discarding but were included for goodness of fit calculation in the layer.
(c) The distribution is not best fit in order to guarantee the reasonable ranges of random fields.

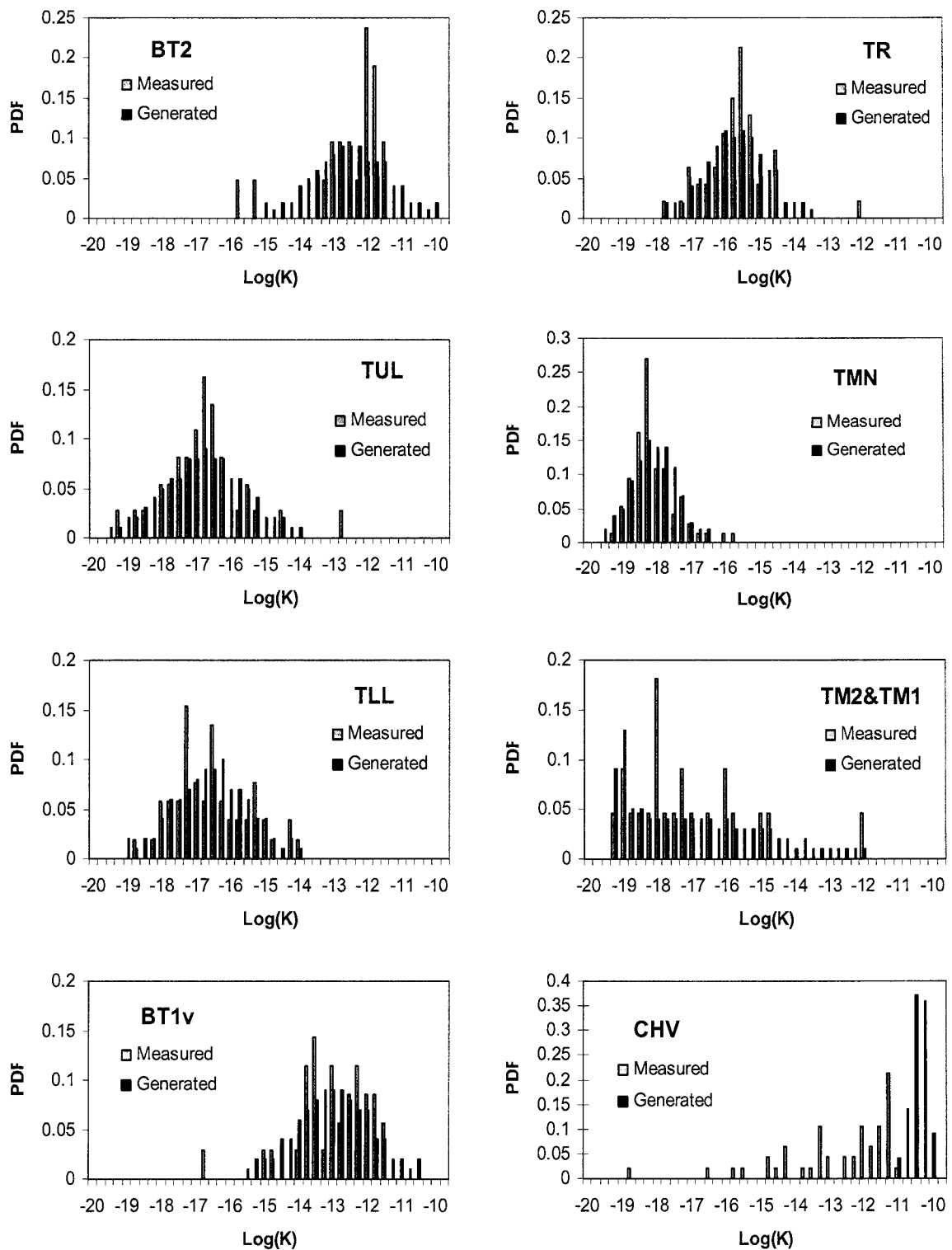


Figure 2.3 Histograms of measured and generated data of matrix log permeability for some model layers.

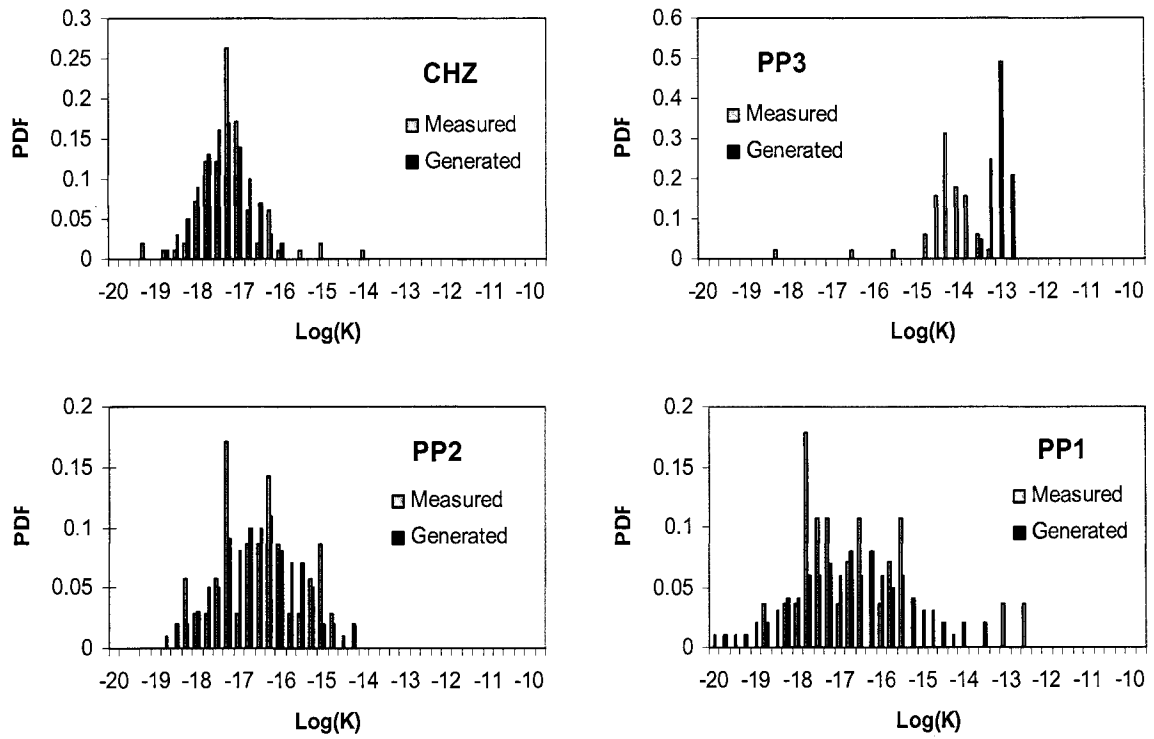


Figure 2.3 (Cont.) Histograms of measured and generated data of matrix log permeability for some model layers.

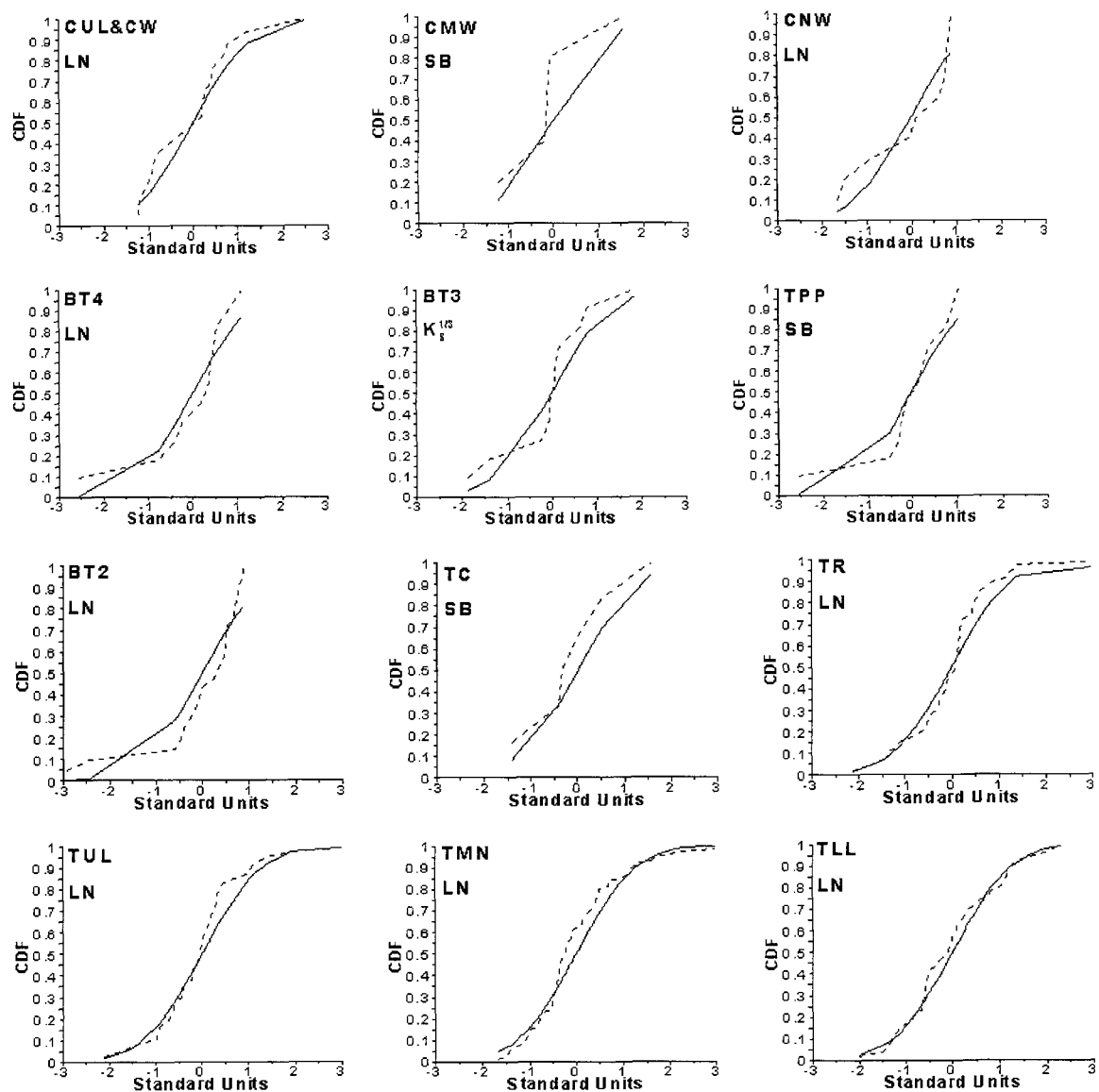


Figure 2.4 Empirical and theoretical distributions for transformed saturated conductivity in each model layer.

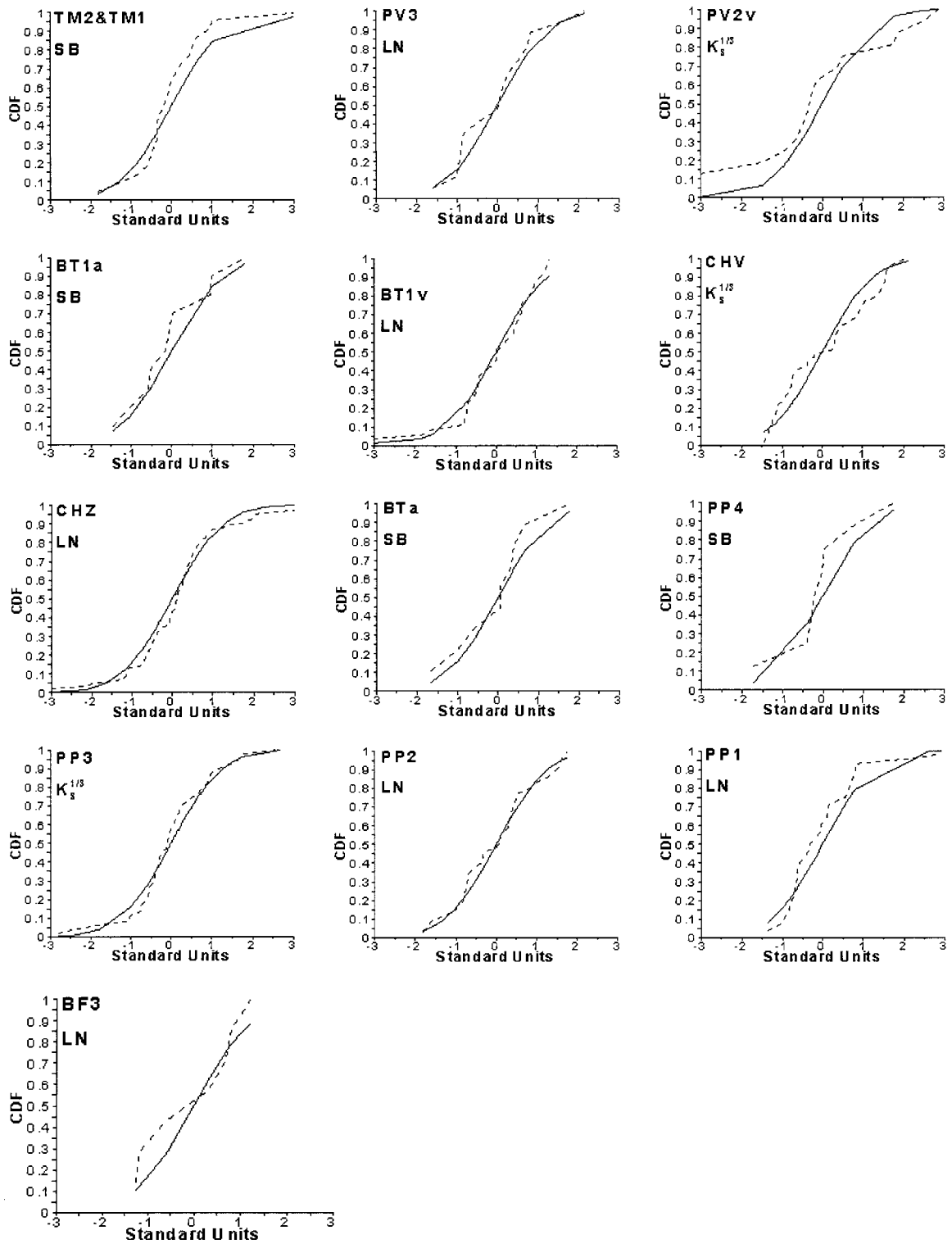


Figure 2.4 (Cont.) Empirical and theoretical distributions for transformed conductivity in each model layer.

2.2.4 Transformation and Distribution of Matrix Sorption Coefficient

The sorption coefficient (K_d) of the reactive tracer is the most important factor in transport simulations and has significant effects on the residence time of radionuclide in the unsaturated zone of Yucca Mountain. The measured sorption coefficients for the reactive tracer Neptunium (Np) in three types of rocks (Devitrified, Vitric and Zeolite tuffs) are obtained from Yucca Mountain Database (DTN: LA0407AM831341.004). The descriptive statistics of sorption coefficient for Np are tabulated in Table 2.4. From Table 2.4, one can see that the sample size is large enough to determine the distributions of the parameter in three types of rocks. One can also know that the spatial heterogeneity in sorption coefficient exists in the three types of rocks because of significant difference of measured data. The measured K_d values have broad ranges from 0.008 to 8.235 mL/g in devitrified tuff, from 0.020 to 4.071 in vitric tuff and from 0.032 to 8.742 mL/g in zeolitic tuff. The heterogeneity of K_d can cause significant uncertainties on radionuclide transport and the effects of heterogeneous K_d should be assessed for uncertainty analysis. The histograms of sorption coefficient for three rock types are shown in Figure 2.5. The histograms of the generated random fields of sorption coefficient are also plotted in Figure 2.5. One can observe that the sorption coefficient of neptunium has a lognormal distribution in Devitrified and Vitric Tuffs.

After implementing Lillifors Test and transformations, the estimations of best transformations and corresponding probability properties for sorption coefficient in three rock types are tabulated in Table 2.5. The empirical and fitted CDF of the best fitting distribution for K_d in the three rock types are shown in Figure 2.6. One can know from Table 2.5 the tests in Devitrified and Zeolitic tuffs are accepted in the level of

significance $\alpha = 0.1$ and another test in Vitric tuff is accepted in the level of $\alpha = 0.05$. The best transformations of sorption coefficient for devitrified and vitric tuffs are lognormal and one for zeolitic tuff was $X^{1/2}$.

The results of distributions determination of parameters are the basis of random field generation for Monte Carlo Simulation and also have important effects on final Monte Carlo Simulation results because the input of the simulations would be obtained based on the determined distributions.

Table 2.4 Descriptive statistics for sorption coefficient of neptunium.

Materials	Sorption Coefficient (K_d , mL/g) of Neptunium (Np)				
	Mean	Stand Deviation	Minimum	Maximum	Sample Size (N)
Devitrified Tuff	0.720	1.006	0.008	8.235	233
Vitric Tuff	0.808	0.855	0.020	4.071	216
Zeolitic Tuff	2.333	1.589	0.032	8.742	264

Table 2.5 Statistical parameters of sorption coefficient of neptunium for distribution approximation.

Materials	Limits of Variation		Trans -form	Estimated Distribution			Critical Values (T)		
	A	B		Mean	Variance	T	$\alpha=0.10$	$\alpha=0.05$	$\alpha=0.01$
Devitrified Tuff	0.007	8.236	LN	-1.06	1.67	0.0396	0.0527	0.0580	0.0675
Vitric Tuff	0.018	4.072	LN	-0.73	1.18	0.0588	0.0548	0.0603	0.0702
Zeolitic Tuff	0.031	8.743	$X^{1/2}$	1.43	0.293	0.0382	0.0495	0.0545	0.0635

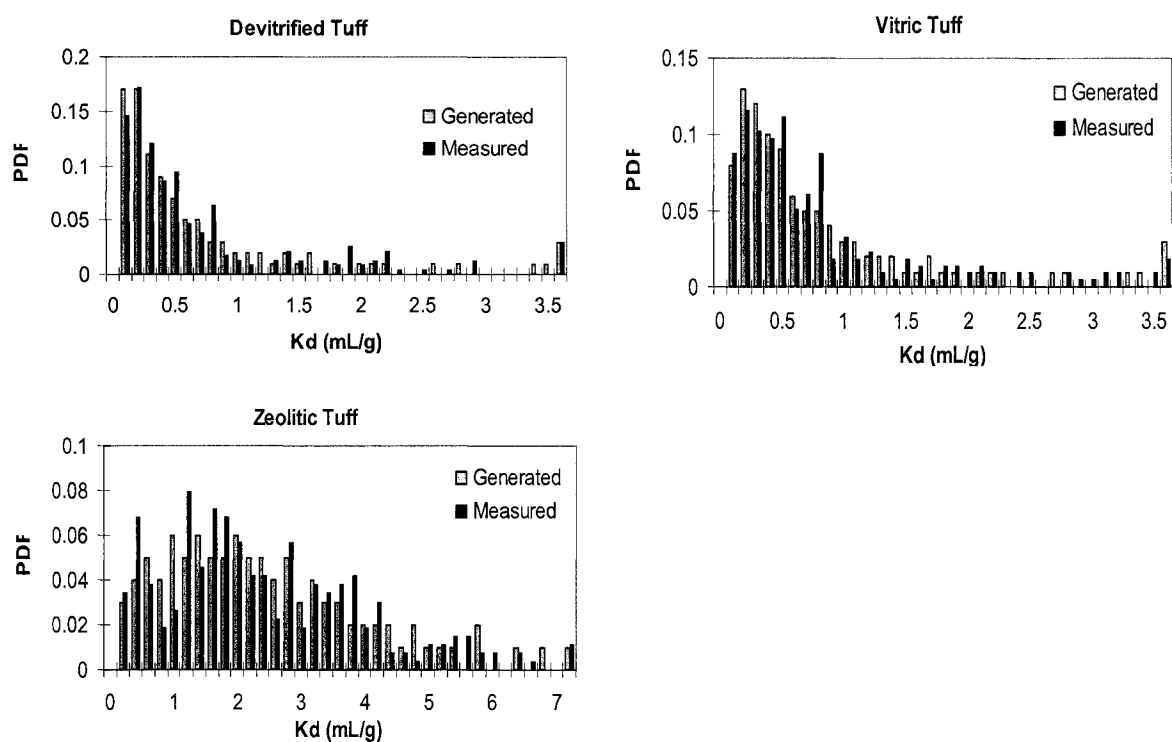


Figure 2.5 Histograms of measured and generated data of sorption coefficient of neptunium for devitrified, vitric and zeolitic tuffs.

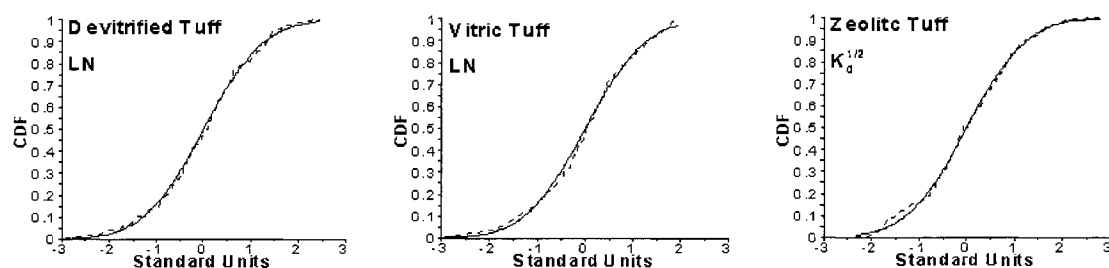


Figure 2.6 Empirical and theoretical distributions for transformed sorption coefficient of neptunium in Devitrified, Vitric and Zeolitic tuffs.

2.3 Random Field Generation of Hydraulic Parameters

The hydraulic parameters such as matrix porosity, saturated hydraulic conductivity and sorption coefficient are treated as statically homogenous random variables. The random fields of the parameters are generated to evaluate the uncertainty of flow and transport. In this study, Latin Hypercube Sampling (LHS) is used to generate random fields based on the distributions and their corresponding mean and variance determined in Section 2.2.

2.3.1 Latin Hypercube Sampling

Latin Hypercube Sampling (LHS) is one of sampling methods and can be used to address the need for uncertainty assessment (Swiler and Wyss, 2004; Helton and Davis, 2000; McKay et al., 1979). LHS ensures that generated random samples span the full coverage of a random variable even when the sample size is relatively small. This overcomes the disadvantage of the random sampling method that it possibly overemphasizes or omits the samples in some parts when the sample size is not enough large. This property of LHS reduces the computational cost of Monte Carlo simulations, since smaller number of random realizations is needed to represent parameter uncertainty.

The sampling procedure of LHS for multiple uncorrelated random variables is as follows (Helton and Davis, 2000; Swiler and Wyss, 2004):

- (1) Divide the CDF of a random variable with equal probability into N intervals and obtain the corresponding range of CDF for each interval;
- (2) Generate one random value from a uniform distribution on each interval of the CDF and identify the corresponding value of the random variable from the CDF;
- (3) Pair the obtained N values for the first variable with the N values of the

second variable randomly;

- (4) Combine these N pairs in a random manner with the N values of the third variable to form n triplets and continue pairing until the last variable is combined with others.

If the random variables are correlated, it is necessary to incorporate the correlations into the samples because the random pairing cannot represent the correlations. Iman and Conover (1982) proposed a method for restricting the pairing of variables based on a desired rank correlation matrix to generate correlated random samples. The properties of this technique are (Iman and Conover, 1982): (1) Distribution free; (2) Simple; and (3) generated original values are retained and only the pairing is affected by the desired rank correlations.

Correlation is measured in this study using the Spearman rank correlation

$R_{x_j x_k}$ between two variables x_j and x_k (Helton and Davis, 2003):

$$R_{x_j x_k} = \frac{\sum_{i=1}^N [R(x_{ij}) - \bar{R}(x_j)] [R(x_{ik}) - \bar{R}(x_k)]}{\left\{ \sum_{i=1}^N [R(x_{ij}) - \bar{R}(x_j)]^2 \right\}^{1/2} \left\{ \sum_{i=1}^N [R(x_{ik}) - \bar{R}(x_k)]^2 \right\}^{1/2}} \quad (2.6)$$

where $R(x_{ij})$ and $R(x_{ik})$ are the ranking index of x_{ij} and x_{ik} in ascending order,

respectively; N is the sample size; and $\bar{R}(x_j) = \bar{R}(x_k) = (N + 1) / 2$. Equation (2.6) can

also be written as:

$$r = 1 - 6 \sum_{i=1}^N \frac{d_i^2}{N(N^2 - 1)} \quad (2.7)$$

where r is Spearman rank correlation coefficient and d is the difference in rank index of the corresponding variables. In this study, matrix porosity and saturated hydraulic

conductivity are correlated and their Spearman rank correlation can be calculated in the following steps:

- (1) Collect the available data for saturated hydraulic conductivity and corresponding porosity from Yucca Mountain database;
- (2) Rank two variables in ascending orders and obtain the rank index of saturated hydraulic conductivity and corresponding porosity;
- (3) Calculate the difference between the rank index of two variables;
- (4) Calculate the Spearman rank correlation according to equation (2.7).

One of advantages of the rank correlation used in this study is that it can be quite meaningful with non-normal distributions of the input data (Iman and Conover, 1982; Helton and Davis, 2003). This can overcome the correlation coefficients may lose some meaning when the data are not normal. The rank correlation can also capture the type of subjective information of correlation for uncertainty assessment (Helton and Davis, 2003). The subjective information means that the large or small value for one variable should correspond with large or small values for another variable.

2.3.2 Random Field Generation of Hydraulic Parameters

By implementing LHS with Spearman rank correlation based on the estimations of the best transformations of matrix porosity, saturated hydraulic conductivity and sorption coefficient and their distributional characteristics, the parameter random fields of transformed data following normal distributions can be generated for each model layer by LHS V2.51 code. The numerical code LHS V2.51 requires 1% and 99% quintiles of a normal distribution, which can be calculated according to the mean (μ) and the standard deviation (σ) of the normal distribution. It is written as (Swiler and Wyss, 2004):

$$V_{0.01} = \mu - 2.326\sigma ; \quad V_{0.99} = \mu + 2.326\sigma \quad (2.8)$$

where μ and σ of matrix porosity, saturated hydraulic conductivity, and sorption coefficient are listed in Tables 2.2, 2.3, and 2.5, respectively.

Since the generated random numbers are subject to the transforms listed in Table 2.2, 2.3 and 2.5, they need to be transformed back to the original scale for Monte Carlo simulation. The equations of inverse transformation for Johnson transformations are as follows (Carsel and Parrish, 1988):

$$\text{LN: } X = \exp(Y) \quad (2.9)$$

$$\text{SB: } X = [B \exp(Y) + A] / [1 + \exp(Y)] \quad (2.10)$$

$$\text{SU: } X = A + (B - A)[\exp(Y) - \exp(-Y)] / 2 \quad (2.11)$$

where Y is the transformed value following a normal distribution with the estimated mean and variance generated by LHS. The equations of inverse transformation for another four classical re-expression ($1/X$, $X^{1/2}$, $X^{1/3}$ and X^2 transformations are as follows respectively:

$$X = \frac{1}{Y}; \quad X = Y^2; \quad X = Y^3; \quad X = Y^{1/2} \quad (2.12)$$

In this study, the Spearman rank correlation between matrix porosity and saturated hydraulic conductivity is used as the input data of LHS V2.51 code to generate the random fields with correlation between matrix porosity and saturated hydraulic conductivity. The calculated Spearman rank correlations list in Table 2.6, show that the matrix porosity and saturated hydraulic conductivity are correlated in most layers. Nevertheless, the spearman correlation is close to zero in layers BT3 and PV2v.

Table 2.6 Spearman rank correlation between transformed data of matrix porosity and saturated conductivity.

HGU	Spearman rank correlation	Sample size	HGU	Spearman rank correlation	Sample size
CCR&CUC ^b		3	PV3	-0.20	17
CUL&CW	-0.50	17	PV2a ^a		1
CMW	0.60	5	PV2v	0.06	16
CNW	0.61	10	BT1a	0.12	10
BT4	0.26	11	BT1v	0.37	35
TPY ^b		2	CHV	-0.19	47
BT3	0.03	11	CHZ	0.47	99
TPP	-0.47	11	BTa	0.22	9
BT2	0.42	21	BTv ^a		1
TC	-0.49	6	PP4	0.52	8
TR	0.39	47	PP3	0.45	51
TUL	0.40	37	PP2	0.68	35
TMN	0.48	9	PP1	0.24	28
TLL	-0.46	52	BF3	-0.71	7
TM2&TM1	-0.39	22	BF2 ^a		1

Note: (a) Only one measured data point is available for Pv2a, BTv and BF2 respectively;
(b) The measured data points are less than 5 in CCR&CUC and TPY.

2.3.2.1 Random Field Generation of Matrix Porosity

The measured and generated data for matrix porosity are compared in Figure 2.1 by plotting their histograms. Figure 2.1 shows that the measured data match well with generated porosity in most layers and it illustrates that the generated random fields represent the distribution of porosity in the layers. The percentiles of measured and generated random fields of matrix porosity are listed in Table 2.7 and plotted in Figure 2.7 as a Q-Q plot. Table 2.7 and Figure 2.7 illustrate that the characterizing statistics of with the measured parameters and generated random fields agree well, except in lower

and upper percentiles in few layers where the outliers in measurements are discarded in the layers when the mean and variance are calculated to generate the random fields.

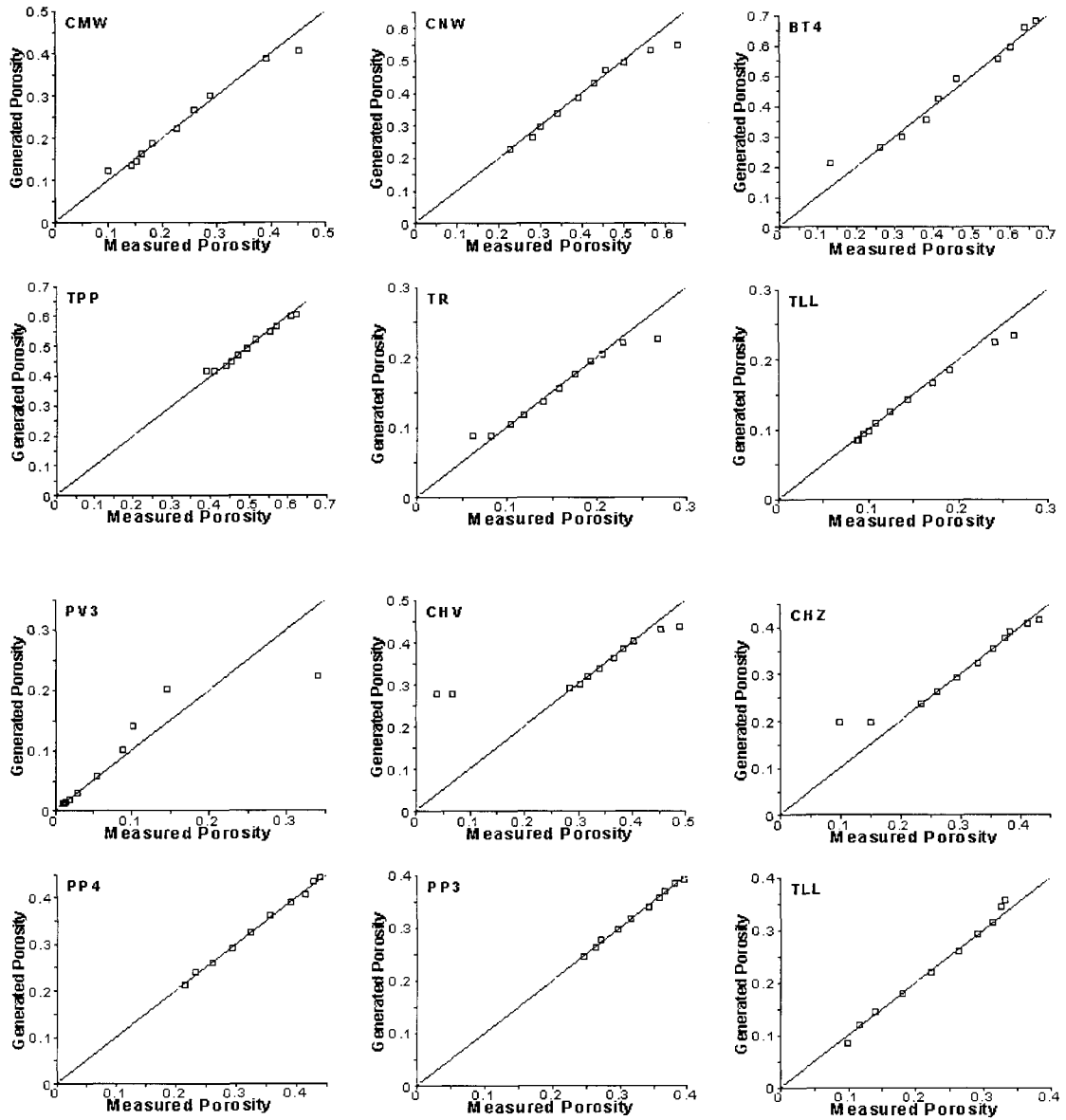


Figure 2.7 Q-Q plot of matrix porosity for measured and generated porosity in some layers.

Table 2.7 Percentiles of measured and generated data of matrix porosity.

HGU Percentile	CCR&CUC		CUL&CW		CMW		CNW	
	Measured	Generated	Measured	Generated	Measured	Generated	Measured	Generated
1%	0.038	0.054	0.050	0.047	0.100	0.123	0.228	0.227
5%	0.064	0.134	0.055	0.052	0.143	0.134	0.283	0.267
10%	0.124	0.169	0.058	0.057	0.152	0.144	0.299	0.296
25%	0.219	0.211	0.065	0.065	0.163	0.162	0.340	0.338
50%	0.254	0.249	0.078	0.079	0.182	0.188	0.392	0.386
75%	0.278	0.282	0.105	0.098	0.227	0.222	0.430	0.433
90%	0.322	0.308	0.138	0.127	0.258	0.265	0.457	0.473
95%	0.333	0.322	0.153	0.154	0.287	0.302	0.501	0.497
99%	0.370	0.343	0.176	0.236	0.392	0.388	0.567	0.534
Minimum	0.038	0.054	0.032	0.047	0.100	0.123	0.228	0.227
Maximum	0.431	0.350	0.213	0.259	0.452	0.406	0.633	0.547
Sample size	124	200	694	200	96	200	104	200

HGU Percentile	BT4		TPY		BT3		TPP	
	Measured	Generated	Measured	Generated	Measured	Generated	Measured	Generated
1%	0.134	0.210	0.073	0.042	0.137	0.233	0.410	0.418
5%	0.262	0.262	0.093	0.126	0.309	0.275	0.441	0.435
10%	0.317	0.299	0.168	0.161	0.327	0.306	0.454	0.447
25%	0.384	0.357	0.188	0.202	0.355	0.354	0.469	0.469
50%	0.414	0.423	0.246	0.240	0.395	0.409	0.493	0.494
75%	0.460	0.492	0.280	0.272	0.470	0.466	0.517	0.521
90%	0.568	0.555	0.291	0.297	0.519	0.519	0.555	0.549
95%	0.601	0.596	0.299	0.311	0.557	0.553	0.572	0.568
99%	0.640	0.659	0.307	0.331	0.571	0.605	0.610	0.601
Minimum	0.134	0.210	0.073	0.042	0.137	0.233	0.388	0.418
Maximum	0.669	0.682	0.309	0.338	0.578	0.625	0.623	0.607
Sample size	58	200	39	200	73	200	159	200

HGU Percentile	BT2		TC		TR		TUL	
	Measured	Generated	Measured	Generated	Measured	Generated	Measured	Generated
1%	0.124	0.275	0.012	0.009	0.082	0.088	0.080	0.084
5%	0.286	0.338	0.019	0.015	0.104	0.105	0.101	0.102
10%	0.365	0.385	0.024	0.021	0.118	0.118	0.115	0.115
25%	0.460	0.452	0.031	0.032	0.140	0.136	0.134	0.133
50%	0.515	0.511	0.049	0.048	0.157	0.156	0.157	0.154
75%	0.550	0.553	0.067	0.069	0.175	0.176	0.178	0.175
90%	0.577	0.576	0.085	0.091	0.192	0.194	0.192	0.193
95%	0.598	0.586	0.107	0.107	0.205	0.204	0.201	0.204
99%	0.609	0.596	0.157	0.133	0.228	0.220	0.223	0.220
Minimum	0.104	0.275	0.012	0.009	0.062	0.088	0.076	0.084
Maximum	0.614	0.599	0.273	0.144	0.267	0.226	0.250	0.226
Sample size	176	200	75	200	449	200	438	200

Table 2.7 (Cont.) Percentiles of measured and generated data of matrix porosity.

HGU	TMN		TLL		TM2&TM1		PV3	
Percentile	Measured	Generated	Measured	Generated	Measured	Generated	Measured	Generated
1%	0.065	0.071	0.089	0.085	0.067	0.070	0.011	0.011
5%	0.080	0.079	0.095	0.093	0.080	0.075	0.012	0.012
10%	0.089	0.086	0.100	0.098	0.084	0.080	0.014	0.013
25%	0.097	0.096	0.108	0.109	0.089	0.088	0.019	0.018
50%	0.109	0.108	0.123	0.125	0.097	0.099	0.029	0.030
75%	0.120	0.123	0.144	0.143	0.110	0.112	0.054	0.058
90%	0.137	0.136	0.171	0.166	0.130	0.127	0.088	0.102
95%	0.148	0.146	0.190	0.185	0.147	0.139	0.101	0.140
99%	0.169	0.160	0.241	0.225	0.180	0.164	0.145	0.202
Minimum	0.055	0.071	0.088	0.085	0.053	0.070	0.011	0.011
Maximum	0.192	0.166	0.263	0.233	0.341	0.169	0.340	0.223
Sample size	277	200	502	200	300	200	125	200
HGU	PV2v		BT1a		BT1v		CHV	
Percentile	Measured	Generated	Measured	Generated	Measured	Generated	Measured	Generated
1%	0.048	0.050	0.158	0.179	0.031	0.127	0.067	0.278
5%	0.054	0.057	0.207	0.202	0.176	0.176	0.285	0.291
10%	0.069	0.069	0.220	0.220	0.204	0.212	0.304	0.301
25%	0.130	0.113	0.252	0.248	0.264	0.264	0.319	0.318
50%	0.262	0.223	0.277	0.281	0.320	0.322	0.340	0.339
75%	0.358	0.355	0.319	0.318	0.390	0.380	0.366	0.362
90%	0.380	0.425	0.349	0.351	0.420	0.430	0.383	0.386
95%	0.415	0.447	0.379	0.373	0.440	0.460	0.403	0.402
99%	0.446	0.462	0.395	0.407	0.478	0.505	0.454	0.431
Minimum	0.048	0.050	0.158	0.179	0.031	0.127	0.038	0.278
Maximum	0.470	0.465	0.400	0.419	0.510	0.521	0.490	0.437
Sample size	49	200	46	200	80	200	130	200
HGU	CHZ		PP4		PP3		PP2	
Percentile	Measured	Generated	Measured	Generated	Measured	Generated	Measured	Generated
1%	0.151	0.198	0.216	0.211	0.247	0.245	0.099	0.086
5%	0.235	0.236	0.233	0.240	0.264	0.263	0.116	0.120
10%	0.262	0.261	0.262	0.261	0.272	0.276	0.140	0.144
25%	0.293	0.293	0.293	0.292	0.297	0.296	0.180	0.180
50%	0.329	0.325	0.323	0.326	0.317	0.317	0.223	0.220
75%	0.354	0.354	0.356	0.360	0.344	0.339	0.263	0.259
90%	0.375	0.377	0.392	0.389	0.358	0.357	0.291	0.293
95%	0.384	0.390	0.415	0.407	0.366	0.369	0.313	0.314
99%	0.414	0.409	0.428	0.434	0.382	0.385	0.326	0.345
Minimum	0.099	0.198	0.216	0.211	0.246	0.245	0.099	0.086
Maximum	0.433	0.416	0.440	0.443	0.395	0.391	0.333	0.356
Sample size	520	200	56	200	168	200	127	200

Table 2.7 (Cont.) Percentiles of measured and generated data of matrix porosity

HGU	PP1		BF3		BF2	
Percentile	Measured	Generated	Measured	Generated	Measured	Generated
1%	0.178	0.179	0.059	0.064	0.160	0.153
5%	0.213	0.216	0.067	0.072	0.163	0.166
10%	0.227	0.239	0.072	0.079	0.179	0.177
25%	0.275	0.269	0.093	0.093	0.195	0.197
50%	0.301	0.299	0.116	0.116	0.223	0.224
75%	0.326	0.326	0.168	0.152	0.272	0.258
90%	0.345	0.348	0.244	0.212	0.313	0.301
95%	0.358	0.361	0.334	0.279	0.320	0.335
99%	0.389	0.379	0.368	0.576	0.326	0.409
Minimum	0.164	0.179	0.059	0.064	0.160	0.153
Maximum	0.426	0.385	0.369	0.694	0.329	0.424
Sample size	280	200	105	200	40	200

2.3.2.2 Random Field Generation of Matrix Permeability

Since measurements of saturated hydraulic conductivity are obtained from the Yucca mountain database, random fields of saturated hydraulic conductivity (K , m/s) are generated and then converted to TOUGH2 required permeability (k , m²) using the equation:

$$k = \frac{K \mu_w}{g \rho_w} \quad (2.13)$$

Where μ_w is the viscosity of water (0.001 N s/m²), g is the acceleration of gravity (9.81 m/s²) and ρ_w is the density of water (998 kg/m³).

Because of the relatively small sample size of matrix saturated hydraulic conductivity in the layers of CCR&CUC, TPY, PV2a, BTv and BF2, the distribution of matrix saturated hydraulic conductivity cannot be identified for these layers. Therefore, matrix saturated hydraulic conductivity in the layers is treated as deterministic variable and the values of model input data of Wu et al. (2004a) are used in each Monte Carlo

simulation. The minimum and maximum values of measured and generated log permeability data are compared with the model input data (Wu et al., 2004a) for thermal domain in Figure 2.8, which shows that the model input data of matrix permeability of Wu et al. (2004a) in most layers are within the ranges of measured data and are larger than the maximum of measured data in the layers of BT3, TPP, CHV, PP3 and BF2 (the layer numbers are shown in Table 1.1). To make generated random fields cover the model input data of Wu et al. (2004), the values of model input data by

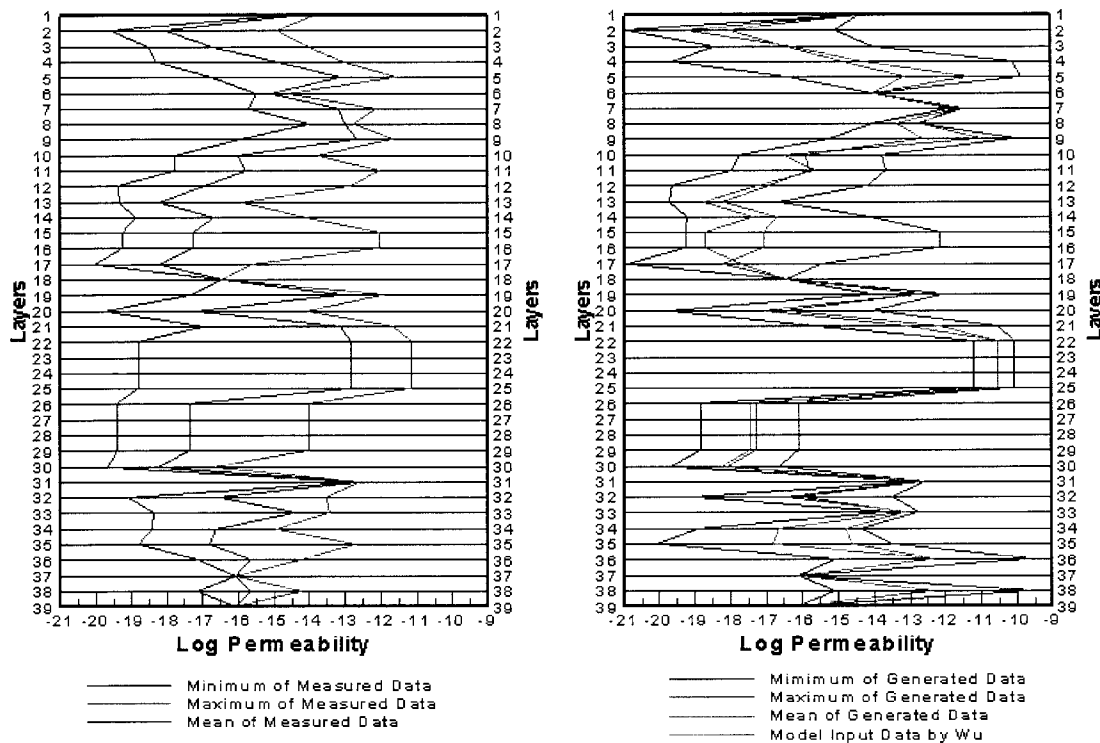


Figure 2.8 Comparison of measured data (Mean, Minimum and Maximum) and generated data (Mean, Minimum and Maximum) and model input data of Wu et al. (2004a) for Thermal domain of matrix log permeability in each model layer (Layer numbers from 1 to 39 represent the model layers shown in Table 1.1).

Wu et al. (2004a) are assumed as the means of the distributions and the variances are the ones determined by Lilliefors Test to generate the random fields of matrix permeability for the layers of BT3, TPP, CHV, PP3 and BF2. One can also see from Figure 2.8 that the model input data of Wu et al. (2004a) are within the ranges of generated data.

200-realization random fields of matrix saturated hydraulic conductivity are generated and these realizations are correlated with matrix porosity through the Spearman rank correlations for each model layer. Then they are transformed back to original scale according to the selected transforms in the layers. Based on Equation (2.13), the random fields of matrix saturated hydraulic conductivity are converted to the matrix permeability.

Figure 2.3 shows the histograms of the measured and generated data for matrix permeability. For the convenience of presenting, log matrix permeability, instead of matrix permeability, is plotted. One can see from Figure 2.3 that there is a good match between measured and generated data in some layers but not good in few layers such as TM2&TM1, CHV and PP3 layers. One of the reasons is small sample size and some outliers in the layers. Another reason is that the model input data by Wu et al. (2004a) is assumed as the mean of generated random fields. Table 2.8 tabulates the percentiles of measured and generated log matrix permeability and Figure 2.9 shows Q-Q plots of the percentiles for some layers whose sample sizes are larger than 20. Table 2.8 and Figure 2.9 show that the measured data match well with generated random fields between 5% and 95% percentiles of matrix permeability except for the certain layers whose means are assumed from the model input data of Wu et al. (2004a). Comparing Table 2.8 and Figure 2.9 with Table 2.7 and Figure 2.7 (for porosity) show that the matches between the

measured data and generated random fields in matrix porosity are better than the one in matrix permeability due to the large sample size of porosity.

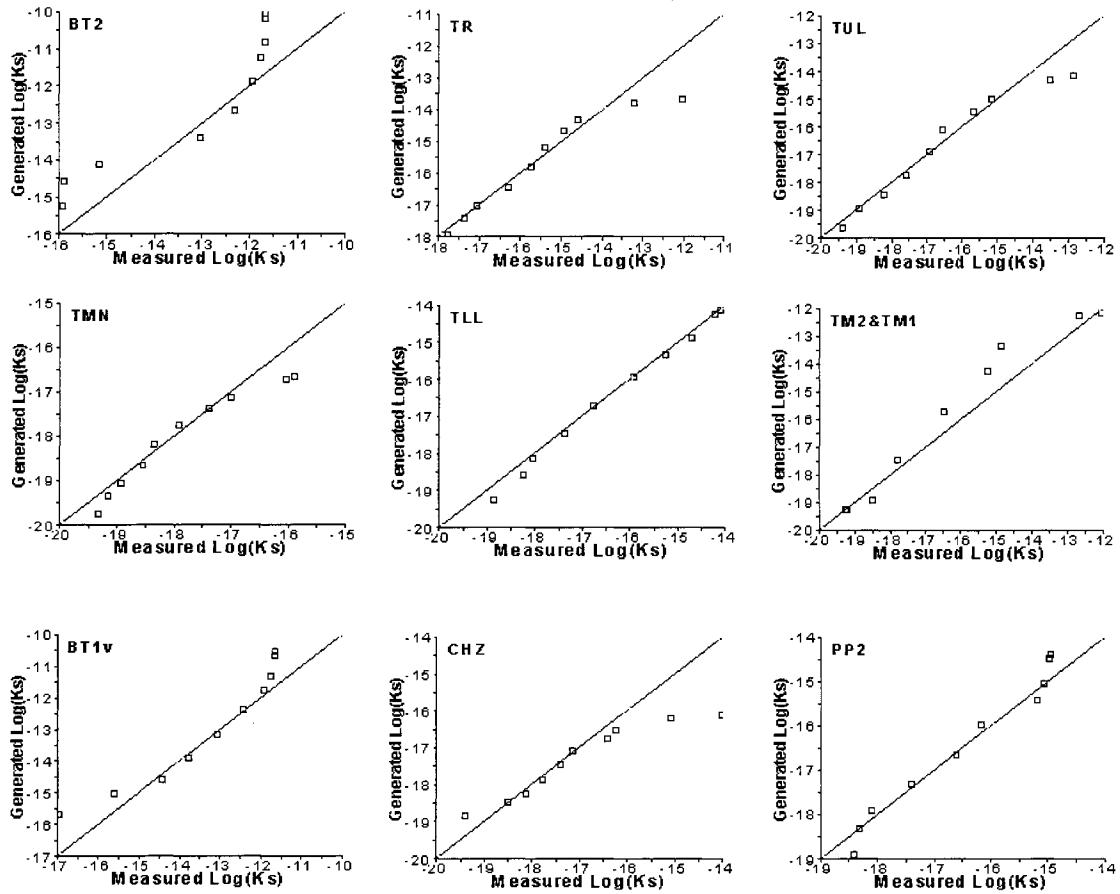


Figure 2.9 Q-Q plot of measured and generated matrix log permeability in some layers.

Table 2.8 Percentiles of measured and generated data of log permeability.

HGU	BT2		TR		TUL		TMN	
Percentile	Measured	Generated	Measured	Generated	Measured	Generated	Measured	Generated
1%	-15.90	-15.23	-17.76	-17.94	-19.37	-19.62	-19.31	-19.73
5%	-15.87	-14.57	-17.36	-17.39	-18.92	-18.92	-19.15	-19.34
10%	-15.15	-14.11	-17.08	-17.02	-18.20	-18.44	-18.93	-19.07
25%	-13.05	-13.42	-16.29	-16.45	-17.61	-17.71	-18.55	-18.66
50%	-12.31	-12.65	-15.76	-15.82	-16.95	-16.91	-18.36	-18.21
75%	-11.93	-11.89	-15.41	-15.19	-16.55	-16.10	-17.92	-17.75
90%	-11.77	-11.25	-14.94	-14.67	-15.65	-15.44	-17.40	-17.37
95%	-11.69	-10.82	-14.61	-14.32	-15.17	-14.99	-17.01	-17.12
99%	-11.68	-10.18	-13.20	-13.78	-13.51	-14.31	-16.03	-16.74
Minimum	-15.90	-15.23	-17.76	-17.94	-19.37	-19.62	-19.31	-19.73
Maximum	-11.68	-10.04	-12.02	-13.67	-12.84	-14.17	-15.90	-16.66
Sample size	21	200	47	200	37	200	74	200

HGU	TLL		TM2&TM1		BT1v		CHV	
Percentile	Measured	Generated	Measured	Generated	Measured	Generated	Measured	Generated
1%	-18.85	-19.24	-19.26	-19.27	-16.97	-15.69	-18.77	-11.21
5%	-18.24	-18.58	-19.26	-19.26	-15.61	-15.02	-16.31	-10.99
10%	-18.05	-18.12	-19.22	-19.25	-14.43	-14.57	-15.14	-10.87
25%	-17.37	-17.45	-18.49	-18.91	-13.78	-13.89	-13.72	-10.70
50%	-16.76	-16.69	-17.79	-17.43	-13.09	-13.13	-12.31	-10.53
75%	-15.92	-15.93	-16.49	-15.71	-12.42	-12.37	-11.62	-10.38
90%	-15.26	-15.31	-15.23	-14.29	-11.92	-11.74	-11.36	-10.27
95%	-14.71	-14.89	-14.86	-13.35	-11.77	-11.32	-11.33	-10.20
99%	-14.21	-14.25	-12.64	-12.25	-11.67	-10.68	-11.19	-10.10
Minimum	-18.85	-19.24	-19.26	-19.27	-16.97	-15.69	-18.77	-11.21
Maximum	-14.11	-14.12	-12.02	-12.15	-11.65	-10.54	-11.13	-10.08
Sample size	52	200	22	200	35	200	47	200

HGU	CHZ		PP3		PP2		PP1	
Percentile	Measured	Generated	Measured	Generated	Measured	Generated	Measured	Generated
1%	-19.40	-18.82	-18.37	-13.67	-18.42	-18.90	-18.76	-20.06
5%	-18.50	-18.47	-16.02	-13.52	-18.32	-18.32	-18.56	-19.23
10%	-18.13	-18.23	-14.84	-13.42	-18.10	-17.92	-18.15	-18.65
25%	-17.77	-17.87	-14.55	-13.28	-17.39	-17.32	-17.78	-17.79
50%	-17.40	-17.47	-14.32	-13.15	-16.61	-16.65	-17.26	-16.83
75%	-17.14	-17.06	-14.06	-13.03	-16.17	-15.98	-16.05	-15.86
90%	-16.42	-16.73	-13.82	-12.93	-15.18	-15.42	-15.69	-15.07
95%	-16.26	-16.50	-13.69	-12.87	-15.07	-15.05	-14.14	-14.53
99%	-15.08	-16.16	-13.55	-12.79	-14.96	-14.48	-12.82	-13.72
Minimum	-19.40	-18.82	-18.37	-13.67	-18.42	-18.90	-18.76	-20.06
Maximum	-14.01	-16.09	-13.43	-12.77	-14.93	-14.36	-12.70	-13.55
Sample size	99	200	51	200	35	200	28	200

2.3.2.3 Random Field Generation of Sorption Coefficient

200-realization random fields of sorption coefficient (K_d) are generated. Figure 2.5 shows the good agreement between the measured and generated data of sorption coefficients in three types of rocks and it indicates that the random fields of sorption coefficient can respond the probabilistic distributions of the sorption coefficient. The percentiles of measured and generated random fields in sorption coefficient are compared in Table 2.9 and the Q-Q plots of the percentiles are also shown in Figure 2.10. One can see from Table 2.9 and Figure 2.10 that the measured data match well with generated random fields below 99% percentiles of the data. Therefore, it can be concluded that the generated random fields of sorption coefficient are good.

Table 2.9 Percentiles of measured and generated data of sorption coefficient.

Materials Percentile	Devitrified Tuff		Vitric Tuff		Zeolitic Tuff	
	Measured	Generated	Measured	Generated	Measured	Generated
1%	0.0139	0.0194	0.0296	0.0428	0.137	0.0498
5%	0.0365	0.0423	0.0722	0.0823	0.235	0.302
10%	0.0607	0.0679	0.110	0.123	0.404	0.514
25%	0.152	0.148	0.255	0.236	1.166	1.154
50%	0.390	0.345	0.491	0.481	1.951	2.041
75%	0.762	0.827	0.947	1.002	3.319	3.220
90%	1.899	1.773	2.019	1.901	4.420	4.467
95%	2.337	2.809	2.855	2.798	5.409	5.318
99%	4.584	5.616	3.925	5.009	6.758	6.739
Minimum	0.008	0.0171	0.0199	0.0385	0.0322	0.0292
Maximum	8.235	7.000	4.071	6.030	8.742	7.231
Sample size	233	200	216	200	264	200

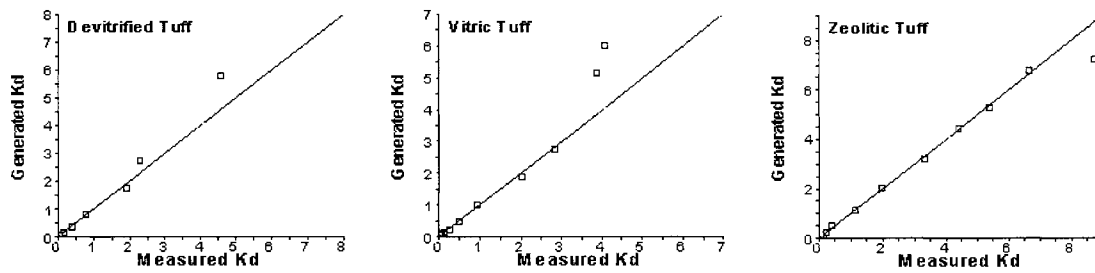


Figure 2.10 Q-Q plot of measured and generated sorption coefficient (K_d) for the three rock types.

2.3.2.4 Comparison of Multiple Random Fields

In Monte Carlo simulation, the random fields generally need to be generated with a large number of realizations. To reduce the computational cost of Monte Carlo simulation, it is necessary to generate the random fields representing the real field characteristics with appropriate realizations. In this study, the comparison of generated random fields in matrix porosity and permeability with 100, 200, 500 and 1,000 realizations are shown in Figure 2.11 and 2.12. Some layers such as BT2, TMN and CHV etc. are selected randomly from all layers to present the comparison. One can see from the figures that there are no big differences among the histograms of generated random fields in porosity and permeability with different realizations. It indicates that the random fields with 200 realizations can represent the real field characteristics of matrix porosity and permeability and can be used to evaluate the uncertainty of flow and radionuclide transport.

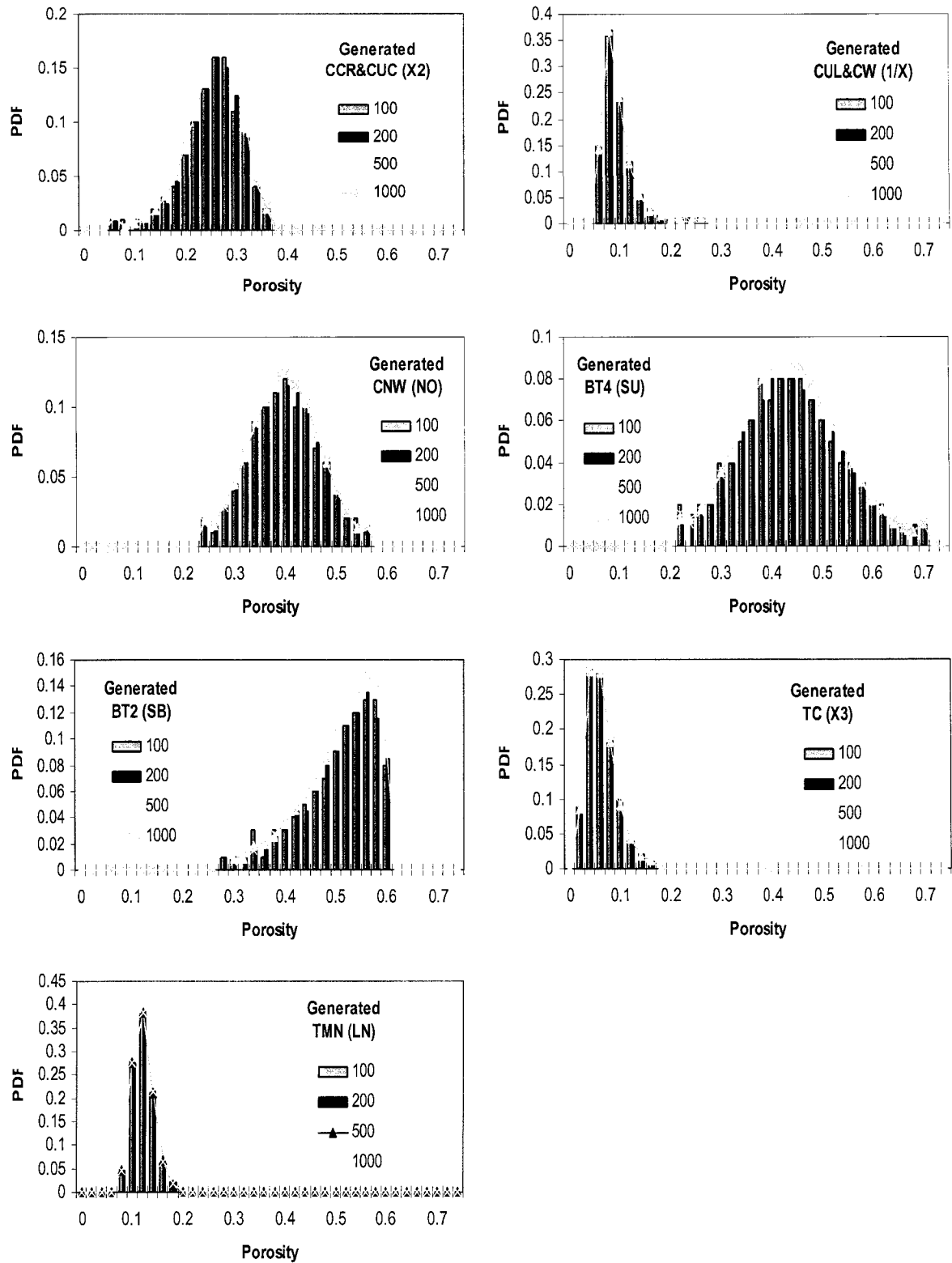


Figure 2.11 Histograms of generated random fields of matrix porosity with 100, 200, 500 and 1000 realizations in few layers.

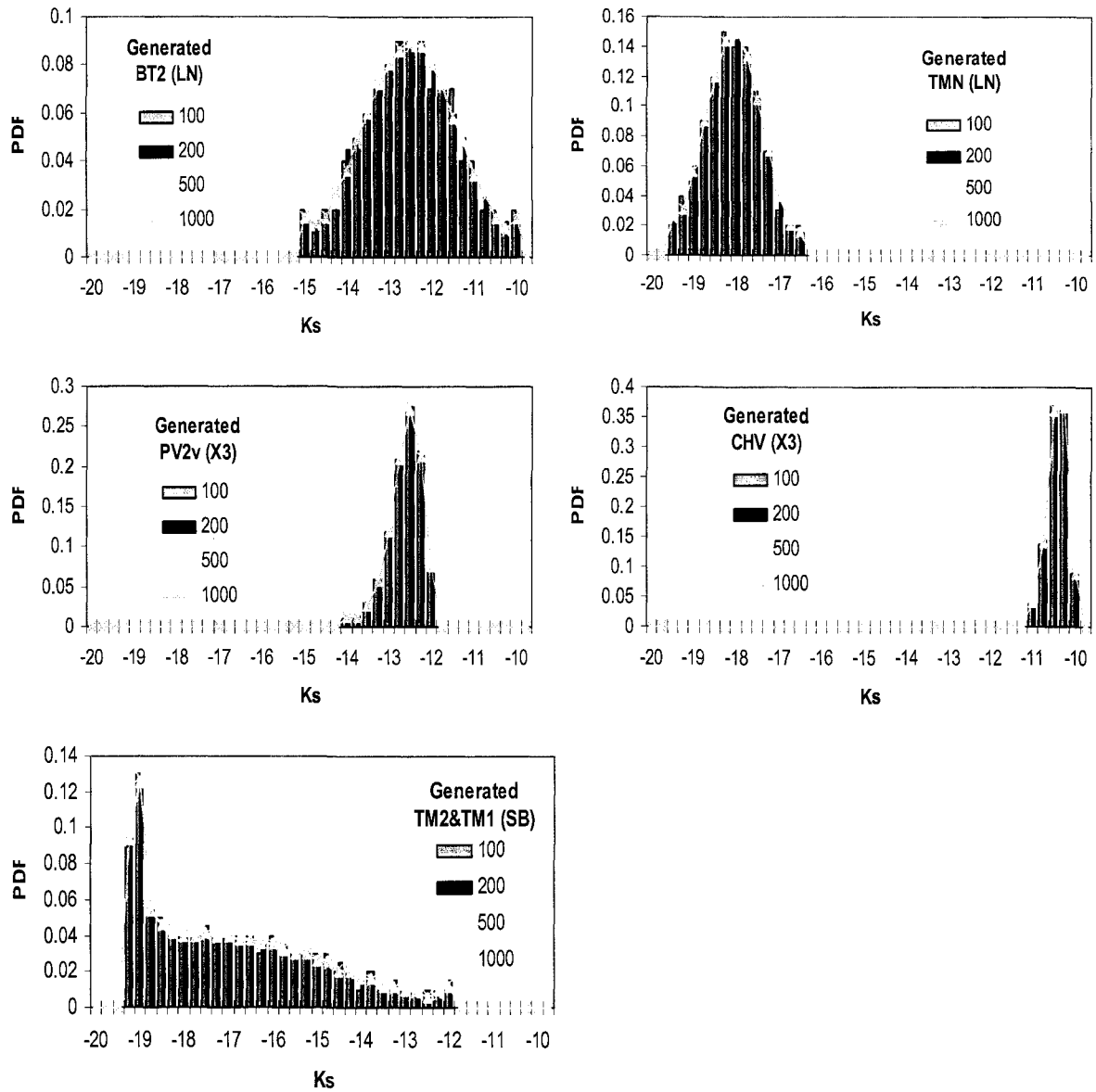


Figure 2.12 Histograms of generated random fields of matrix saturated conductivity with 100, 200, 500 and 1000 realizations in few layers.

CHAPTER 3

UNCERTAINTY ANALYSIS OF UNSATURATED FLOW FIELDS

3.1 Introduction

In this study, Monte Carlo simulation is used to quantify the propagation of the parametric uncertainty in the unsaturated flow field at Yucca Mountain. The random fields of matrix porosity, permeability and sorption coefficient with 200 realizations are generated by Latin Hypercube Sampling (LHS) method in Chapter 2. These random fields are used to generate input files of the TOUGH2 code and unsaturated flow field is simulated for each parameter realization, i.e., each TOUGH2 input file. A recently developed method by Ballio and Guadagnini (2004) is employed to examine the convergence of Monte Carlo Simulation. The means, variances and percentiles of simulated flow variables (e.g., saturation, capillary pressure, and flux) over all realizations are estimated. The means are our optimum predictions and the variances measure the associated predictive uncertainty, which is further quantified by the 5% and 95% percentiles of the 200 realization of the simulated quantities. The detail description about Monte Carlo Simulation, convergence analysis of Monte Carlo approach and TOUGH2 model are in Appendix A.

3.2 Procedures of Monte Carlo Flow Simulation

Monte Carlo simulation is conceptually straightforward. In this study, the random fields of matrix porosity and permeability with 200 realizations are used as the input data of TOUGH2 code. By running TOUGH2 code with the input data for each realization, the unsaturated flow can be simulated. Then, the uncertainty of flow can be evaluated by analyzing output of the overall realizations. In the input files of TOUGH2, only the random matrix porosity and permeability vary in each realization, while other deterministic parameters are fixed. In each Monte Carlo simulation, the element volumes are increased by a factor of 10,000 to overcome convergence difficulty and this approach does not affect the final solution when a steady state is obtained (Wu et al., 2004a). Following Wu et al. (2004a), ground surface and water table are taken as the top and bottom model boundaries, where Dirichlet-type boundary conditions are applied. No-flux boundary condition is specified for the lateral boundaries. The surface infiltration is a source term at the top boundary and a fixed water pressure is used at the bottom boundary. While the system is conceptualized as a steady state one, TOUGH2 requires specifying initial condition, which is adopted from the simulation results with a convergence tolerance of 10^{-3} and the simulation time of 10^{10} years using deterministic model parameters. In this simulation, the convergence tolerance is set as 1,000 and the simulation time is 10^9 years. Several tests with different convergence tolerances have been used to examine the effects of convergence tolerance on the flow simulation results. Simulations are of the same accuracy regardless convergence tolerances, as long as the system reaches steady state. Nevertheless, using a large convergence tolerance reduces computational cost.

Flow simulations are based on steady-state solutions by using EOS9 module. The steady-state solutions are examined by the equivalent inflow and outflow over the entire flow domain. If inflow from infiltration is approximately equal to outflow to water table, this indicates that the flow has reached the steady state for the simulation. Because the infiltration rates over the entire top boundary (inflow) are deterministic for 200 different realizations, the inflow is 2.1804519 kg/s for all of them. The simulated cumulative total-flow rate to water table (outflow) for 200 different realizations vary from 2.1762940 kg/s to 2.1857081 kg/s and the maximum relative error is only 0.241%. Therefore, steady-state solutions are obtained and the mass-balance results for all the realizations are considered good.

3.3 Results Analysis

3.3.1 Convergence of Monte Carlo Simulation

As there are no well-established convergence criteria, the convergence analysis is a major concern in Monte Carlo simulation to ensure that the sample statistics (e.g., mean and variance) obtained from multiple realizations are the ensemble ones. In this study, a recently developed convergence method by Ballio and Guadagnini (2004) is implemented to examine the convergence of groundwater flow simulations. The theoretical description is in Appendix A.

The saturation, capillary pressure, and vertical flux at the elements of PTn bottom, Repository layer (TLL) and PV3 layer are selected to check the convergence of Monte Carlo Simulation. Because the radionuclide would be released from Repository layer, the variables at Repository layer play important roles on overall repository performance.

Because PTn bottom is on the upper of Repository layer and PV3 layer is below the repository, the vertical fluxes and other variables at PTn bottom have significant influences on flow and radionuclide transport at Repository layer and the ones at PV3 layer also are affected by Repository layer. The sample means and variances of the three variables with 95% confidence intervals of simulated saturation, capillary pressure and vertical flux at three elements for 200 realizations are shown in Figure 3.1, 3.2 and 3.3 respectively.

Figure 3.1 shows that the sample means and variances of saturation at three elements in three different layers stabilized after 100 realizations. The 95% confidence intervals decrease with the increase of the realizations, but only vary at negligible level after 150 realizations, indicating convergence of our Monte Carlo simulations. Therefore, sample statistics obtained from the 200 realizations are considered the same as ensemble ones and used to present our optimum predictions and associated predictive uncertainty.

One can notice that the intervals of the first few realizations are extremely large. The reason is that the values of t distribution used for sample mean with small degrees of freedom in Equation (A.6) are much larger than the ones with large degrees of freedom and the values of chi-square distribution with small degrees of freedom in Equation (A.7) used for sample variance are very small.

One can also observe from Figure 3.1 that the sample means increase from PTn bottom, repository to PV3 layer. The sample means of saturation at PTn bottom, repository and PV3 layer are around 0.6, 0.8 and 0.97, respectively. Because the mean of saturated hydraulic conductivity (Table 2.1) decrease from PTn bottom, repository to PV3 layer, the simulated vertical fluxes decrease according to Darcy's law and the

saturation at PV3 layer is almost saturated and is much more saturated than another two layers when the unsaturated system reaches the steady state. The sample variance at the element of repository layer with 200 realizations has no much difference with the one at PTn bottom. They are much larger than the one at PV3 layer. This could be explained by Figure 2.8 that the range of matrix permeability at repository layer is slightly larger than the one at PTn bottom and much larger than the one at PV3 layer.

From Figure 3.2, one can see that the sample means and variances of simulated capillary pressure have similar characteristics and trends as the ones of water saturation. They reach the convergence around 200 realizations and the 95% confidence intervals decrease with the increase of the realizations. The sample means of simulated capillary pressure increase from 0.5, 2.0 to 2.6 (bars) with the increase of depths in unsaturated zone from PTn bottom, Repository to PV3 layer, due to the decrease of volumetric water content determined by saturation and porosity according to the van Geuchten model. Because the mean of porosity generated in Chapter 2 is only 0.043 for PV3 layer and is much smaller than the ones at PTn bottom and repository layer, the volumetric water content is still smaller than the ones at another two layers although the saturation at PV3 layer was almost 1.0.

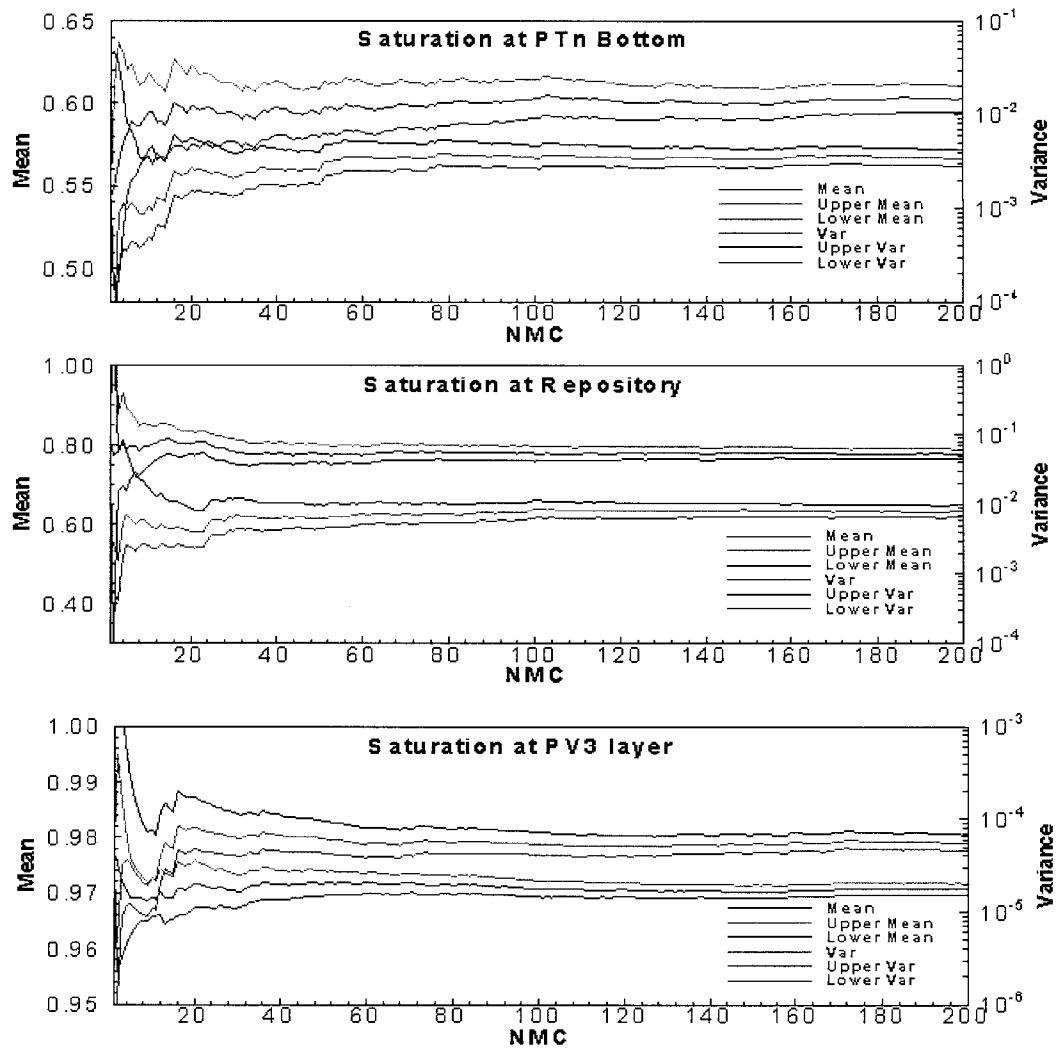


Figure 3.1 Sample mean and variance of simulated water saturation with 95% confidence interval at PTn bottom, Repository layer (TLL) and PV3 layer for three-dimensional domain.

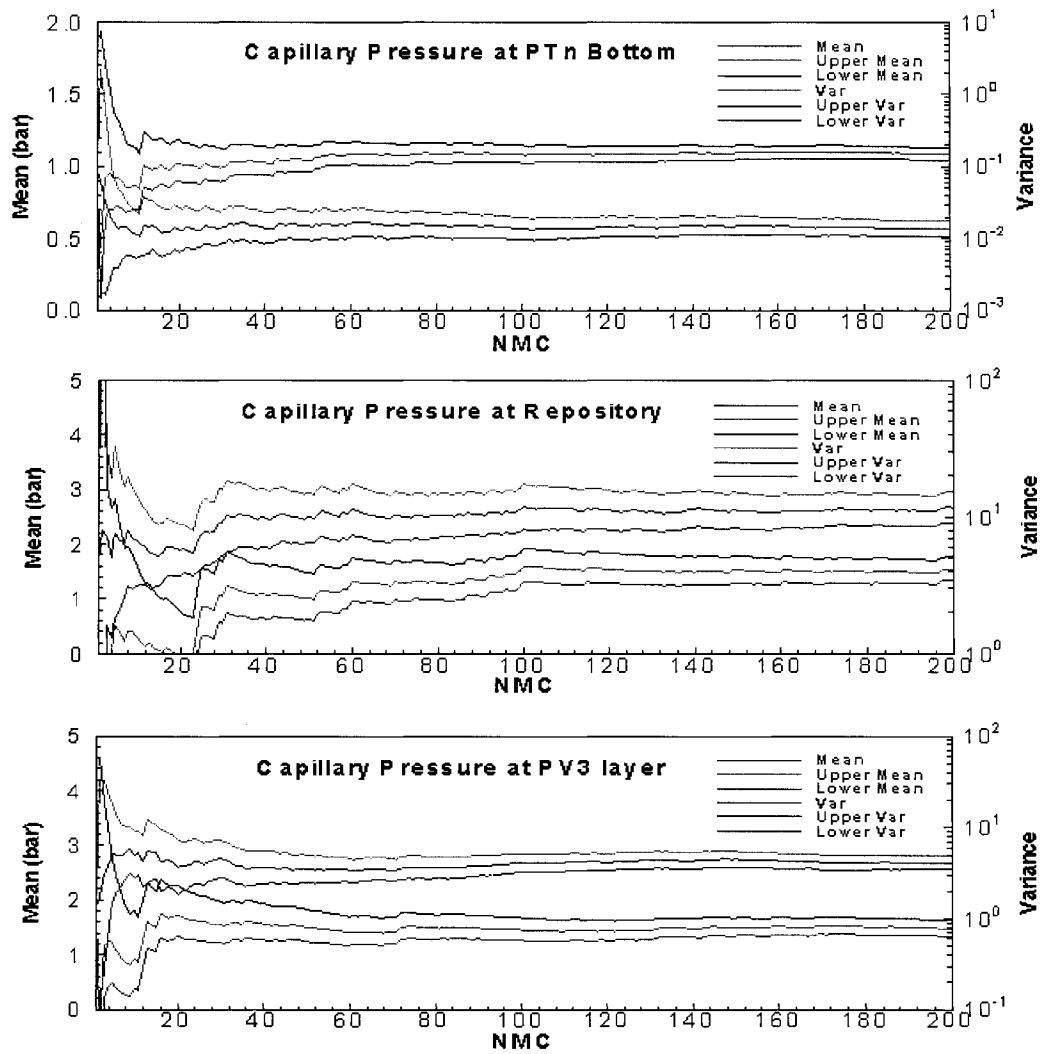


Figure 3.2 Sample mean and variance of simulated capillary pressure with 95% confidence interval at PTn bottom, Repository layer (TLL) and PV3 layer for three-dimensional domain.

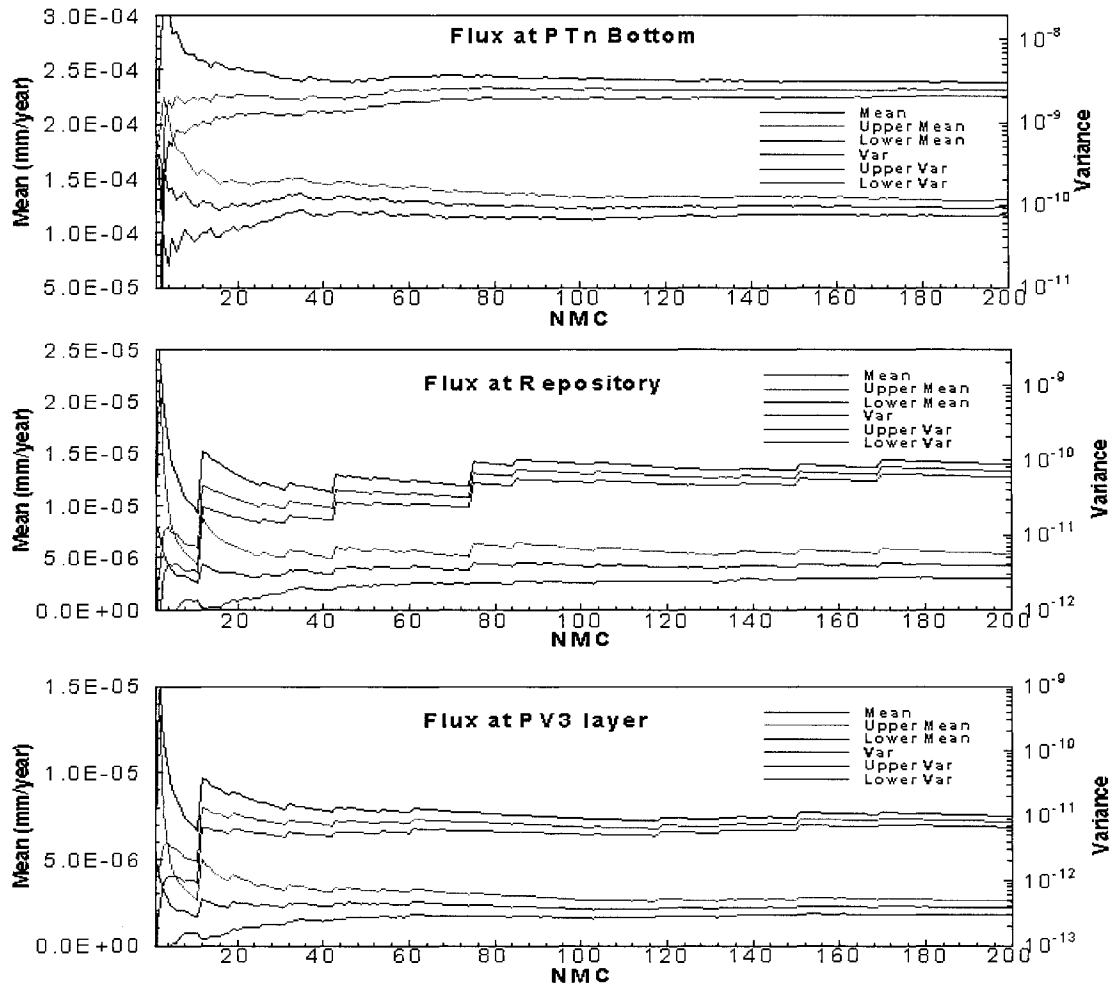


Figure 3.3 Sample mean and variance of simulated matrix vertical flux with 95% confidence interval at PTn bottom, Repository layer (TLL) and PV3 layer for three-dimensional domain.

One can see from Figure 3.3 that the sample means and variances of matrix vertical flux at PTn bottom and PV3 layer stabilize at 200 realizations and the ones at Repository layer have small oscillation. This could be solved by running more simulations. One could also know that the matrix vertical flux decrease from PTn bottom, Repository to PV3 layer because of the decrease of matrix permeability shown in Figure 2.8.

3.3.2 Comparisons of Simulated and Measured Data

In this study, the measured saturation and water potential of boreholes UZ-14, SD-12 and SD-7 (Figure 1.1) are used to examine the model results. The matrix water saturation and water potential data are compared with mean, 5% percentile and 95% percentile of simulated results with 200 realizations. Figures 3.4, 3.5 and 3.6 show the comparisons of mean, 5% percentile, 95% percentile of simulated results and measured data in matrix water saturations along the vertical column of boreholes UZ-14, SD-12 and SD-7. Figure 3.7 shows the comparisons of the simulated and measured matrix water potential for borehole SD-12. In these figures, mean and 50% percentile of our 200 realizations appear close to the simulation results of Wu et al. (2004a), which is used as a base case.

Figures 3.4, 3.5 and 3.6 show that the means of simulated water saturation are in reasonable agreement with the measured water saturation profiles and catch the patterns of the variation of saturation. 5% and 95% percentiles of simulated matrix water saturation bracket the large portion of the measurements. It indicates that the uncertainty bounds from our Monte Carlo simulation represent well the variation of water saturation of the unsaturated system caused by parameter uncertainty. Significant discrepancy between simulated and measured water saturation is observed in the top layer and the interface between TSw and CHn layers. The 5% and 95% percentiles of simulated results at top of the boreholes do not cover the measured data well. This can be attributed to measurement errors, conceptual model error, and ignorance of the randomness of the van Genuchten α and n .

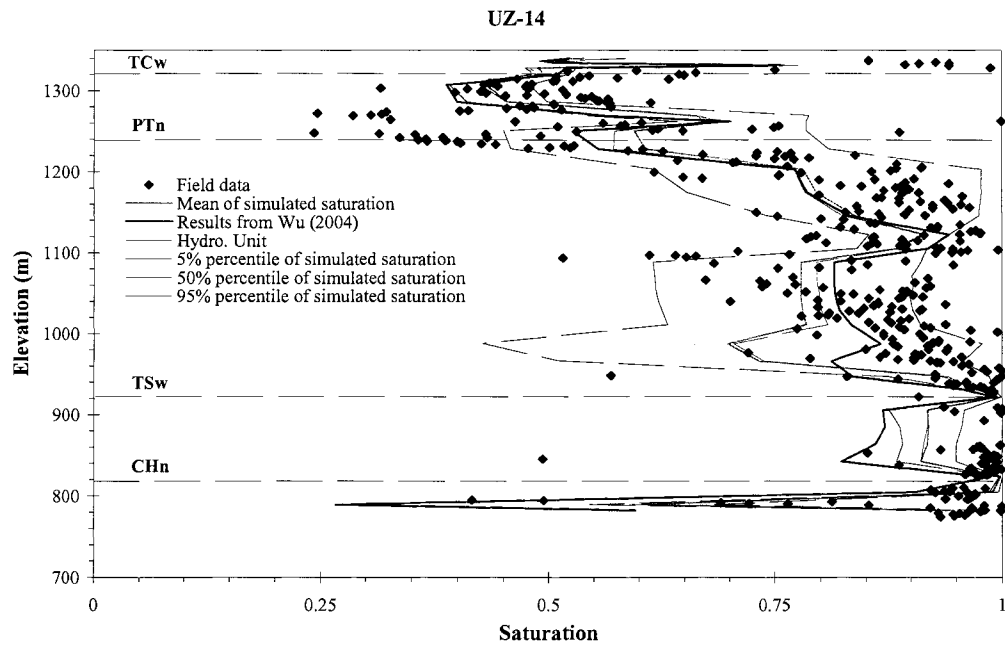


Figure 3.4 Comparison to the simulated and observed matrix saturation for Borehole UZ-14 in three-dimensional domain.

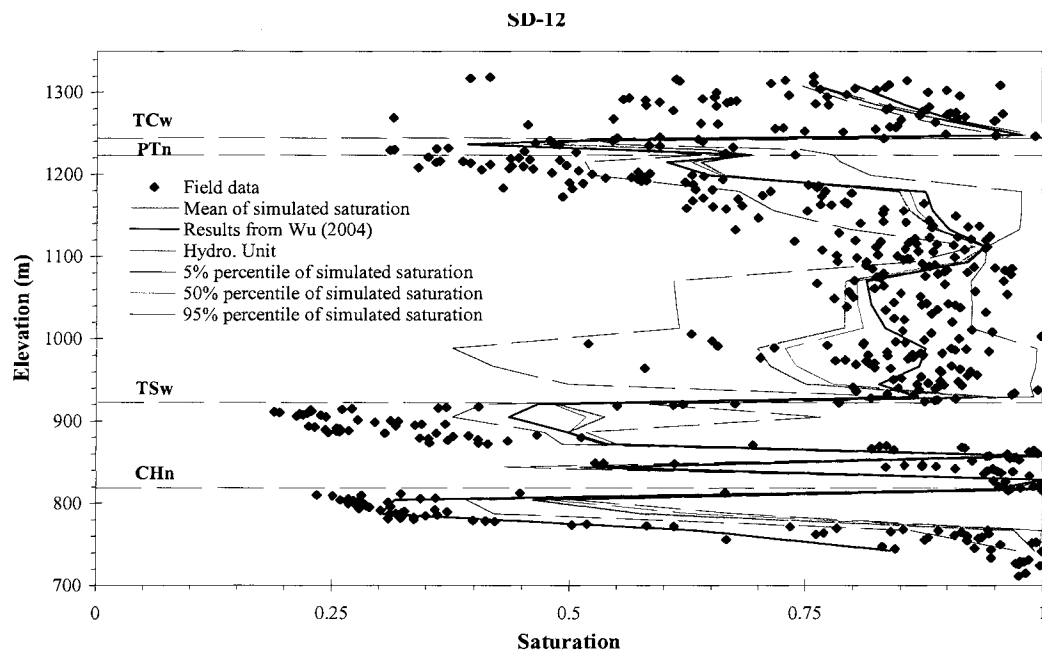


Figure 3.5 Comparison to the simulated and observed matrix saturation for Borehole SD-12 in three-dimensional domain.

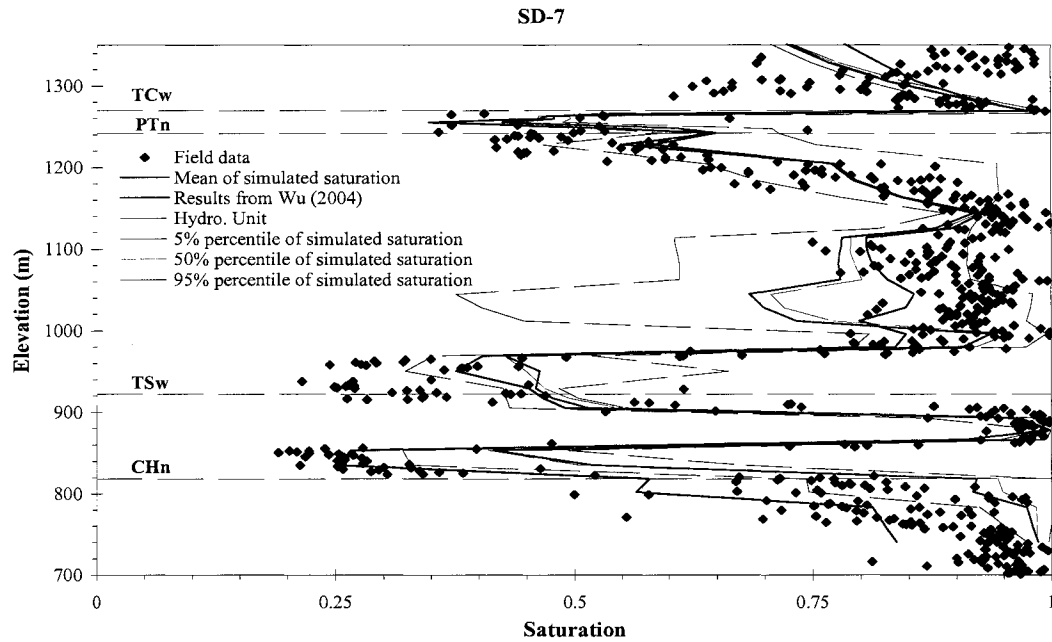


Figure 3.6 Comparison to the simulated and observed matrix saturation for Borehole SD-7 in three-dimension domain.

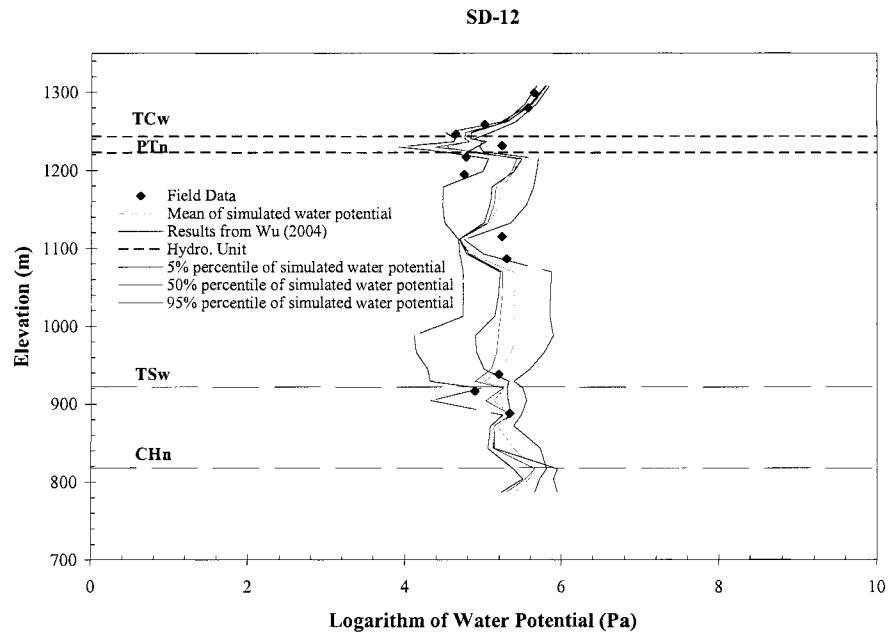


Figure 3.7 Comparison to the simulated and observed Water Potentials for Borehole SD-12 in three-dimension domain.

Figure 3.7 shows similar characteristics as those exhibited in Figures 3.4 - 3.6. The simulated water potential in Borehole SD-12 matches the variation pattern of the measured data and the intervals between 5% and 95% percentiles of simulated results cover most measured values. By comparing Figures 3.5 and 3.7, the values of water potential increase with the decrease of saturation in most depths and do not follow this characteristic in some depths. The reason is that water potential is in inverse proportion to volumetric water content (θ) calculated by saturation (S) and porosity (ϕ) according to the formula $\theta = S * \phi$. In general, the volumetric water content at one layer is larger than the one at another layer when the saturation increases from the layer to another layer, if the porosity has no much change between the two layers. But at some depths, the volumetric water content decreases when saturation increases from one layer to another layer, if the porosity decreases largely. For example, the means of saturation at Repository and PV3 layer shown in Figure 3.1 are about 0.8 and 0.97 but the means of measured porosity shown in Table 2.1 are 0.131 and 0.043, respectively. The volumetric water content at Repository is larger than the one at PV3 layer although the saturation at Repository is smaller than the one at PV3 layer. Therefore, the water potential did not always increase with the decrease of saturation and depended on the volumetric water content.

3.3.3 Uncertainty Analysis of Unsaturated Flow Fields

By the convergence analysis and comparison of measured and simulated data, the simulated unsaturated flow fields are reliable to predict unsaturated flow and to evaluate the uncertainty of flow caused by parameter uncertainty. Because the unsaturated zone acts as a critical natural barrier by delaying the arrival of radionuclide at the saturated

zone, the percolation flux and its spatial variations through the unsaturated zone could affect the amount of water flowing into waste emplacement drifts, radionuclide release from the repository and radionuclide migration from the unsaturated zone to groundwater table (Wu et al., 2004a). Therefore, simulating percolation flux through the unsaturated zone has tremendous significance for the evaluation of the Yucca Mountain as a potential nuclear waste repository site. In this study, the predictions and uncertainties of percolation flux for each layer are calculated and quantified based on the simulated unsaturated flow with 200 realizations. We select three layers, PTn Bottom, Repository layer and Water Table, to present the predictions and uncertainties here.

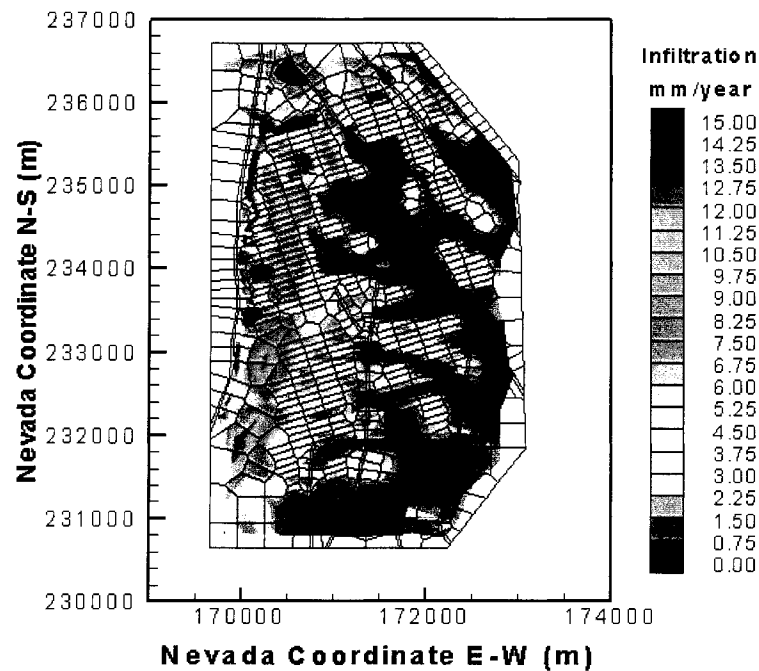


Figure 3.8 Plan view of net infiltration distributed over the 3-D domain.

The source of percolation through the unsaturated zone is net infiltration from precipitation at the land surface at Yucca Mountain. The infiltration pattern is shown in

Figure 3.8 and the average rate of net infiltration over the entire model domain is 3.583 mm/year.

Figures 3.9 - 3.12 depict means, variances, 5% and 95% percentiles of simulated percolation fluxes at PTn bottom. Figures 3.13-3.16 do the same for the Repository layer and Figures 3.17-3.20 for the Water Table. Figures 3.9 and 3.13 show that there is not much difference among the means of simulated percolation fluxes and their spatial distribution patterns at PTn bottom and Repository layer. In addition, the mean of simulated percolation fluxes at the three layers is similar to the surface infiltration pattern shown in Figure 3.8. The only slight difference among them is the flow at southwest part of the model domain. Comparison of Figures 3.9 and 3.13 with 3.17 shows there is similar pattern of spatial distribution of percolation fluxes at the water table as the ones at PTn bottom and Repository layer but the values of fluxes has significant difference between them from west to center of the model domain.

Variances of simulated percolation fluxes with 200 realizations shown in Figures 3.10, 3.14 and 3.18 quantify predictive uncertainty of the fluxes caused by parameter uncertainty in matrix permeability and porosity. From these figures, one can observe that the variances of simulated percolation fluxes and their patterns at PTn bottom and Repository layer are very similar and the ones at Water Table have significant difference from the ones at PTn bottom and Repository layer. The variances of simulated flux at the water table are much larger than the ones at PTn bottom and Repository layer. It indicates that the fluxes at Water Table are more uncertain than the ones at PTn bottom and Repository layer due to the deterministic bottom boundary condition. It can also be

observed from 5% and 95% percentiles of simulated fluxes at three layers shown in Figures 3.11, 3.12, 3.15, 3.16, 3.19 and 3.20.

Figures 3.9 to 3.16 show that the means, 5% and 95% percentiles of simulated fluxes are the same or very similar at PTn bottom and Repository layer because of the small variances shown in Figures 3.10 and 3.14. Figures 3.17 to 3.20 show that the means, 5% and 95% percentiles of simulated fluxes and their patterns are totally different, which demonstrates the significance of our uncertainty analysis. The major differences are the fluxes from center to west boundary of the model domain. Due to the variance shown in Figure 3.18, the 5% percentile of flux at the region is much smaller and the 95% percentile of flux at the region is much larger than the means of fluxes. The mean of fluxes from center to east boundary of the model domain has no big difference from the 5% and 95% percentiles of fluxes. In the future site characterization, more effort should be spent at the west part of the domain.

From the above analysis, it can be concluded that the uncertainties of simulated percolation fluxes exist in the unsaturated zone and could be quantified by the means, variances, 5% and 95% percentiles of simulated fluxes. Parametric uncertainty in matrix permeability and porosity has significant influences on simulated fluxes at the water table and can lead to the large uncertainties of flow at the water table. Parametric uncertainty, however, has negligible effects on simulated fluxes at PTn bottom and Repository layer, which can be attributed to the fracture and fault dominated flow at PTn bottom and Repository layer, while the ones at the water table are around 50% from matrix flow which is obtained from the mean of simulated percolation fluxes in matrix and fracture and the generated random fields in matrix permeability and porosity only represent

parameter uncertainty in Matrix. Therefore, the uncertainties of groundwater flow at the water table are much larger than the ones at PTn bottom and Repository layer caused by parameter uncertainty in matrix permeability and porosity.

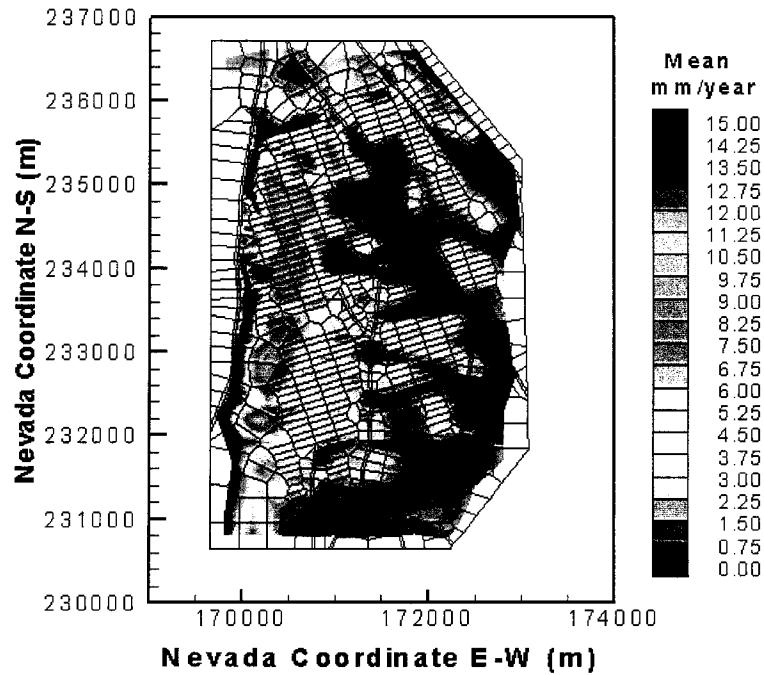


Figure 3.9 Mean of simulated percolation fluxes at PTn Bottom for the 3-D domain.

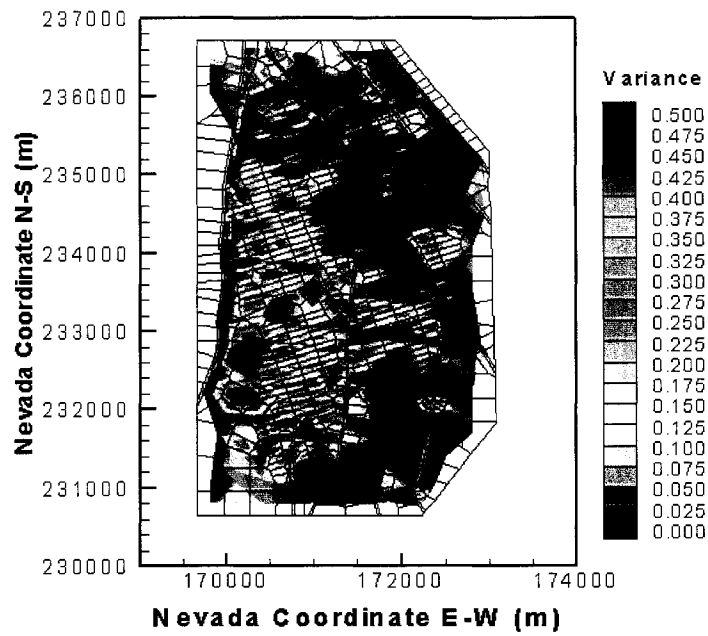


Figure 3.10 Variance of simulated percolation fluxes at PTn Bottom for the 3-D domain.

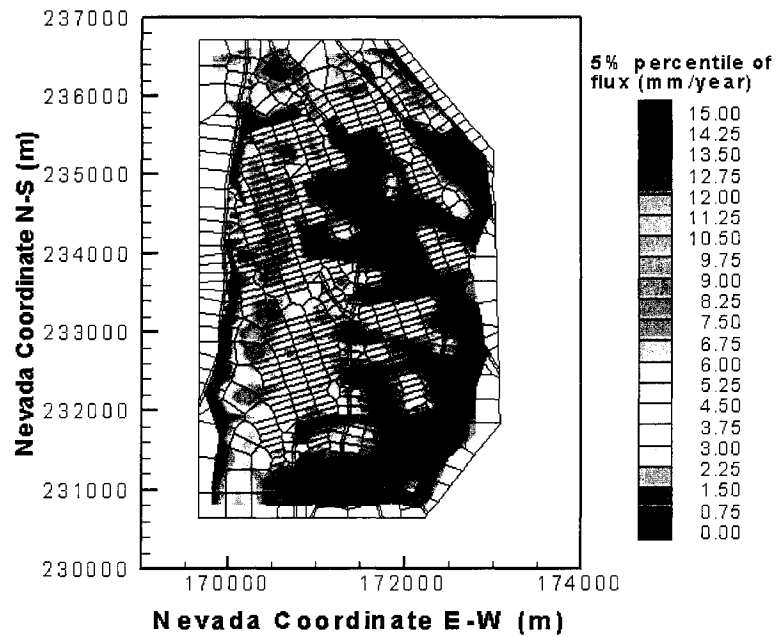


Figure 3.11 5% percentile of simulated percolation fluxes at PTn Bottom for the 3-D domain.

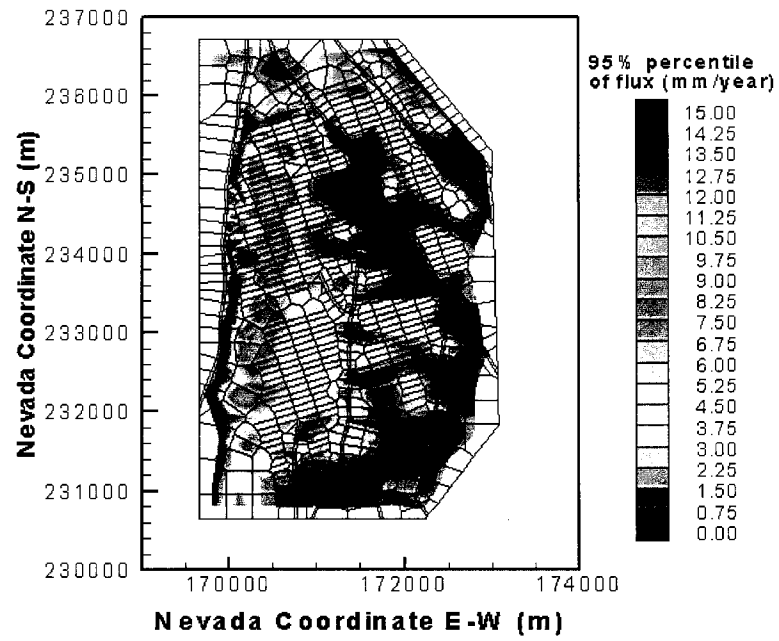


Figure 3.12 95% percentile of simulated percolation fluxes at PTn Bottom for the 3-D domain.

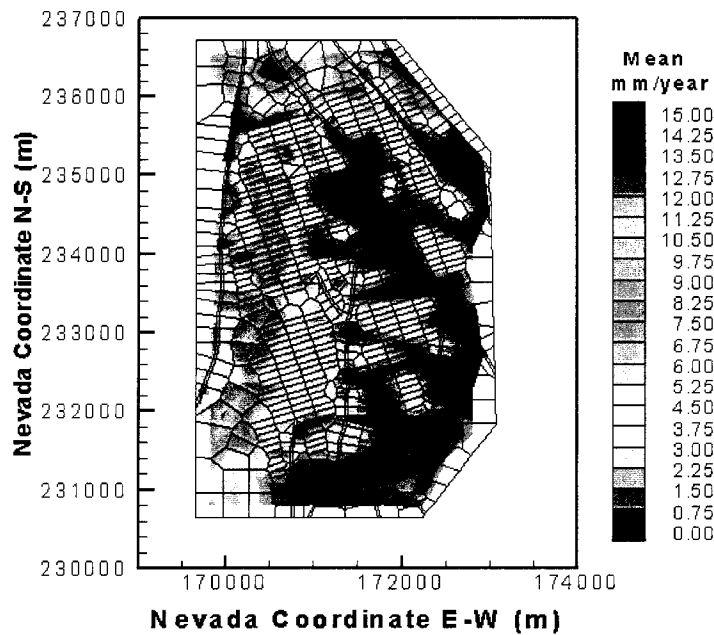


Figure 3.13 Mean of simulated percolation fluxes at Repository level for the 3-D domain.

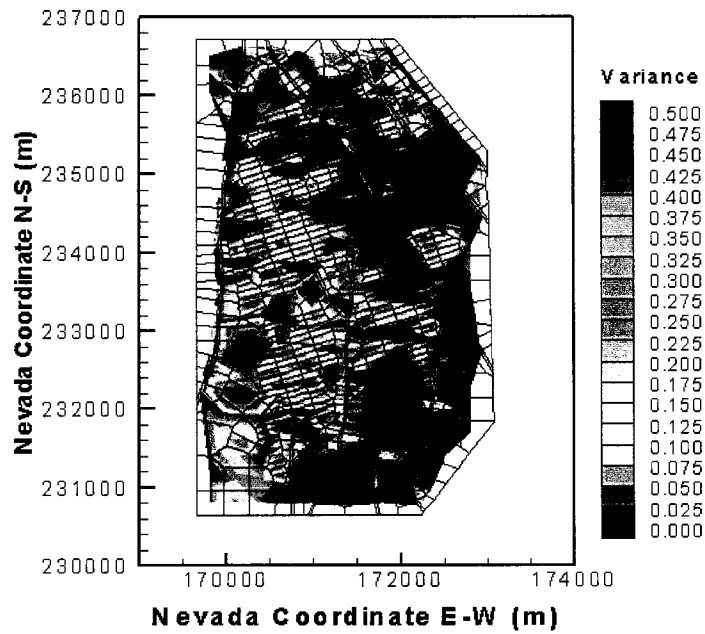


Figure 3.14 Variance of simulated percolation fluxes at Repository level for 3-D domain.

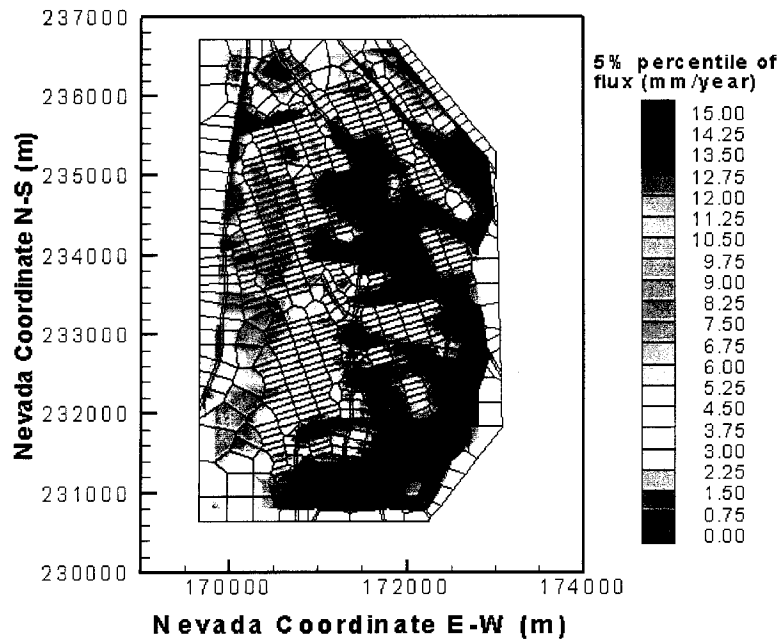


Figure 3.15 5% percentile of simulated percolation fluxes at Repository level for the 3-D domain.

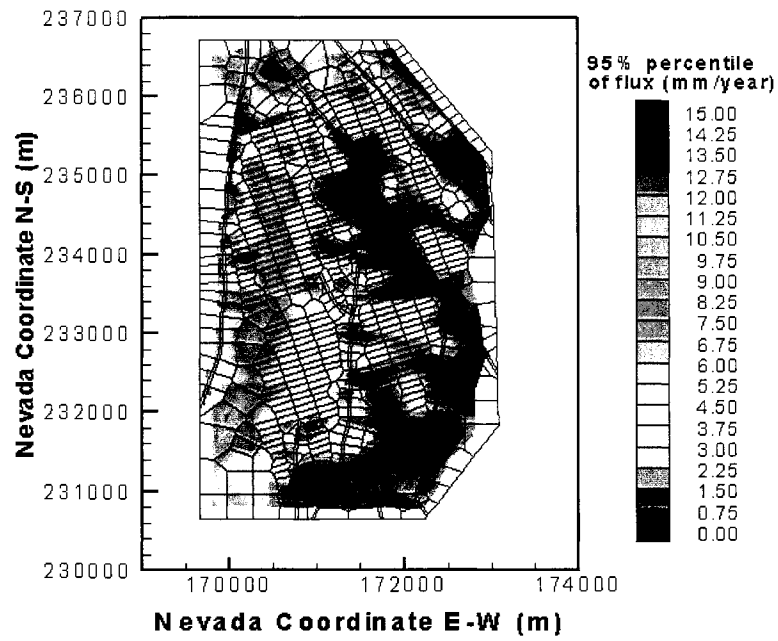


Figure 3.16 95% percentile of simulated percolation fluxes at Repository level for the 3-D domain.

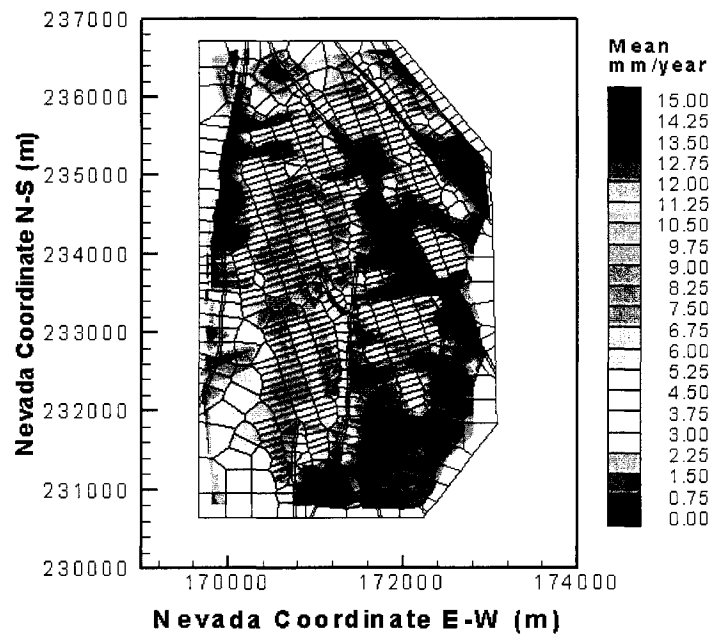


Figure 3.17 Mean of simulated percolation fluxes at water table for the 3-D domain.

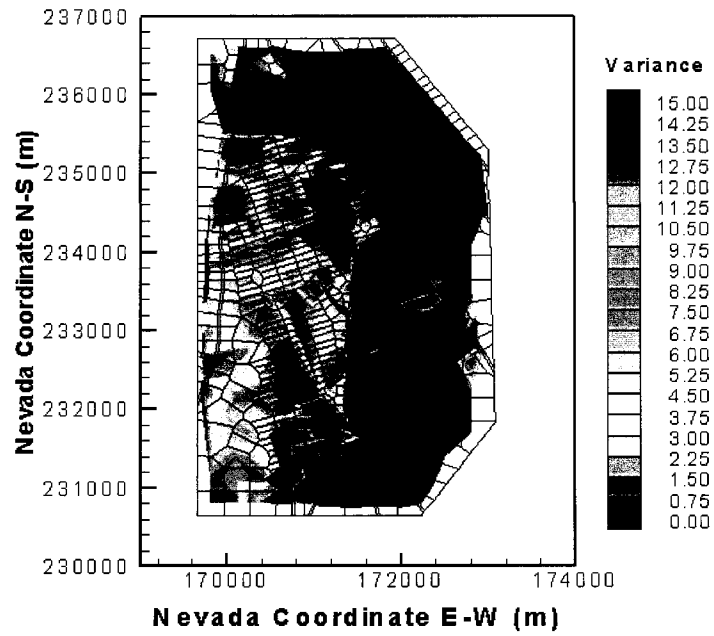


Figure 3.18 Variance of simulated percolation fluxes at water table for the 3-D domain.

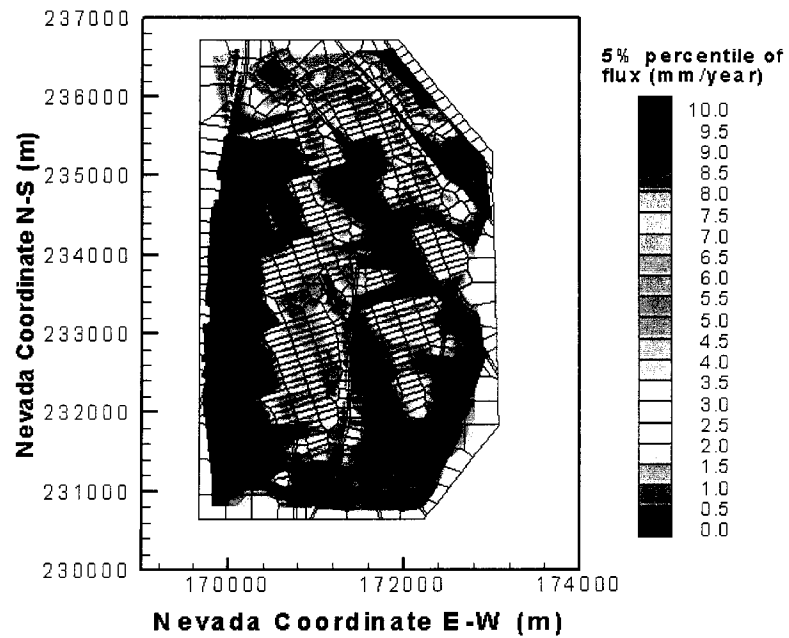


Figure 3.19 5% percentile of simulated percolation fluxes at water table for the 3-D domain.

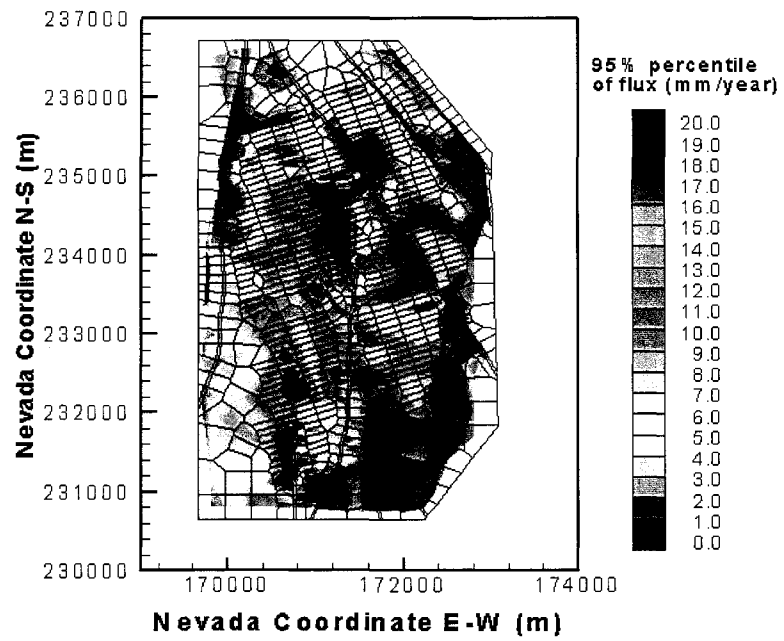


Figure 3.20 95% percentile of simulated percolation fluxes at water table for the 3-D domain.

CHAPTER 4

UNCERTAINTY ANALYSIS OF RADIONUCLIDE TRANSPORT IN THE UNSATURATED ZONE

4.1 Introduction

Modeling radionuclide transport in the unsaturated zone is one of the most important issues in the Yucca Mountain Project because the potential high-level nuclear waste repository would be located in the unsaturated zone at Yucca Mountain. It is necessary to predict the radionuclide travel time from repository to water table and to evaluate the associated predictive uncertainty due to parameter uncertainty in sorption coefficient, permeability, and porosity.

In this study, Monte Carlo approach is used to quantify radionuclide transport uncertainty and the T2R3D module of TOUGH2 code is used to simulate the transport of the conservative tracer (technetium, ^{99}Tc) and reactive tracer (neptunium, ^{237}Np), respectively, in the unsaturated zone at Yucca Mountain. The steady-state flow fields obtained in Chapter 3 are used by T2R3D to simulate the transport problem. For the conservative tracer Tc, we evaluate the effects of parametric uncertainty of matrix permeability and porosity on the transport simulation. For the reactive tracer Np, 200 realizations of the random sorption coefficient for Np are generated using the Latin Hypercube Sampling (LHS) method in Chapter 2 and are used as the input data to

T2R3D module for the reactive tracer. Therefore, the effects of parametric uncertainty of sorption coefficient, matrix permeability and porosity on radionuclide transport are evaluated for Np. The method by Ballio and Guadagnini (2004) is also employed to examine the convergence of Monte Carlo simulation. The means, variances, and 5% and 95% percentiles of simulated travel time and fractional mass of radionuclide transport over all realizations are estimated based on the simulated 200 transport realizations. Therefore, the prediction of travel time and fractional mass of radionuclide transport can be obtained and the uncertainty of radionuclide transport from the parameter uncertainty can also be quantified.

4.2 Simulation Procedure and Transport Parameters

In this study, the steady-state flow fields of 200 realizations with uncertainty from matrix porosity and permeability are used as the input data of T2R3D module. The random fields of sorption coefficient for the reactive tracer with 200 realizations are also inputted to the transport simulations. In this study, only matrix porosity and permeability are treated random for the conservative tracer simulations, whereas the sorption coefficient, matrix porosity and permeability are generated randomly for the reactive tracer. In this simulation, the convergence tolerance is set as 0.01 and the simulation time is 10^6 years. By running T2R3D module with the input data under steady-state flow fields with constant released tracers at the repository fracture blocks for each realization, the radionuclide transport in unsaturated zone is simulated. Then, the uncertainty of travel time and fractional mass of the tracers released from repository can be evaluated by analyzing output of the overall realizations.

In transport simulations, the sorption coefficient of the reactive tracer (^{237}Np) is treated random and the parametric uncertainty is incorporated by generating the random fields in Chapter 2 for the three types of rocks Devitrified, Vitric and Zeolitic tuffs. Sorption coefficient is set as zero for the conservative tracer (^{99}Tc). The molecular diffusion coefficient is set as $3.2 \times 10^{-10} \text{ m}^2/\text{s}$ for the conservation tracer and $1.6 \times 10^{-10} \text{ m}^2/\text{s}$ for the reactive tracer in each layer. The effective diffusion coefficient is random because it is obtained by multiplying deterministic dispersivity and tortuosity with random porosity for each layer. The mechanical dispersion through fracture-matrix system is set as zero because it has no significant effect on the breakthrough curves of the tracers at water table by sensitivity studies (Wu et al., 2004a).

4.3 Results Analysis

200 realizations of cumulative fractional mass breakthrough and tracer travel time are simulated and transport uncertainty is evaluated based on the 200 realizations. In this study, the definition of cumulative fractional mass breakthrough is the cumulative mass of a tracer arriving at the water table over the entire bottom model boundary over time normalized by the total mass of the tracers released from the repository. The tracer travel time is the cumulative time of the tracers from repository to water table and is calculated from the cumulative fractional breakthrough curve.

4.3.1 Convergence Analysis of Monte Carlo Simulation

The method of Ballio and Guadagnini (2004) is used to examine convergence of the Monte Carlo simulation. The cumulative fractional mass of the tracers arriving at water table and the travel time from repository to water table are selected to check the

convergence of Monte Carlo simulation. Figures 4.1 and 4.2 show the sample means and variances with 95% confidence intervals of cumulative fractional mass at water table for ^{99}Tc and ^{237}Np released from repository after 0.1, 1.0, 10, 100, 1,000, 10,000, 100,000 and 1,000,000 years. Figure 4.1 shows that the mean and variance stabilize after 200 realizations, indicating that 200 realizations are sufficient.

Figure 4.1 shows that the sample means of cumulative fractional mass increase from 0.2 to 0.99 with the increase of the travel time from 10 years to 1 million years, indicating the amount of radionuclide transported to water table increase with time. In other words, after the radionuclide releases from repository at 1 million years, almost 100 percent released tracers have arrived at water table and move into groundwater. The variances of cumulative fractional mass increase from the beginning of the tracer traveled, reach the largest values around 100 and 1,000 years, and then decrease after 1,000 years. It can also be observed in Figure 4.5 as discussed below. It indicates that the parameter uncertainty has more significant effects on the simulated cumulative fractional mass breakthrough at the middle of tracer travel than one at the beginning and the end of the tracer transport. The reason is that the mass of radionuclide arriving at water table is very small at the beginning of the tracer travel and more than 90% of radionuclide has arrived at water table after 100,000 years regardless the radionuclide traveling rate. And uncertainty of flow fields can cause a large range of the cumulative fractional mass breakthrough at water table at the middle of tracer travel.

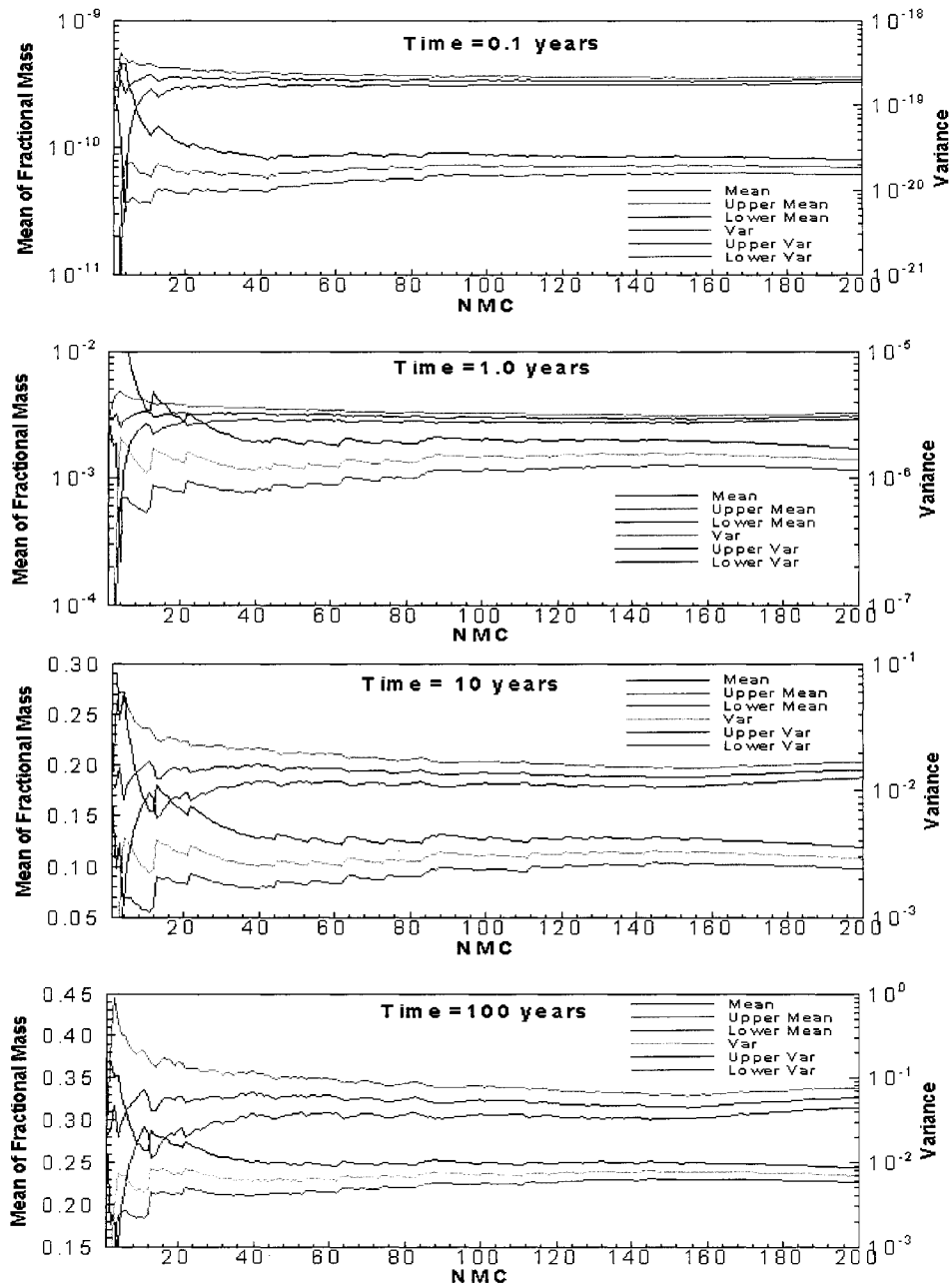


Figure 4.1 Sample mean and variance of simulated cumulative fractional mass of a conservative tracer (T_c) arriving at water table after 0.1, 1.0, 10 and 100 years with 95% confidence interval for the three-dimensional domain.

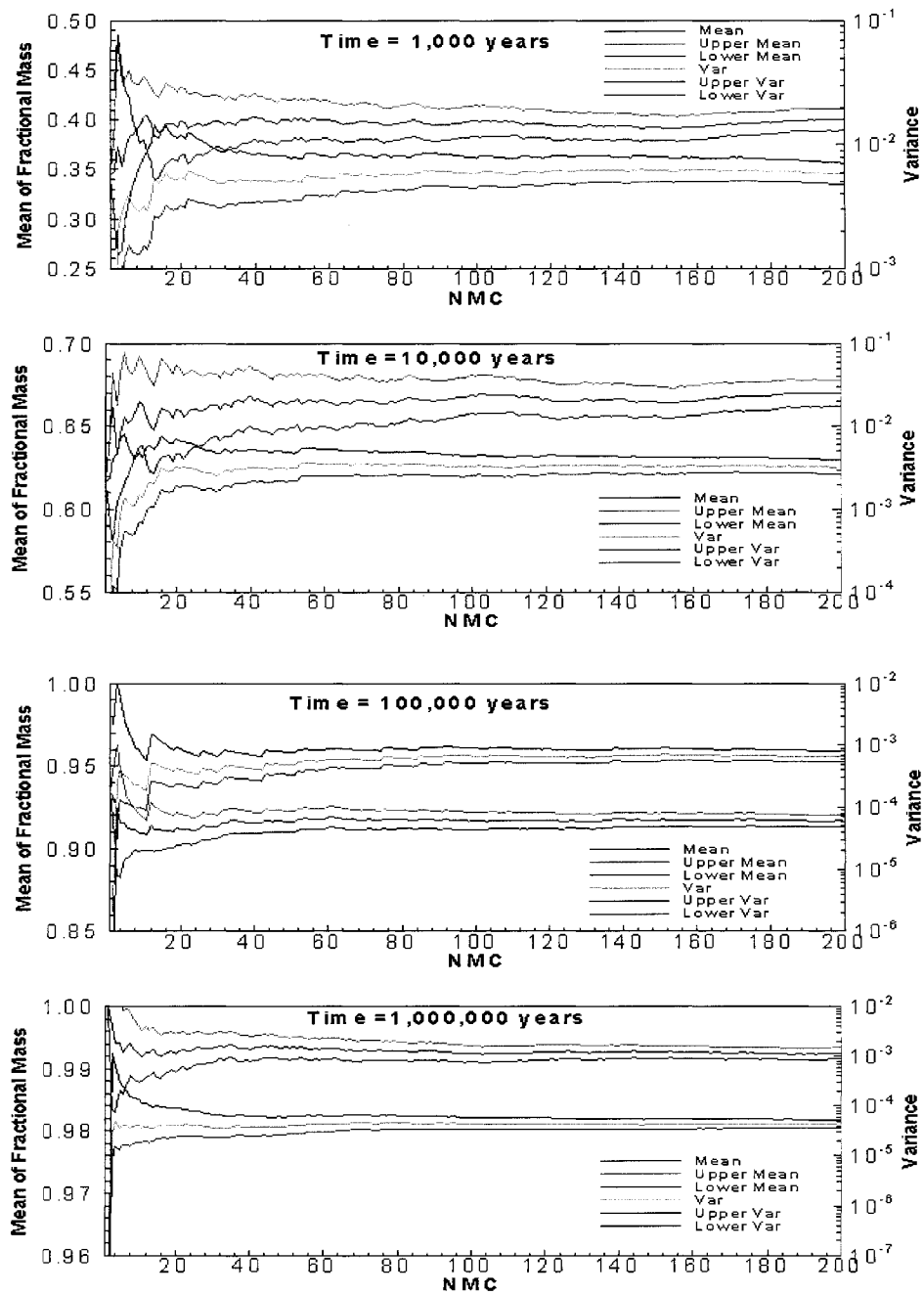


Figure 4.1 (Cont.) Sample mean and variance of simulated cumulative fractional mass of a conservative tracer (T_c) arriving at water table after 1,000, 10,000, 100,000 and 1,000,000 years with 95% confidence interval for the three-dimensional domain.

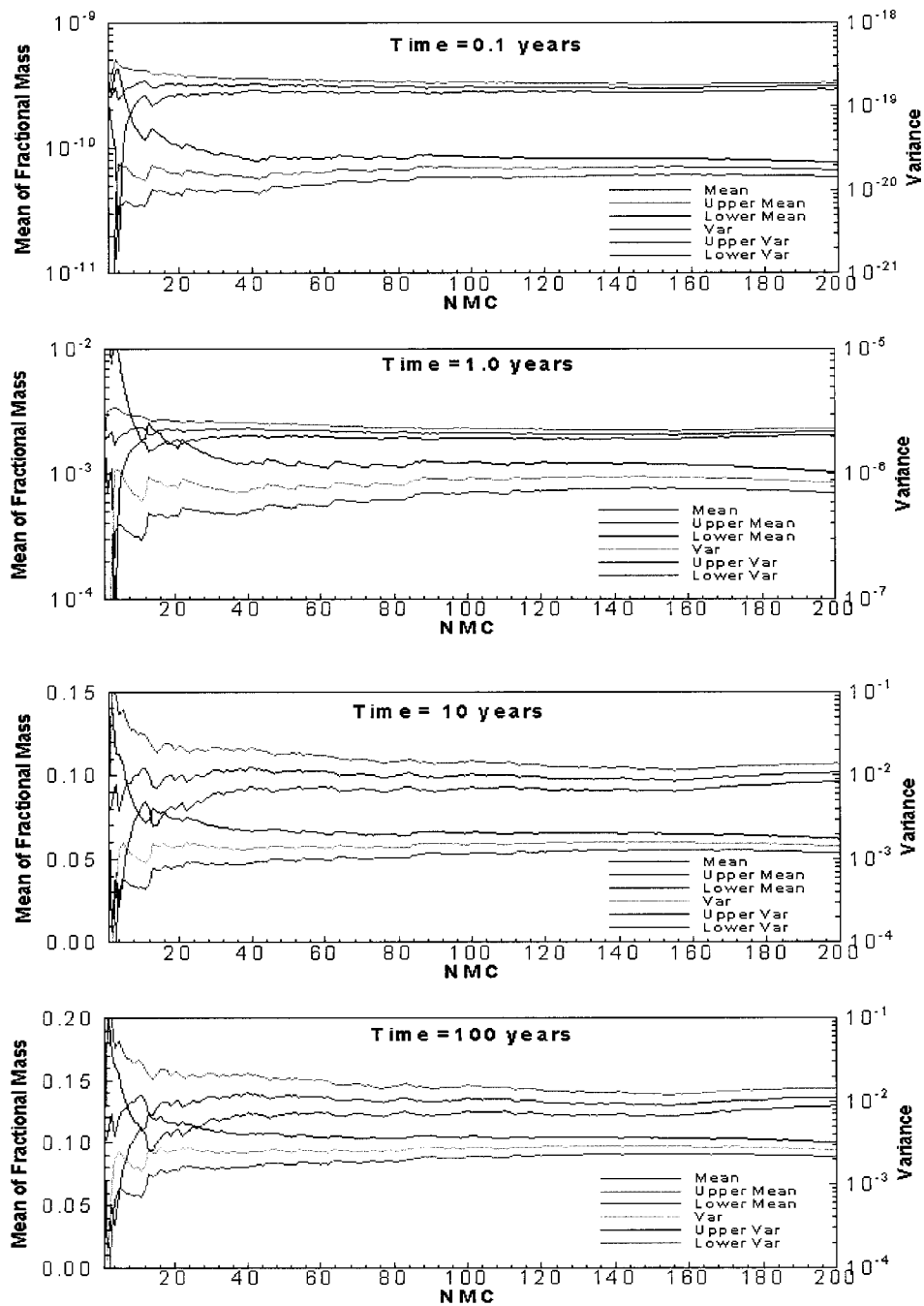


Figure 4.2 Sample mean and variance of simulated cumulative fractional mass of a reactive tracer (Np) arriving at water table after 0.1, 1.0, 10 and 100 years with 95% confidence interval for the three-dimensional domain.

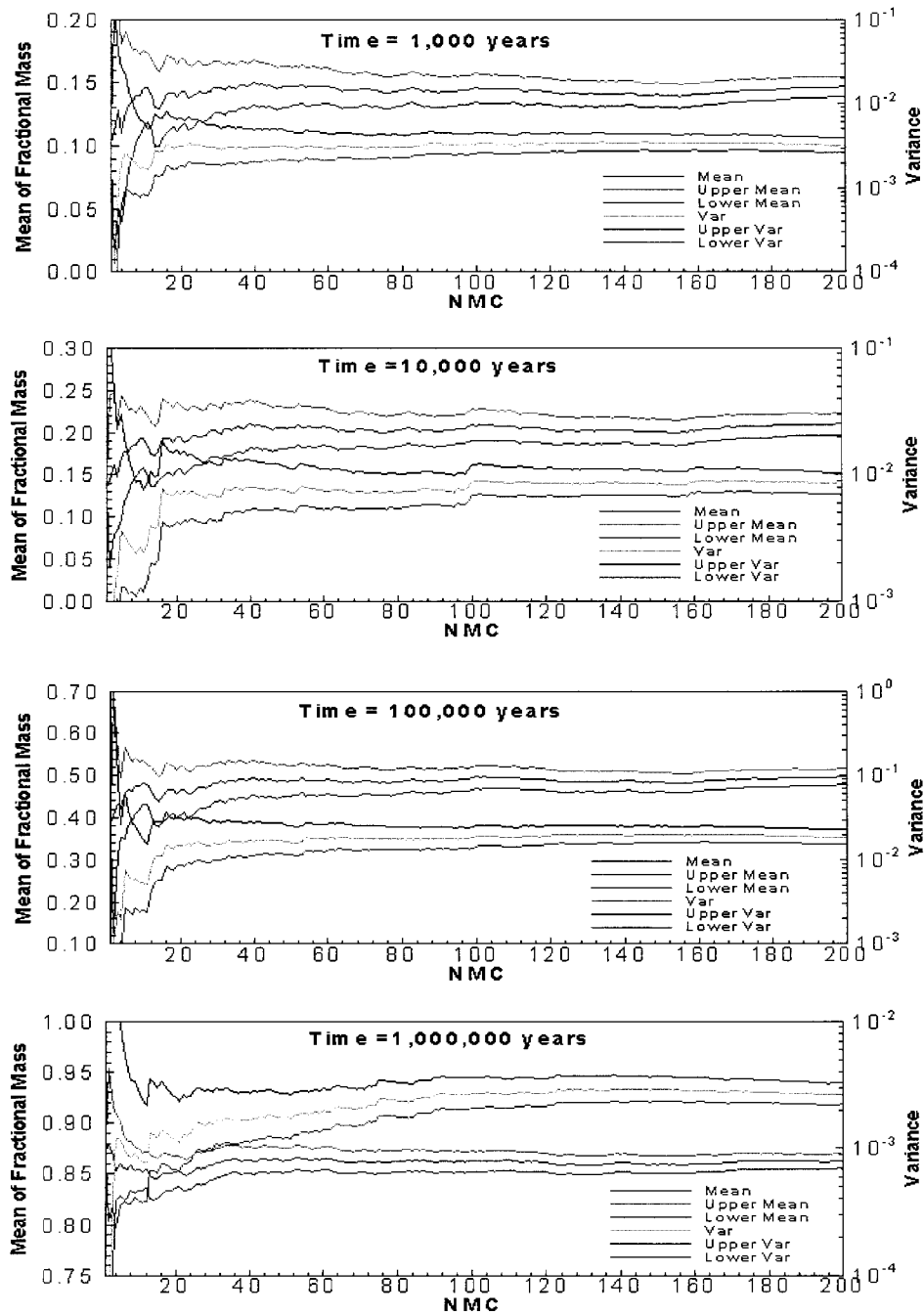


Figure 4.2 (Cont.) Sample mean and variance of simulated cumulative fractional mass of a reactive tracer (Np) arriving at water table after 1,000, 10,000, 100,000 and 1,000,000 years with 95% confidence interval for the three-dimensional domain.

The convergence patterns of mean and variance for the reactive tracer Np shown in Figure 4.2 are similar to those shown in Figure 4.1. The comparison of Figures 4.1 and 4.2 shows that the cumulative fractional mass of ^{237}Np is smaller and increase slower than ones of ^{99}Tc . One can know from the figures that the cumulative fractional mass of ^{99}Tc reaches 0.4 and 0.66 after 1,000 and 10,000 years but the one of ^{237}Np is only 0.14 and 0.20 at the same travel time. The reason is that the sorption of the reactive tracer leads to less mass arriving at water table than the conservative tracer at the same transport time.

Figure 4.3 shows the sample means and variances with 95% confidence intervals of travel time from repository to water table for ^{99}Tc at 50%, 75% and 90% cumulative fractional breakthrough. One can see from Figure 4.3, the 95% confidence intervals decrease with the increase of realizations and stabilize after 150 realizations. The sample means and variances of the travel time reach the convergence at 200 realizations.

Figure 4.4 shows the convergence analysis of the travel time for ^{237}Np at 25%, 50% and 75% cumulative fractional breakthrough. From Figure 4.4, one can observe that the sample means and variances of the travel time with 95% confidence intervals have similar properties and trends as those for ^{99}Tc . Although small jumps of the means and variances with 95% confidence intervals happen at 60 and 120 realizations for 25% and 50% cumulative fractional breakthrough, the means and variances stabilize after 150 realizations. By the above examinations, it can be concluded that the sample means and variances of cumulative fractional mass and travel time have reached the convergence at 200 realizations.

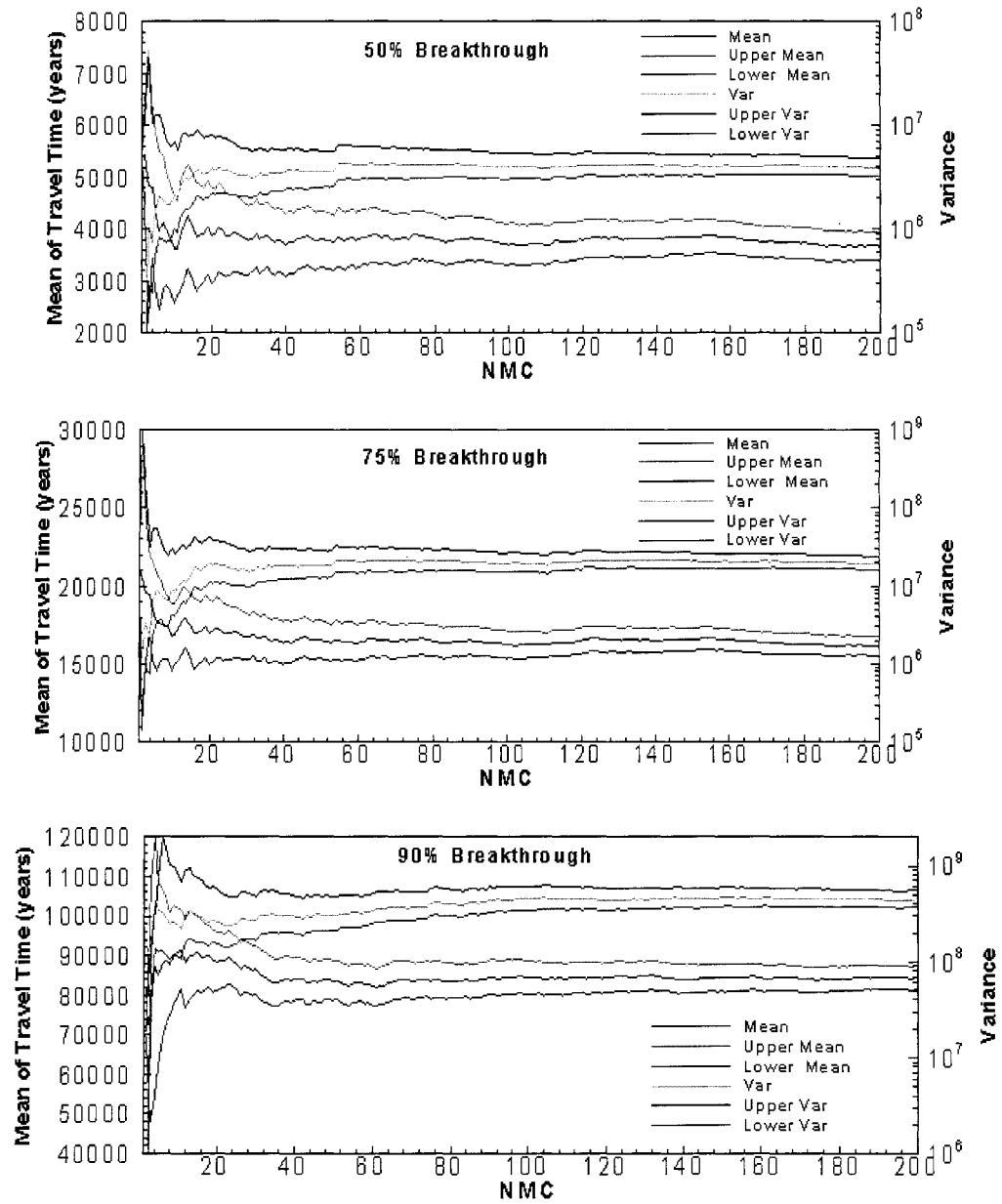


Figure 4.3 Sample mean and variance of simulated travel time of a conservative tracer (T_c) arriving at water table at 50%, 75% and 95% breakthrough with 95% confidence interval for the three-dimensional domain.

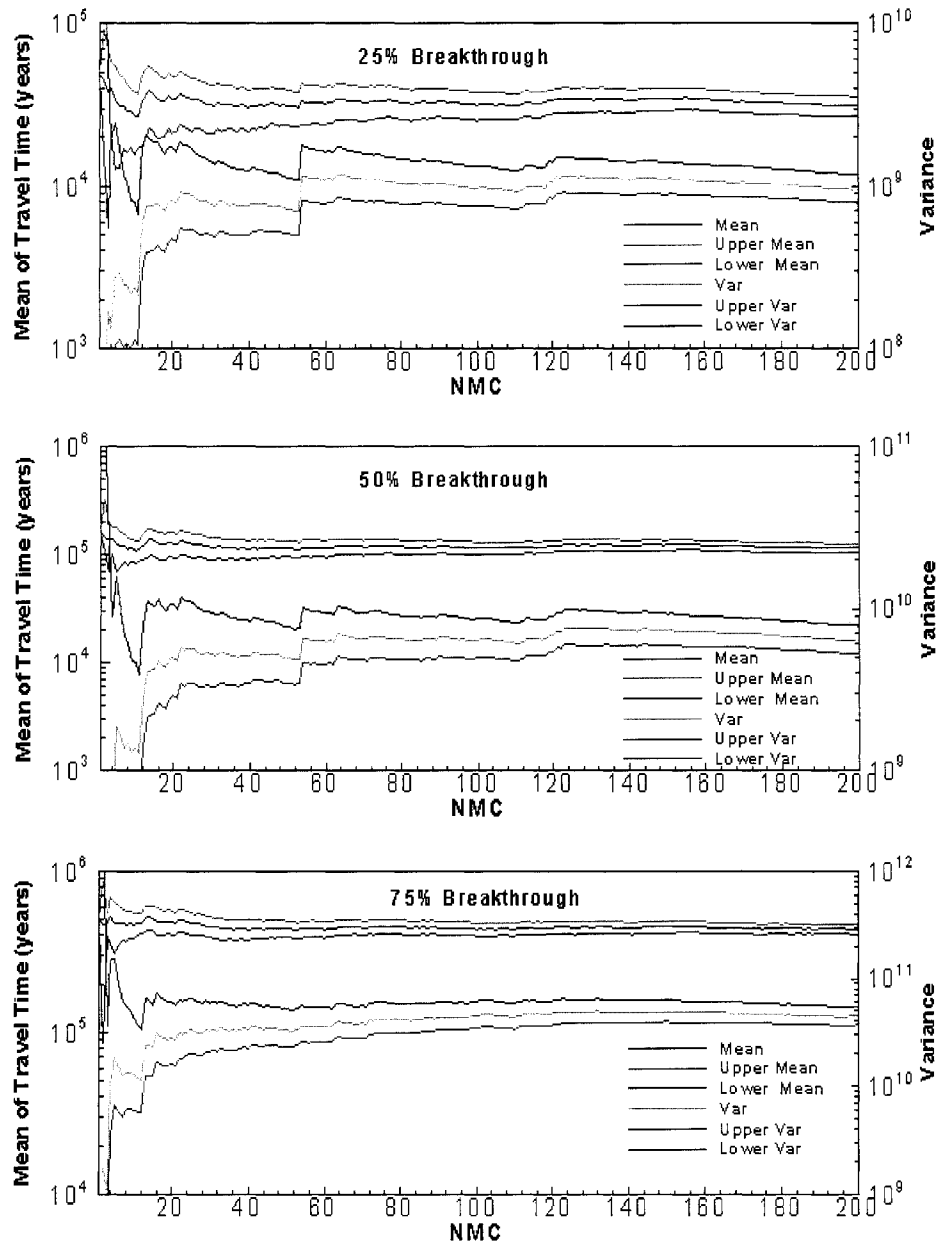


Figure 4.4 Sample mean and variance of simulated travel time of a reactive tracer (N_p) arriving at water table at 25%, 50% and 75% breakthrough with 95% confidence interval for the three-dimensional domain.

4.3.2 Uncertainty Analysis of Transport Simulation

The tracer travel time from repository to water table is analyzed using the breakthrough curve, which is obtained by calculating the cumulative fractional mass arriving at water table at each time step. The means, 5%, 50% and 95% percentiles of cumulative fractional breakthrough are used to evaluate the uncertainty of radionuclide. In addition, the cumulative mass arrival at each cell of water table can also be calculated to estimate the potential locations with high concentration of radionuclides at water table. The cumulative mass arrival is the cumulative mass arriving at each cell of water table over time, normalized by the total released radionuclide from repository (Wu et al., 2004a). The uncertainties of the cumulative mass are also evaluated by 5% and 95% percentiles at 1,000 and 1,000,000 years for ^{99}Tc and ^{237}Np .

The cumulative fractional breakthrough curves are shown in Figures 4.5 and 4.6 for the conservative tracer Tc and the reactive tracer Np, respectively. In Figure 4.5, the mean and 50% percentile of simulated fractional mass breakthrough of ^{99}Tc are almost the same as the base case of Wu et al. (2004a). Figure 4.5 shows that there are significant uncertainties in fractional mass breakthrough of ^{99}Tc released from repository after 10 years by comparing their means, 5%, 50% and 95% percentiles. Although the mean (and 50% percentile) shows that all of radionuclide arrive at water table at 1,000,000 year, the 95% percentile of the breakthrough curve shows that this may occur at 100,000 years and the 5% percentile line shows that 98% of the mass would flow out to groundwater at 1,000,000 year. The tracer transport time from repository to water table also varies largely by analyzing the breakthrough curve. The travel time varies from 1,000 to 10,000 years between 5% and 95% percentiles at 50% breakthrough and is from 6,000 to 20,000

years at 75% breakthrough. These uncertainties are caused by the uncertainties of flow fields and random porosity. It indicates that the uncertainty in hydraulic flow parameters has significant influences on the cumulative fractional mass arriving at water table and the travel time of the radionuclide from repository to water table.

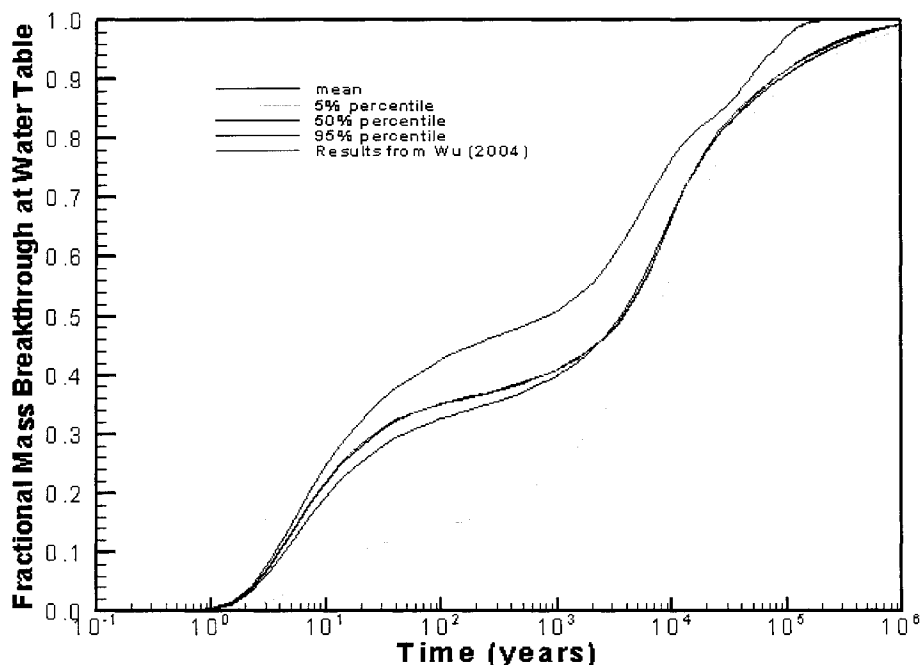


Figure 4.5 Simulated breakthrough curves of cumulative mass of a conservative tracer (Tc) arriving at water table for the three-dimensional domain.

Figure 4.6 shows that the transport simulation of ^{237}Np is more uncertain than that of ^{99}Tc . Not all of radionuclide has arrived at water table at 1,000,000 years and cumulative fractional mass at 1,000,000 years are only 0.78, 0.86 and 0.94 for 5%, 50% (the same for mean) and 95% percentiles, respectively. The 5% and 95% percentile lines show that the cumulative fractional breakthrough ranges from 0.06 to 0.4 at 10,000 years and from 0.22 to 0.68 at 100,000 years. And the tracer transport time from repository to

water table varies from 3,000 to 100,000 years between 5% and 95% percentiles at 25% breakthrough and is from 25,000 to 350,000 years at 50% breakthrough. These illustrate that the parameter uncertainty in sorption coefficient of ^{237}Np and porosity and the uncertainties from flow fields could cause significant uncertainties of radionuclide transport. One can also know that the mean and 50% percentile of cumulative fractional breakthrough are much larger after 5,000 years than the base case of Wu et al. (2004a). The main reason is the different values of sorption coefficient used in our simulations and the base case of Wu et al. (2004a). In Wu's case, the sorption coefficients are 4.0 mL/g for Zeolitic tuff and 1.0 mL/g for Vitric and Devitrified tuffs. In our simulations, the sorption coefficient (K_d) is generated randomly based on measured data. The 50% percentile of generated K_d shown in Table 2.9 are 2.041, 0.481 and 0.345 mL/g for Zeolitic, Vitric and Devitrified tuffs, respectively. Therefore, the smaller sorption coefficient used in our simulations makes the radionuclide travel much further than ones in Wu's case after 5,000 years. Nevertheless, the breakthrough curve of Wu et al (2004a) is within the 5% and 95% percentiles of the simulated breakthrough curves.

By comparing Figure 4.5 with 4.6, one can find that the transport of the conservative tracer travels one or two orders of magnitude faster than the reactive tracer. The mean of the travel times are 3,500 year and 100,000 years for ^{99}Tc and ^{237}Np at 50% breakthrough respectively. When the tracers transport 1,000 years, the mean of cumulative fractional mass arriving at water table are 0.38 for ^{99}Tc and only 0.14 for ^{237}Np , due to the sorption. Therefore, it indicates that sorption coefficient has significant effects on radionuclide transport.

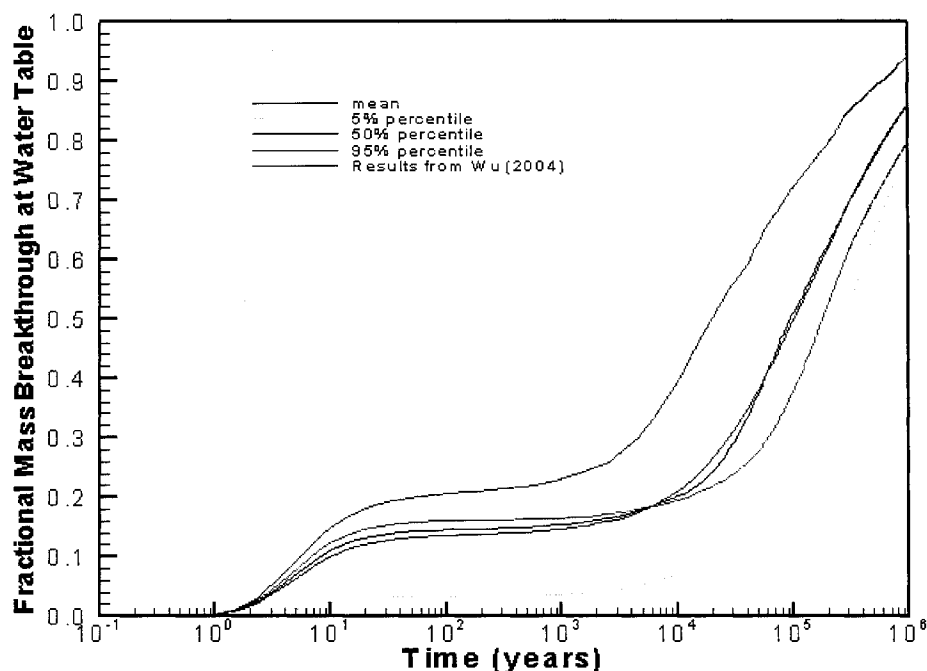


Figure 4.6 Simulated breakthrough curves of cumulative mass of a reactive tracer (Np) arriving at water table for the three-dimensional domain.

Figures 4.7 to 4.10 show that the mean, variance, 5% and 95% percentiles of cumulative normalized mass arrive at the water table at 1,000 years for the conservative tracer. The uncertainties of radionuclide transport could also be evaluated by these figures. One can see that the mean of cumulative normalized mass arrival contour for ^{99}Tc at 1,000 years covers a large area below the repository footprint shown in Figure 1.1 and about 38% (Mean) of the total released radionuclide has arrived at water table (Figure 4.5). One can also see from Figure 4.7 that the large means of mass arrival are close to several faults in north of the model domain. From Figure 4.8, one can know that the pattern of variances is similar as that of the mean shown in Figure 4.7. The largest variance appears in north boundary of repository footprint with the corresponding largest mean of mass fraction along several faults. The variances decrease from north to south of

the model domain with corresponding decrease of the means. Because the repository is in north and west of the model domain (Figure 1.1) and only part of radionuclide has arrived at the water table at 1,000 years, the large mean of mass fraction at a grid cell can cause large variance at the grid. That is, the large variance appears in the north of model domain with large mean and no variance is in south-east of the model domain because no radionuclide releases from the locations at repository. The uncertainty and variance shown in Figure 4.8 can also be responded in 5% and 95% percentiles of mass arrival contours shown in Figures 4.9 and 4.10. The 5% percentile of mass arrival contour at 1,000 years covers much smaller area than the mean; while 95% percentile contour has a little larger covered area and values than one of the mean. It indicates that there is significant uncertainty of mass fraction of radionuclide arriving at the water table after 1,000 years.

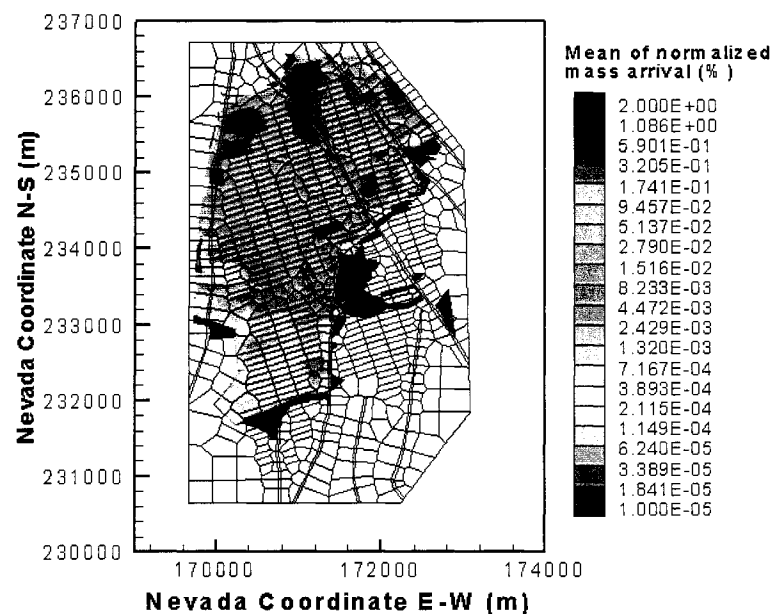


Figure 4.7 Mean of simulated cumulative, normalized mass arrival contours of a conservative tracer (Tc) at water table after 1,000 years for the 3-D domain.

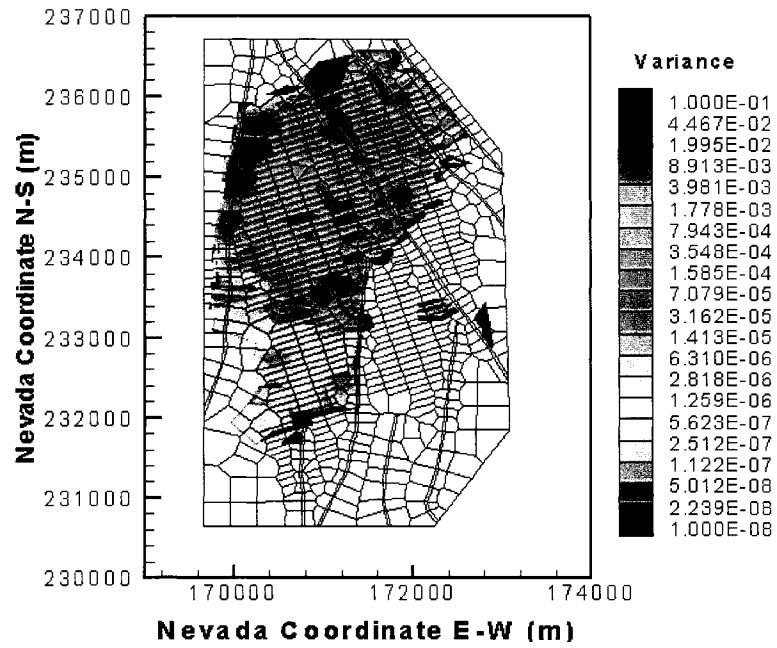


Figure 4.8 Variance of simulated cumulative, normalized mass arrival contours of a conservative tracer (Tc) at water table after 1,000 years for the 3-D domain.

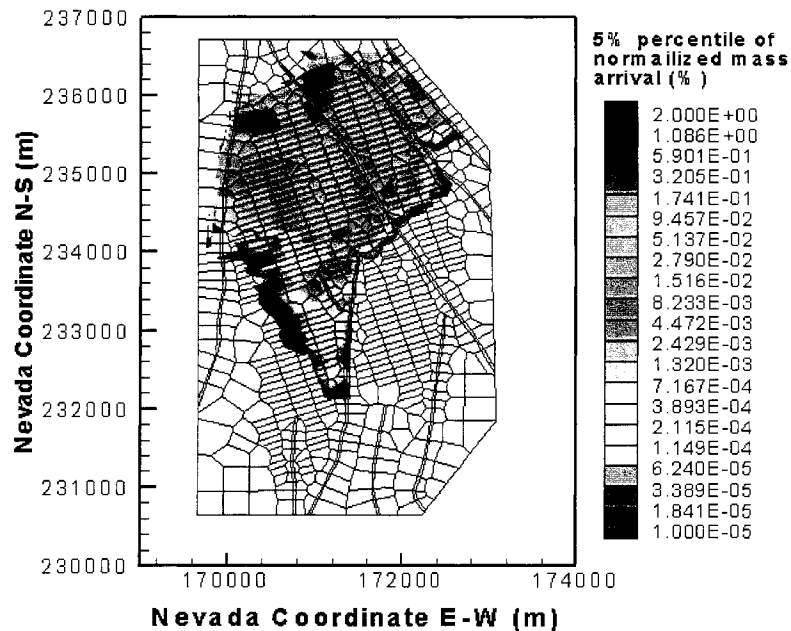


Figure 4.9 5% percentile of simulated cumulative, normalized mass arrival contours of a conservative tracer (Tc) at water table after 1,000 years for the 3-D domain.

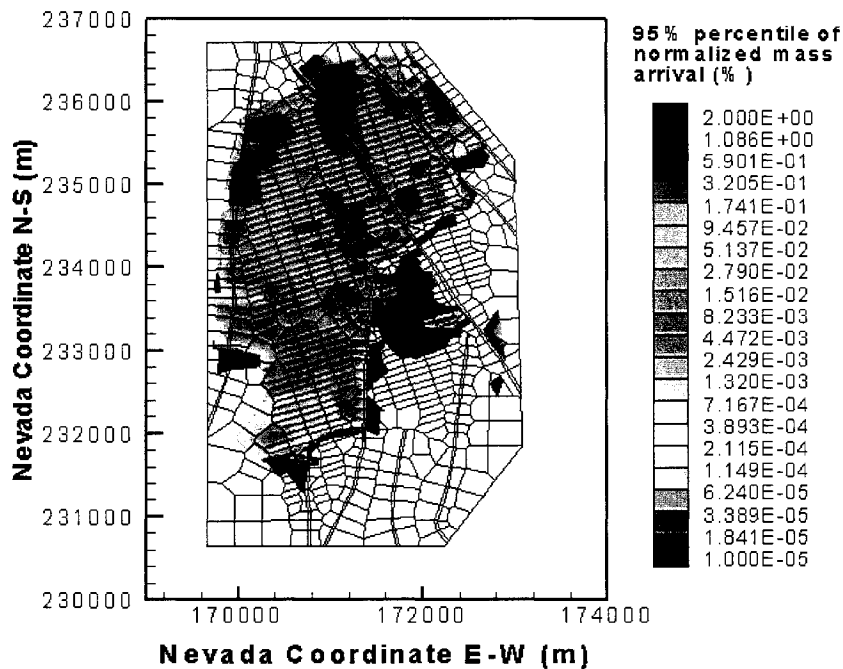


Figure 4.10 95% percentile of simulated cumulative, normalized mass arrival contours of a conservative tracer (Tc) at water table after 1,000 years for the 3-D domain.

The means, variances, 5% and 95% percentiles of cumulative normalized arrival at each grid of water table at 1,000,000 years for ^{99}Tc are shown in Figures 4.11 to 4.14. The mean of mass arrival for ^{99}Tc at 1,000,000 years covers the entire area directly below the repository footprint, spreading to the east of the model domain but does not cover the area in south-east of the model domain. One can also see that the mean of mass arrival for ^{99}Tc at 1,000,000 years has larger value at the area below the repository footprint (Figure 1.1) than the one of other areas. The reason why the radionuclide spreads to east and covers almost the entire model domain is that the lateral flow at the water table affects the spread of transport. Because the simulated lateral flow at the water table in the east of repository footprint is much larger than the one in south-east of model domain, the radionuclide spreads to the east of the repository footprint and does not reach the south-

east of model domain. One can see from Figure 4.12 the largest variance of mass arrival is in west and center of the model domain and it is not the same as the largest mean appeared in the west and north of the model domain. One can see the variance has a similar pattern as the one of simulated fluxes at the water table shown in Figure 3.18. It indicates that the uncertainty of radionuclide mass arrival is correlated with the uncertainty of flow fields when almost all of radionuclide releases from repository has arrived at the water table. The uncertainty of radionuclide can also be quantified by the significant differences between the 5% and 95% percentile contours shown in Figures 4.13 and 4.14. .

The comparisons of the means, variances, 5% and 95% percentiles of the contours at 1,000 years with the ones at 1,000,000 years show the significant differences on contour pattern and values. The ones at 1,000,000 years cover much larger area and have higher concentration of the radionuclide than the ones at 1,000 years, indicating that more radionuclide is transported to the water table with the increase of travel time. The spatial distributions of predictive variance shown in Figures 4.8 and 4.12 have significance difference between 1,000 and 1,000,000 years. The variance of cumulative mass fraction at each grid at 1,000,000 years is larger than the one at 1,000 years in most region of model domain but is smaller in the north boundary of repository footprint. The variance in Figure 4.12 shows a similar pattern as the variance of flow fields at the water table in Figure 3.18. Because 99% (mean) of total radionuclide released from the repository after 1,000,000 years has arrived at the water table shown in Figure 4.5, the uncertainty of radionuclide transport is from the uncertainty of flow fields and random porosity. When the radionuclide releases from the repository at 1,000 years, the variance at 1,000 years

are correlated the corresponding mean of mass arrival because only 38% (mean) of total radionuclide arrives at the water table. For example, the largest variance is around several faults in north of the model domain where the largest mean appears.

By comparing the mean, variance, 5% and 95% percentiles of cumulative normalized mass arrival contours for ^{99}Tc at 1,000,000 years with the mean, variance, 5% and 95% percentiles of simulated percolation fluxes at water table shown in Figures 3.17, 3.18, 3.19 and 3.20, one can know that there are similar patterns between them and the high values of cumulative mass arrival at the water table correspond to high percolation fluxes at water table. It means that the uncertainty of flow fields can cause significant uncertainty of mass fraction of radionuclide.

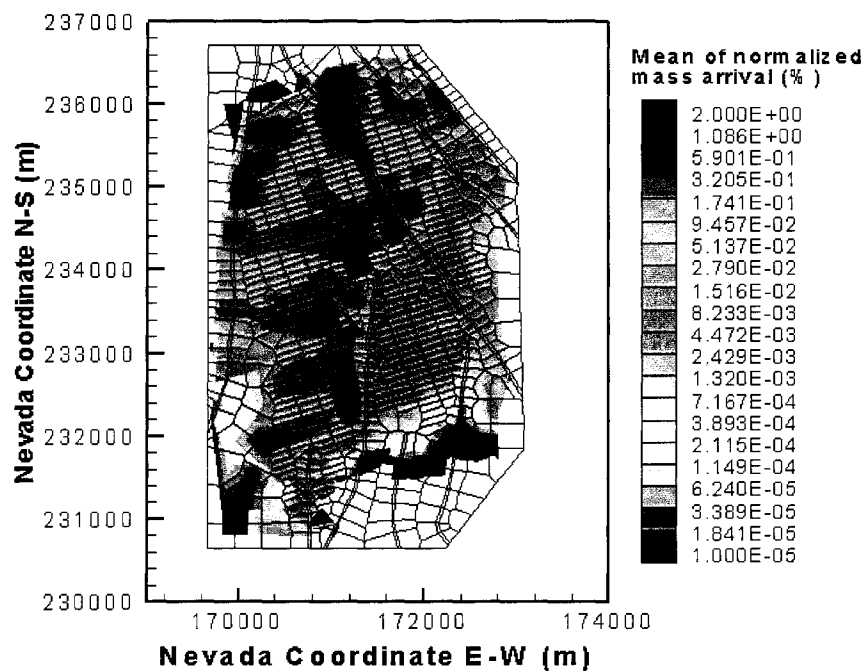


Figure 4.11 Mean of simulated cumulative, normalized mass arrival contours of a conservative tracer (Tc) at water table after 1,000,000 years for the 3-D domain.

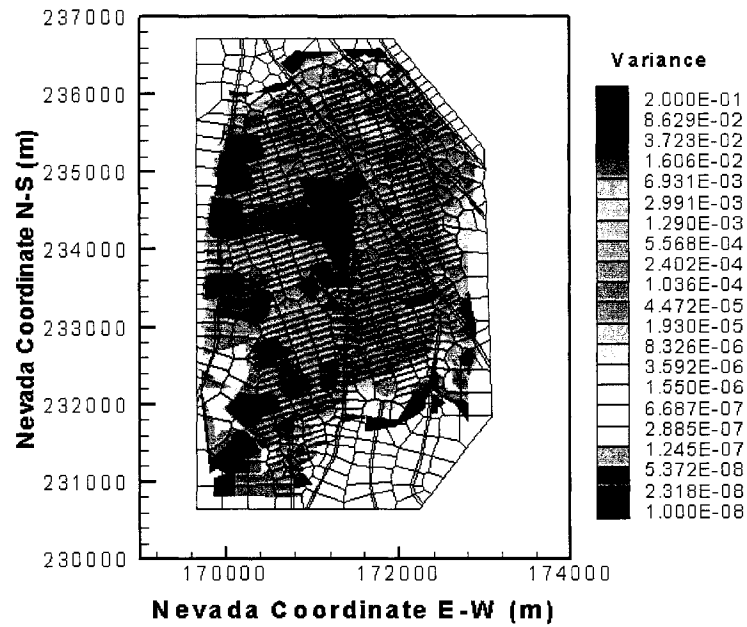


Figure 4.12 Variance of simulated cumulative, normalized mass arrival contours of the conservative tracer at water table after 1,000,000 years for the 3-D domain.

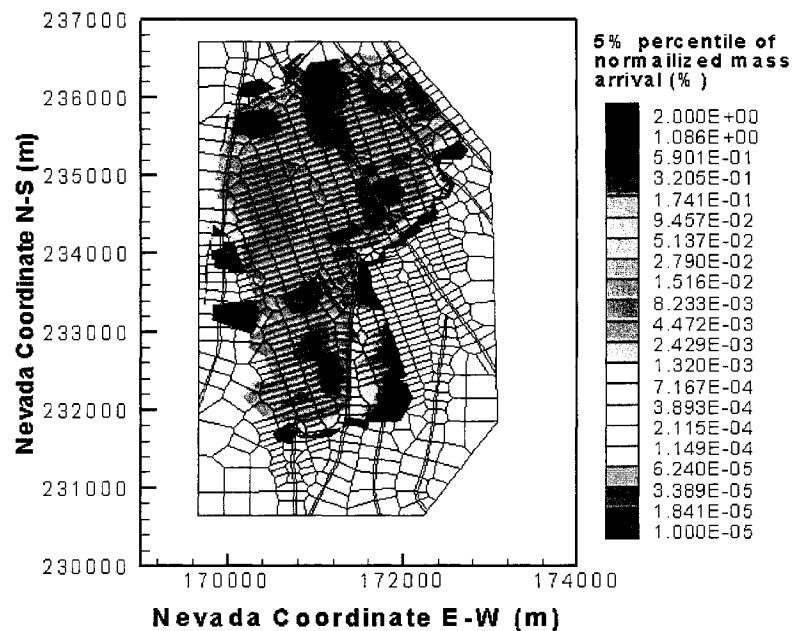


Figure 4.13 5% percentile of simulated cumulative, normalized mass arrival contours of a conservative tracer (Tc) at water table after 1,000,000 years for 3-D domain.

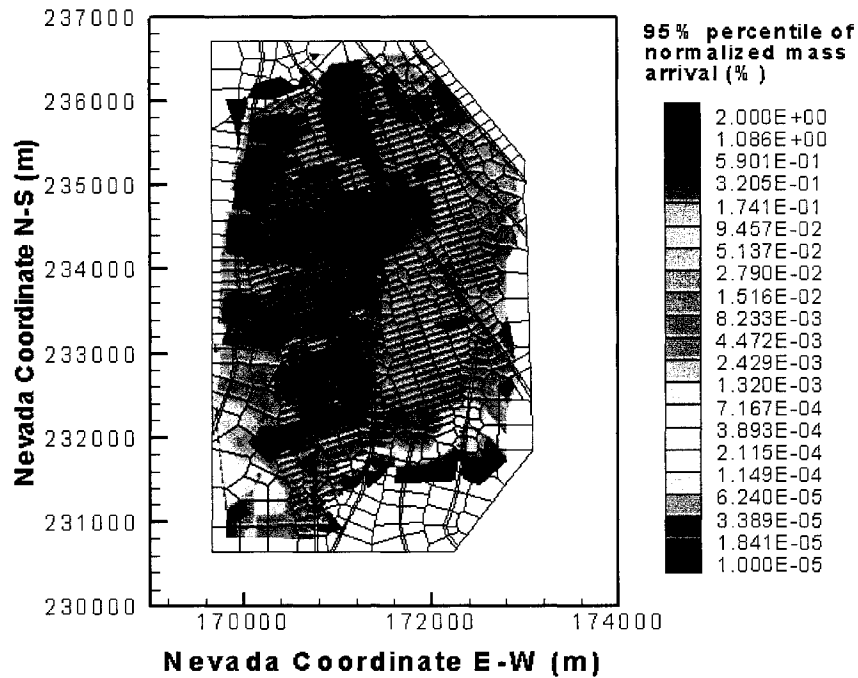


Figure 4.14 95% percentile of simulated cumulative, normalized mass arrival contours of a conservative tracer at water table after 1,000,000 years for 3-D domain.

Figures 4.15 - 4.18 show that the means, variances, 5% and 95% percentiles of cumulative normalized arrival at each grid of water table at 1,000 years for the reactive tracer (^{237}Np). One can see from these figures that they have similar patterns and characteristics as the ones for the conservative tracer (^{99}Tc). Figures 4.7 and 4.15 show a significant different spatial distribution of mean cumulative mass arrival at water table between ^{99}Tc and ^{237}Np at 1,000 years. This is also true for the 5%, 95% percentiles and variances. In general, the means, variances, 5% and 95% percentiles of cumulative mass arrival for ^{237}Np have much smaller covered area and values than the corresponding ones for ^{99}Tc , because the adsorption of the reactive tracer slows down the movement of the tracer transport and the reactive tracer travels much longer time arriving at water table than the conservative one.

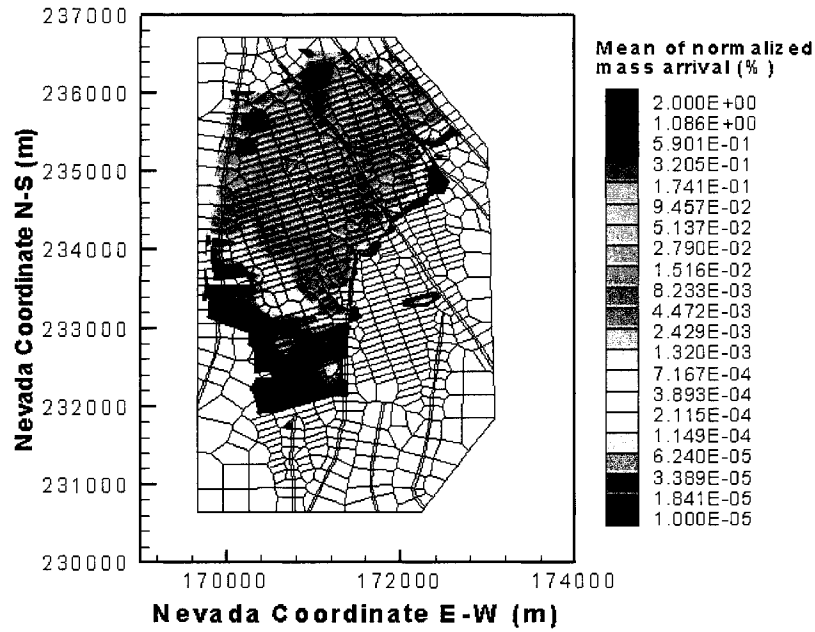


Figure 4.15 Mean of simulated cumulative, normalized mass arrival contours of a reactive tracer (Np) at water table after 1,000 years for the 3-D domain.

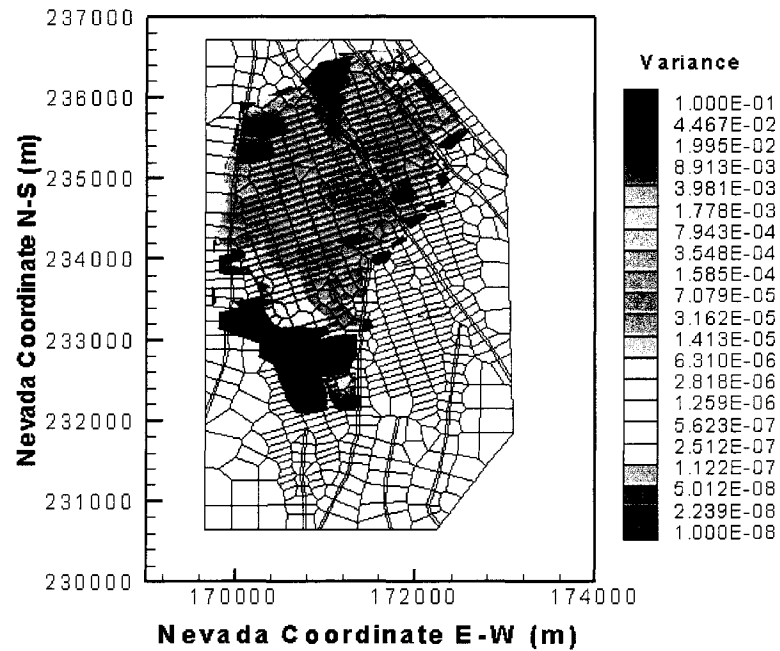


Figure 4.16 Variance of simulated cumulative, normalized mass arrival contours of a reactive tracer (Np) at water table after 1,000 years for the 3-D domain.

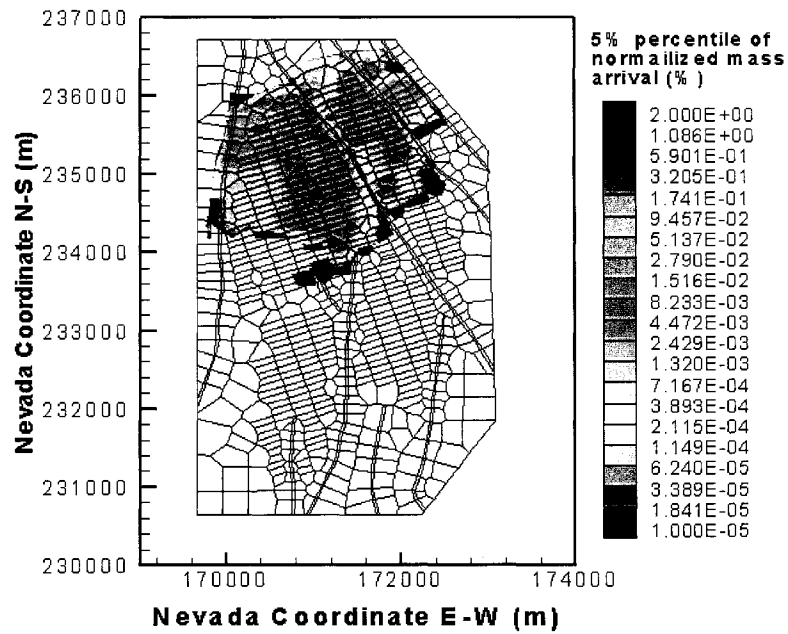


Figure 4.17 5% percentile of simulated cumulative, normalized mass arrival contours of a reactive tracer (Np) at water table after 1,000 years for the 3-D domain.

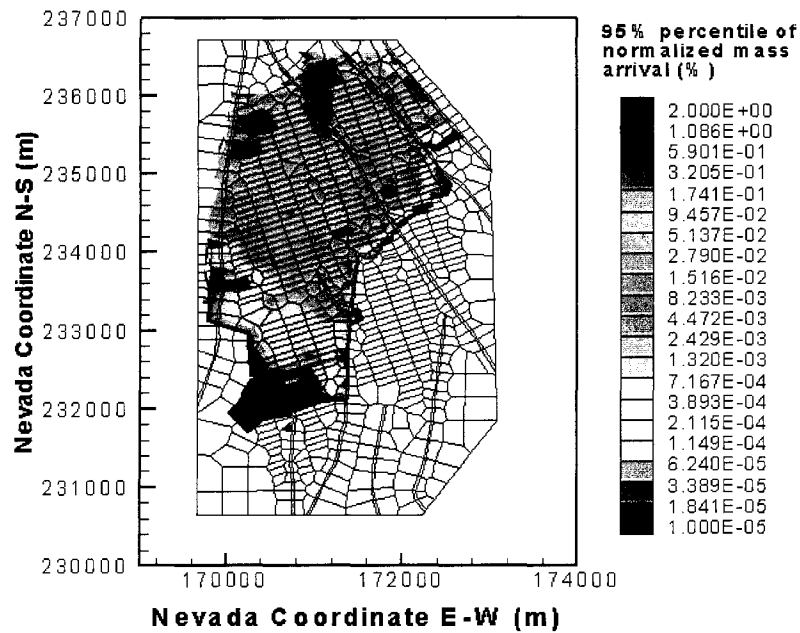


Figure 4.18 95% percentile of simulated cumulative, normalized mass arrival contours of a reactive tracer (Np) at water table after 1,000 years for the 3-D domain.

The means, variances, 5% and 95% percentiles of cumulative normalized arrival at each grid of water table at 1,000,000 years for ^{237}Np are shown in Figures 4.19 to 4.22. One can also see that there are similar patterns and characteristics between the ones for ^{99}Tc and ^{237}Np at 1,000,000 years. Figures 4.11 and 4.19 show no much difference for ^{99}Tc and ^{237}Np in the distribution of the mean of cumulative mass arrival at water table. There are no much difference among their corresponding 5%, 9% percentiles and variances for ^{99}Tc and ^{237}Np . This is because more than 80 percent of both tracers have arrived at water table at this time.

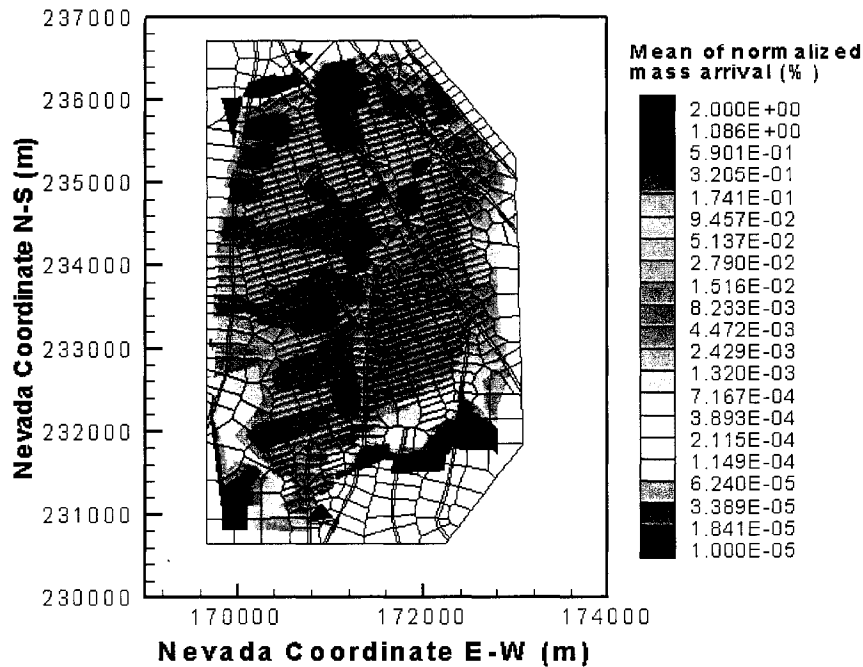


Figure 4.19 Mean of simulated cumulative, normalized mass arrival contours of a reactive tracer (Np) at water table after 1,000,000 years for the 3-D domain.

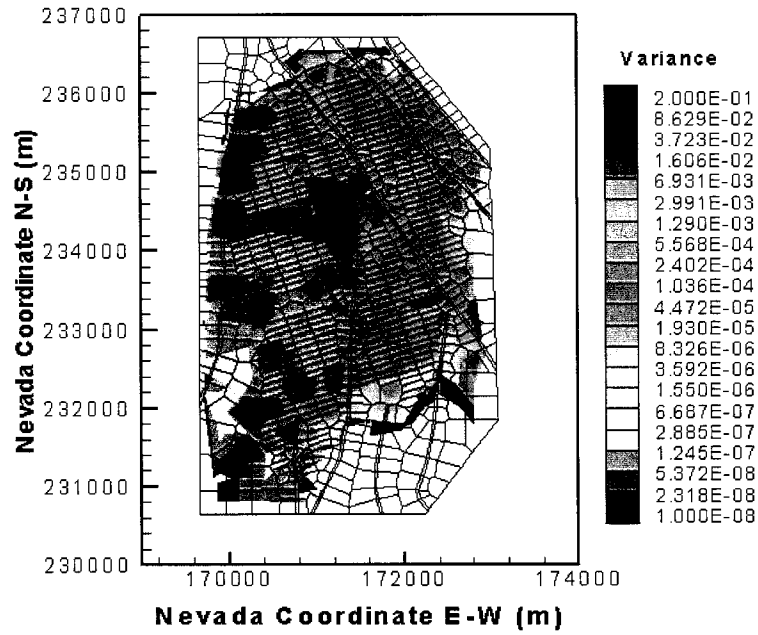


Figure 4.20 Variance of simulated cumulative, normalized mass arrival contours of a reactive tracer (Np) at water table after 1,000,000 years for the 3-D domain.

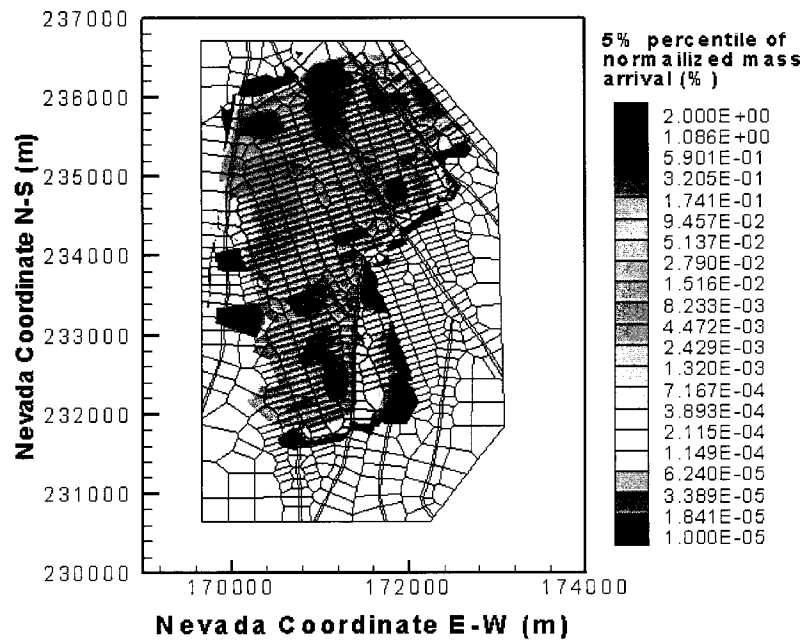


Figure 4.21 5% percentile of simulated cumulative, normalized mass arrival contours of a reactive tracer (Np) at water table after 1,000,000 years for the 3-D domain.

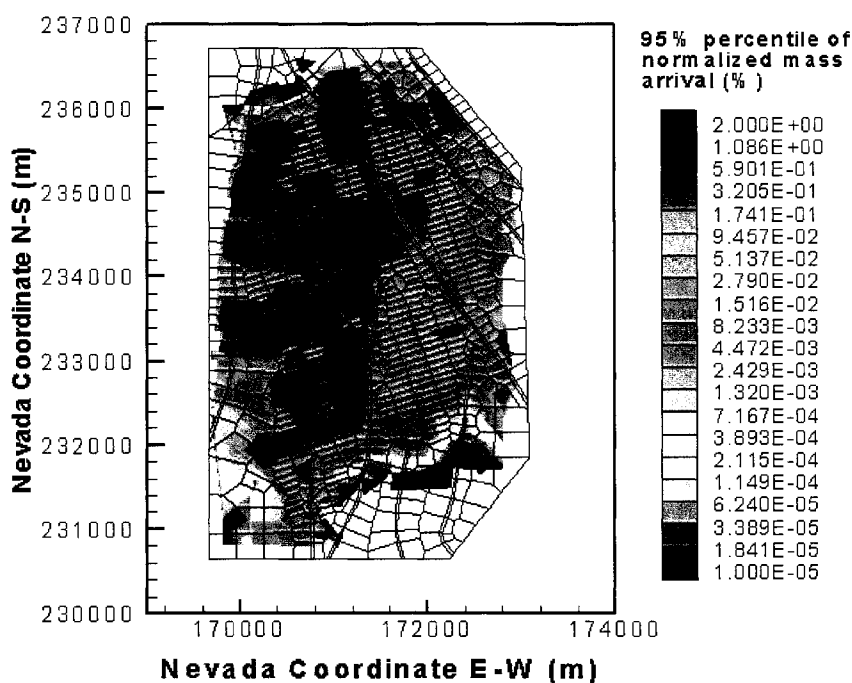


Figure 4.22 95% percentile of simulated cumulative, normalized mass arrival contours of a reactive tracer (Np) at water table after 1,000,000 years for the 3-D domain.

By comparison of the means, variances, 5% and 95% percentiles of cumulative mass arrival contours of ^{237}Np at 1,000 and 1,000,000 years, there are big differences in the patterns and values of cumulative mass arrival at 1,000 and 1,000,000 years between them. The ones at 1,000,000 years cover much larger area and have higher concentration of the radionuclide than the ones at 1,000 years. The main reason is that the mass of radionuclide arriving at water table increases with the increase of the travel time. The uncertainty of radionuclide (^{237}Np) from the uncertainty of flow fields, random porosity and sorption coefficient shows the similar characteristics as the comparisons of ^{99}Tc at 1,000 and 1,000,000 years.

By the above analysis, it can be concluded that the parameter uncertainty in porosity and sorption coefficient and the uncertainties of flow fields have significant

effects on the simulated radionuclide transport in the unsaturated zone at Yucca Mountain. These uncertainties are evaluated by analyzing the means, variances, 5% and 95% percentiles of cumulative mass arrival at water table and travel time from repository to water table.

CHAPTER 5

CONCLUSIONS

In this thesis, the uncertainties of unsaturated flow and radionuclide transport simulations caused from parameter uncertainty in matrix porosity, permeability and sorption coefficient in the unsaturated zone at Yucca Mountain are evaluated by analyzing the means, variances, 5% and 95% percentiles of simulated flow and transport properties (e.g., saturation, capillary pressure, and travel time). The three-dimensional flow and transport model, TOUGH2, and Monte Carlo method are used to simulate the flow and transport with multiple parameter realizations. A recently developed method by Ballio and Guadagnini (2004) is implemented to examine the convergence of Monte Carlo simulation.

To generate random fields of hydraulic parameters, the distributions of matrix porosity, saturated conductivity and sorption coefficient are determined by the Lilliefors Test for normality to select the best fitted transforms from four Johnson transformations and three classic re-expressions based on the field data. The main types of transforms for matrix porosity are NO and 1/X and LN and SB for saturated conductivity. The random fields of matrix porosity, permeability and sorption coefficient with 200 realizations are generated by Latin Hypercube Sampling (LHS) method based on the measured data and used for TOUGH2 code. The generated random fields in hydraulic parameters match well

with the measured data in most layers, indicating that parameter uncertainty in the hydraulic parameters could be represented by the generated random fields.

The simulated water saturation and capillary pressure reach the convergence around 200 realizations after implementing the convergence method by Ballio and Guadagnini (2004). The simulated water saturation and water potential match well the measured profiles at three boreholes and 5% and 95% percentiles cover a large portion of the measured data. The simulated unsaturated flow results indicate that the parameter uncertainty in matrix porosity and permeability have significant effects on the ones at the water table because about 50% of fluxes at the water table are from matrix.

The cumulative fractional mass and travel time of the conservative and reactive tracers with 200 realizations are simulated under steady-state flow fields with constant released tracer at the repository. The convergence analysis indicates that the simulated cumulative fractional mass and travel time have reached the convergence around 200 realizations and are reliable to predict the radionuclide transport. The parameter uncertainty in sorption coefficient and matrix porosity and uncertainties of flow fields could cause significant uncertainties of the conservative and reactive tracers by analyzing the means, 5%, 50% and 95% percentiles of simulated cumulative fractional mass breakthrough arriving at water table. The conservative tracer without sorption could move one or two orders of magnitude faster than the reactive one with random sorption coefficient. The cumulative fractional mass of the conservative tracer arriving at water table at 1,000 years is much larger than the one of the reactive tracer at the same time and there is no much difference between them after the tracer has traveled 1,000,000 years.

The uncertainties of radionuclide transport are also evaluated by means, variances, 5% and 95% percentiles of cumulative normalized mass arrival contours at water table.

Uncertainty analysis conducted in this research indicates that parametric uncertainty in matrix porosity, permeability, and sorption coefficient have significant effects on the uncertainties of unsaturated flow and radionuclide transport in the unsaturated zone. The completed research provides the optimum prediction and associated predictive uncertainty, which can be used for decision making and guide future system characterization. Nevertheless, van Genuchten α and n parameters are not treated as random due to the lack of measurements, which may cause underestimation of uncertainty. This problem will be resolved in the future research and sensitivity analysis will also be conducted to determine which parameter is the most sensitive one to flow and radionuclide transport sensitivity predictive uncertainty.

APPENDIX A

METHODOLOGY OF FLOW AND TRANSPORT SIMULATION

A.1 Convergence Analysis of Monte Carlo Simulation

Because there are no standard convergence criteria in Monte Carlo simulations, various methods for convergence analysis have been developed to evaluate the convergence (Bellin et al., 1992; Burr et al., 1994; Hassan et al., 1998; Ballio and Guadagnini, 2004). Ballio and Guadagnini (2004) proposed a new method for convergence analysis of Monte Carlo Simulation by estimating the ensemble mean and variance of random variables within a given confidence intervals. Therefore, the newly developed method for convergence analysis was implemented in this study. The properties of the sample mean and variance of random variable \mathfrak{R} are as follows (Ballio and Guadagnini, 2004):

$$\langle \overline{\mathfrak{R}_n} \rangle = \mu; \quad \text{var}[\overline{\mathfrak{R}_n}] = \frac{1}{n} \sigma^2; \quad (\text{A.1})$$

$$\langle S_n^2 \rangle = \sigma^2; \quad \text{var}[S_n^2] = \frac{1}{n} \left(\mu_4 - \frac{n-3}{n-1} \sigma^4 \right) \quad (\text{A.2})$$

where $\overline{\mathfrak{R}}$ is the sample mean of \mathfrak{R} ; μ is the ensemble mean of \mathfrak{R} ; S_n^2 is the sample variance; σ^2 is the ensemble variance; and μ_4 is ensemble kurtosis.

If \mathfrak{R} is normal, then

$$\frac{\bar{R}_n - \mu}{\sigma / \sqrt{n}} \sim N_{0,1}(\); \quad \text{and} \quad \frac{\bar{R}_n - \mu}{S_n / \sqrt{n}} \sim t_{n-1}(\) \quad \forall n \quad (\text{A.3})$$

$$\text{var}[S_n^2] = \frac{2}{n-1} \sigma^4 \quad (\text{A.4})$$

$$\sum_{i=1,n} \frac{(\mathfrak{R}_i - \mu)^2}{\sigma^2} \sim \chi_n^2(\); \quad \sum_{i=1,n} \frac{(\mathfrak{R}_i - \bar{\mathfrak{R}}_n)^2}{\sigma^2} = (n-1) \frac{S_n^2}{\sigma^2} \sim \chi_{n-1}^2(\) \quad (\text{A.5})$$

where $N_{0,1}(\)$ is the standard normal distribution; $t_{n-1}(\)$ is the student distribution with $(n-1)$ degrees of freedom; and χ_{n-1}^2 is the chi-square distribution with $(n-1)$ degrees of freedom.

Therefore, according to the above the equations, the estimation of the uncertainty by the evaluation of confidence intervals are (Ballio and Guadagnini, 2004):

$$\Pr \left[\bar{\mathfrak{R}}_n - t_{n-1} \left(1 - \frac{\alpha}{2}\right) \frac{S_n}{\sqrt{n}} \leq \mu \leq \bar{\mathfrak{R}}_n + t_{n-1} \left(1 - \frac{\alpha}{2}\right) \frac{S_n}{\sqrt{n}} \right] = 1 - \alpha \quad (\text{A.6})$$

$$\Pr \left[\frac{n-1}{\chi_{n-1}^2(1-\alpha/2)} S_n^2 \leq \sigma^2 \leq \frac{n-1}{\chi_{n-1}^2(\alpha/2)} S_n^2 \right] = 1 - \alpha \quad (\text{A.7})$$

where $1 - \alpha$ is the probability that the value of μ lies within the confidence interval around sample mean $\bar{\mathfrak{R}}_n$.

According to Equations (A.3) and (A.4), the confidence intervals (upper bound and lower bound) of the ensemble mean and variance can be obtained for a given number of realizations. Thus, the number of realizations that assures convergence can be determined.

A.2 TOUGH2

TOUGH2, a numerical model, was developed to simulate flow and transport processes in the unsaturated zone system at Yucca Mountain and can be used for modeling flow and transport in heterogeneous fractured rocks (Wu et al., 2004a). TOUGH2 modules such as saturated/unsaturated flow (EOS9) and radionuclide transport (T2R3D) were supplemented in TOUGH2 code and also quality approved by U.S. Department of Energy (DOE) to study groundwater flow and solute transport at Yucca Mountain in 1996 (Wu, et al., 1996). The modules of EOS9 and T2R3D were used to simulate flow and transport in the unsaturated zone at Yucca Mountain respectively. A new dual-continua method such as multiple-porosity and dual-permeability has been implemented into TOUGH2 to handle the fracture-matrix interactions of flow and transport in a fractured medium (Wu and Pruess, 2000). The dual-continua approach was applied to both fractures and matrix respectively to simulate the processes of flow and transport.

A.2.1 EOS9 Module

EOS9 is a saturated-unsaturated flow module based on the Richard's equation, the conservation of mass and Darcy's law and can be used to simulate the multi-phase liquid flow in the saturated and unsaturated heterogeneous media (Wu et al., 1996; Wu et al., 2004a).

In TOUGH2, the basic mass and energy equations for fracture or matrix in the dual-continuum system are (Pruess et al., 1999, Wu et al., 2004a):

$$\frac{d}{dt} \int_{V_n} M_f^k dV_n = \int_{\Gamma_n} F_f^k \cdot n \cdot d\Gamma_n + \int_{V_n} (q_f^k + q_{fm}^k) dV_n \quad (\text{A.8})$$

$$\frac{d}{dt} \int_{V_n} M_m^k dV_n = \int_{\Gamma_n} F_m^k \cdot n \cdot d\Gamma_n + \int_{V_n} (q_m^k - q_{fm}^k) dV_n \quad (\text{A.9})$$

where subscripts f, m stand for fracture continuum and matrix continuum respectively; M^k is mass or energy per volume; F^k is mass or heat flux; q^k is sinks and sources; $\kappa = 1, \dots, NK$ is the mass components (air, water and radionuclide etc.); Γ_n is the closed surface; and V_n is an arbitrary subdomain.

The general form of the mass accumulation term is (Pruess et al., 1999):

$$M^k = \phi \sum_{\beta} S_{\beta} \rho_{\beta} X_{\beta}^k \quad (\text{A.10})$$

where subscript β stands for fluid phases (e.g., liquid, gas or radionuclide); ϕ is porosity; S_{β} is saturation of phase β ; ρ_{β} is the density of phase β ; and X_{β}^k is the mass fraction of component k present in phase β .

Darcy's law was also used in EOS9 and can be written as (Wu et al., 2004a):

$$F_p = \rho u_p = -k_p \frac{k_{rp} \rho}{\mu} (\nabla P_p - \rho g) \quad (\text{A.11})$$

where subscript p stands for fracture continuum f or matrix continuum m ; F_p is mass flux; u_p is the Darcy velocity (volume flux); k_p is absolute permeability; k_{rp} is relative permeability; μ is viscosity; g is gravity acceleration constant; and P_p is capillary pressure. The capillary pressure can be calculated by the following equation:

$$P_p = -P_{pg} + P_{pl} \quad (\text{A.12})$$

where P_{pl} is water phase pressure and P_{pg} is the gas pressure.

The Richards' equation can be expressed as (Pruess et al., 1999; Wu et al., 2004a):

$$\frac{\partial}{\partial t} \theta_f = \text{div}[K_f \nabla \psi_f] + q_f + q_{fm} \quad (\text{A.13})$$

$$\frac{\partial}{\partial t} \theta_m = \text{div}[K_m \nabla \psi_m] + q_m - q_{fm} \quad (\text{A.14})$$

where $\theta_p = \phi_p S_p$ is specific volumetric moisture content for fracture or matrix;

where $\theta = \phi S_l$ is specific volumetric moisture content; $K_p = k_p k_{rp} \rho g / \mu$ is hydraulic conductivity; and $\psi_p = z + P_p / (\rho g)$ is the total water potential, z is elevation.

Van Genuchten model was also used in EOS9 module to calculate water capillary pressure and relative permeability for matrix continuum and fracture continuum. The capillary pressure for matrix continuum (P_m) and fracture continuum (P_f) can be described as (van Genuchten, 1980; Liu et al., 1998; Wu et al., 2004a):

$$P_m(S_{em}) = \frac{1}{\alpha_m} [S_{em}^{-1/m_m} - 1]^{1/n_m} \quad (\text{A.15})$$

$$P_f(S_{ef}) = \frac{1}{\alpha_f} [S_{ef}^{(\gamma-1)/m_f} - 1]^{1/n_f} \quad (\text{A.16})$$

where $\alpha_p, n_p, m_p = 1 - 1/n_p$ are van Genuchten parameters for matrix or fracture continuum; γ is the active fracture parameter; and S_{ep} is the effective water saturation of matrix or fracture continuum. It can be written as:

$$S_{ep} = \frac{S_p - S_{rp}}{1 - S_{rp}} \quad (\text{A.17})$$

where S_p is the water saturation of matrix or fracture; and S_{rp} is the residual saturation of matrix or fracture.

The relative permeability for matrix continuum (k_{rm}) and fracture continuum (k_{rf}) can be given as (Liu et al., 1998; Wu et al., 2004a):

$$k_{rm} = S_{em}^{1/2} [1 - \{1 - S_{em}^{1/m}\}^m]^2 \quad (A.18)$$

$$k_{rf} = S_{ef}^{(1+\gamma)/2} [1 - \{1 - S_{ef}^{(1-\gamma)/m_f}\}^{m_f}]^2 \quad (A.19)$$

A fracture-matrix interface area reduction factor (R) was introduced by Liu et al. (1998) to handle the flow and transport between fracture and matrix. It can be expressed as:

$$R \cong S_{ef}^{1+\gamma} \quad (A.20)$$

According the reduction factor (R) and interface area (A) between fracture and matrix, the fracture-matrix exchange flux (q_{fm}) can be calculated by the following formula (Wu et al., 2004a):

$$q_{fm} \propto RA \frac{\psi_m - \psi_f}{l_f} \quad (A.21)$$

where l_f is the characteristic distance for fracture-matrix flow.

A.2.2 T2R3D Module

T2R3D is a radionuclide transport module based on mass conservation equation and basic solute transport equations and can be used to simulate the transport of radionuclide or liquid tracers in multiphase groundwater systems (Wu, et al., 1996).

The governing equation for radionuclide within the fracture or matrix continuum can be written as (Wu et al., 2000):

$$\frac{\partial}{\partial t} \{ \phi \sum_{\beta} \rho_{\beta} S_{\beta} X_{\beta}^k \} + (1 - \phi) \rho_s \rho_L X_L^k K_d^k \} + \lambda_k \{ \phi \sum_{\beta} \rho_{\beta} S_{\beta} X_{\beta}^k \} + (1 - \phi) \rho_s \rho_L X_L^k K_d^k \} =$$

$$-\sum_{\beta} \nabla \cdot (\rho_{\beta} X_{\beta}^k v_{\beta}) + \sum_{\beta} \nabla \cdot (\rho_{\beta} \underline{D}_{\beta}^k \cdot \nabla X_{\beta}^k) + q^k \quad (\text{A.22})$$

where ρ_s is the density of rock grains; ρ_L is the density in the liquid phase; X_L^k is mass fraction of component k in the liquid phase; K_d^k is the distribution coefficient of component k between the liquid phase; λ_k is radioactive decay constant of radionuclide ($k = 3$ only); v_{β} is Darcy's velocity of phase β ; and \underline{D}_{β}^k is diffusion-dispersion tensor for component k in phase β .

Therefore, the Mass flux for the radionuclide in the liquid phase can be described by (Wu et al., 1996):

$$F^k = F_A^k + F_D^k \quad (\text{A.23})$$

where F_A^k is mass flux by advection, and F_D^k is mass flux by dispersion and diffusion.

The mass flux by advection can be defined as (Wu et al., 1996):

$$F_A^k = X_{\beta}^k F_{\beta} \quad (\text{A.24})$$

where F_{β} is liquid flux by Darcy's law.

The mass flux by dispersion and diffusion can be written as (Wu et al., 1996):

$$F_D^k = -\rho_{\beta} \underline{D} \cdot \nabla X_{\beta}^k \quad (\text{A.25})$$

where \underline{D} is the combined diffusion-dispersion tensor for both molecular diffusion and hydraulic dispersion. The hydrodynamic dispersion tensor with three types of flow can be described by a general dispersion model for fracture and matrix systems (Wu et al., 2000). The equations are as follows:

For transport in fractures:

$$\underline{D}_{\beta,f} = \alpha_{T,f} |v_{\beta,f}| \delta_{ij} + (\alpha_{L,f} - \alpha_{T,f}) \frac{v_{\beta,f} v_{\beta,f}}{|v_{\beta,f}|} + \phi_f S_{\beta,f} \tau_f d_f \delta_{ij} \quad (\text{A.26})$$

For transport in matrix:

$$\underline{D}_{\beta,m} = \alpha_{T,m} |v_{\beta,m}| \delta_{ij} + (\alpha_{L,m} - \alpha_{T,m}) \frac{v_{\beta,m} v_{\beta,m}}{|v_{\beta,m}|} + \phi_m S_{\beta,m} \tau_m d_m \delta_{ij} \quad (\text{A.27})$$

For diffusive transport processes between fracture and matrix or inside matrix:

$$\underline{D}_{\beta,fm} = \alpha_{fm} |v_{\beta,fm}| + \phi_m S_{\beta,m} \tau_m d_m \quad (\text{A.28})$$

where $\underline{D}_{\beta,p}$ is combined diffusion-dispersion tensors for transport through fractures, matrix, and between fractures and matrix or inside matrix; $\alpha_{T,p}, \alpha_{L,p}$ are transverse and longitudinal dispersivities of fractures and matrix respectively; α_{fm} is longitudinal dispersivity along fracture-matrix or inner matrix-matrix connections; τ_p is the tortuosity of fracture or matrix continuum; d_p is the molecular diffusion coefficient in phase β ; and δ_{ij} is Kroneker delta function.

Two types of radionuclides, conservative tracers and reactive tracers, can be handled in T2R3D module. For reactive tracers, the radioactive decay constant of the radionuclide (λ_k) can be defined as:

$$\lambda_k = \frac{\ln(2)}{T_{1/2}} \quad (\text{A.29})$$

where $T_{1/2}$ is the half-life of the radionuclide component.

For mass transport with sorption, the retardation equation can be written as (Domenico and Schwartz, 1990):

$$R_f = 1 + \left(\frac{1 - \phi}{\phi} \right) \rho_\beta K_d \quad (\text{A.30})$$

where R_f is the retardation coefficient.

A.2.3 Numerical Scheme

Numerical scheme is necessary to solve the governing and conservation equations of flow and transport. In TOUGH2, an integral finite-difference method was implemented to discretize the equations in space and a backward, first-order, finite-difference scheme was used to discretize them in time (Pruess, et al., 1999; Wu et al., 2000). The discretization approach with the integral finite difference method and the definition of the geometric variables are shown in Figure A.1.

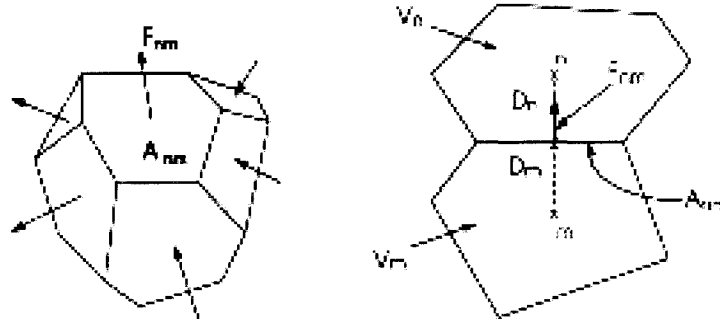


Figure A.1 Space discretization and geometry variables in the integral finite-difference method (Pruess, et al., 1999; Wu et al., 2000).

By implementing the numerical scheme of space and time discretization in TOUGH2, the discrete non-linear equations at gridblock n can be expressed as (Pruess et al., Wu et al., 2000):

$$R_n^{k,t+1} = M_n^{k,t+1} (1 + \lambda_k \Delta t) - M_n^{k,t} - \frac{\Delta t}{V_n} \left\{ \sum_m (A_{nm} F_{nm}^{k,t+1}) + V_n q_n^{k,t+1} \right\} \quad (\text{A.31})$$

where superscript $t + 1$ is current time step; Δt is time step size; subscripts n and nm are element n and connection between element n and element m ; m is a neighbor element connected with element n directly; V_n is the volume of element n ; M_n is the average value of accumulation term of mass or energy over element volume V_n ; F_{nm} is the average value of the normal component mass or heat fluxes, over the surface segment area, A_{nm} , between volumes V_n and V_m ; q_n is source/sink term; and R_n is the residuals of mass or energy.

In TOUGH2, a spatial and harmonic weighting scheme was used to convert the velocities along connections in the local coordinate system to a velocity vector in global coordinate system (Pruess et al., 1999, Wu et al., 2000). The schematic illustration of the weighting scheme for velocity fields was shown in Figure A.2. A global velocity component ($v_{n,i}$) of the vector (v_n) can be calculated by a weighting scheme of projected area weighting method. It was expressed as follows (Pruess et al., 1999):

$$v_{n,i} = \frac{\sum_m (A_{nm} |n_i|) (v_{nm} n_i)}{\sum_m (A_{nm} |n_i|)} \quad (i = x, y, z) \quad (\text{A.32})$$

where m is the total number of connections between element V_n and all its neighboring elements V_m ; v_{nm} is the Darcy's velocity along connection nm in the local coordinate system; $(A_{nm} |n_i|)$ is the projected area of the interface A_{nm} on to direction i of the global coordinate system; and $(v_{nm} n_i)$ is the velocity component in the direction i of global coordinate system.

The harmonic weighting scheme was used to calculate the velocity vector v at the interface of elements n and m by the distances (D_n, D_m) from the block cents of the two elements to the interface (Pruess et al., 1999). The formula can be written as:

$$\frac{D_n + D_m}{V_i} = \frac{D_n}{V_{n,i}} + \frac{D_m}{V_{m,i}} \quad (i = x, y, z) \quad (\text{A.33})$$

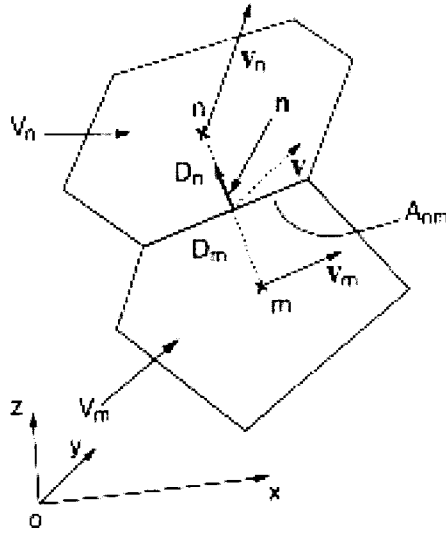


Figure A.2 Schematic illustration of spatial weighting scheme for velocity fields (Pruess et al., 1999; Wu et al., 2000).

Therefore, the concentration or mass fraction gradient of the radionuclide at element n (∇X_n^k) can be evaluated by the interface area weighting scheme (Pruess et al., 1999; Wu et al., 2000). It was as follows:

$$\nabla X_n^k = \frac{\sum_m A_{nm} \nabla X_{nm}^k}{\sum_m A_{nm}} \quad (\text{A.34})$$

where ∇X_{nm}^k is the mass fraction gradient of the radionuclide at the interface between gridblocks n and m . It can be expressed as (Pruess et al., 1999):

$$\nabla X_{nm}^k = (n_x \Delta X_{nm}^k, n_y \Delta X_{nm}^k, n_z \Delta X_{nm}^k) \quad (\text{A.35})$$

where

$$\Delta X_{nm}^k = \frac{X_m^k - X_n^k}{D_m + D_n} \quad (\text{A.36})$$

The mass flux of diffusion and dispersion of the radionuclide along the connection of two elements ($F_{D,nm}^k$) can be calculated by the following formula (Wu et al., 2000):

$$F_{D,nm}^k = n \cdot F_D^k = -n \cdot [\rho_\beta \underline{D}_\beta^k \cdot \nabla X_\beta^k] \quad (\text{A.37})$$

The mass flux of advection of component k along the connection of two elements ($F_{A,nm}^k$) can also be obtained (Wu et al., 2000):

$$F_{A,nm}^k = \sum_{\beta} (X_\beta^k)_{nm} F_{\beta,nm} \quad (\text{A.38})$$

where $F_{\beta,nm}$ is the mass fluxes of phase β along the connection nm . It was written as (Wu et al., 2000):

$$F_{\beta,nm} = \rho_\beta v_\beta = -\left\{ k_{nm} \left[\frac{k_{r\beta} \rho_\beta}{\mu_\beta} \right]_{nm} \left[\frac{P_{\beta,m} - P_{\beta,n}}{D_{nm}} - \rho_{\beta,nm} g_{nm} \right] \right\} \quad (\text{A.39})$$

Equations (4.37) and (4.38) were used in T2R3D module to evaluate the dispersive and advective mass transport terms for Equation (4.23). The dispersive and advective mass flux along the connection of two elements can be obtained by the above equations.

REFERENCES

- Bakker, M., E.I. Anderson, T.N. Olsthoorn, and O.D.L. Strack, 1999. Regional groundwater modeling of the Yucca Mountain site using analytic elements, *J. Hydrol.*, 226, 167-178.
- Balakrishnan, S., A. Roy, M.G. Ierapetritou, G.P. Flach, and P.G. Georgopoulos, 2005. A comparative assessment of efficient uncertainty analysis techniques for environment fate and transport models: application to the FACT model, *J. Hydro.*, 307, 204-218.
- Ballio, F., and A. Guadagnini, 2004. Convergence assessment of numerical Monte Carlo simulations in groundwater hydrology, *Water Resour. Res.*, 10(4), W04603.
- Bellin, A., P. Salandin, and A. Rinaldo, 1992. Simulation of dispersion in heterogeneous / porous formations: Statistics, first-order theories, and convergence of computations, *Water Resour. Res.*, 28(9), 2211-2227.
- Bellin, A., Y. Rubin, and A. Rinaldo, 1994. Eulerian-Lagrangian approach for modeling of flow and transport in heterogeneous geological formations, *Water Resour. Res.*, 30(11), 2913-2924.
- Bodvarsson, G.S., H.H. Liu, R. Ahlers, Y.S. Wu, and E. Sonnenthal, 2001. Parameterization and upscaling in modeling flow and transport at Yucca Mountain. Conceptual Models of Flow and Transport in the Fractured Vadose

- Zone, National Research Council. National Academy Press, Washington, DC.
- Bowen, W.M., and C. A. Bennett, 1988. Statistical methods for nuclear material management, NUREG/CR-4604, Battelle Pacific Northwest laboratory, Richland, WA.
- Burr, D.T., and E.A. Sudicky, 1994. Nonreactive and reactive solute transport in three-dimensional heterogeneous porous media: mean displacement, plume spreading, and uncertainty, *Water Resour. Res.*, 30(3), 791-815.
- Carsel, R.F., and R.S. Parrish, 1988. Developing joint probability distributions of soil water retention characteristics, *Water Resour. Res.*, 24(5), 755-769.
- Cowles, M.K., and B.P. Carlin, 1996. Markov chain Monte Carlo convergence diagnostics: a comparative study, *J. Amer. Statist. Assoc.*, 91, 883-904.
- Deutsch, C.V., and A.G. Journel, 1998. GSLIB: Geostatistical software library and user's guide, Oxford University Press, 369p.
- Domenico, P.A., and F.W. Schwartz, 1990. Physical and chemical hydrogeology, John Wiley & Sons, Inc., 506p.
- Dou, C., W. Woldt, I. Bogardi and M. Dahab, 1995. Steady state groundwater flow simulation with imprecise parameters, *Water Resour. Res.*, 31(11), 2709-2719.
- Fenelon, J.M., and M.T. Moreo, 2002. Trend analysis of ground-water levels and spring discharge in the Yucca Mountain region, Nevada and California, 1960-2000, U.S. Geological Survey, Water-Resources Investigations Report 02-4178.
- Flint, L.E., 2003. Physical and hydraulic properties of volcanic rocks from Yucca Mountain, Nevada, *Water Resour. Res.*, 39(5), 1-13.
- Flint, L.E., 1998. Characterization of hydrogeologic units using matrix properties, Yucca

- Mountain, Nevada, U.S. Geological Survey, Water- Resources Investigations Report, 97-4243.
- Freeze, R.A., 1975. A stochastic-conceptual analysis of one-dimensional groundwater flow in nonuniform homogeneous media, *Water Resour. Res.*, 11(5), 725-741.
- Hassan, A.E., J.H. Cushman, and J.W. Delleur, 1998. A Monte Carlo assessment of Eulerian flow and transport perturbation models, *Water Resour. Res.*, 34(5), 1143-1163.
- Helton, J.C., and F.J. Davis, 2003. Latin hypercube sampling and the propagation of uncertainty in analyses of complex systems, *Reliability Engineering & System Safety*, 81, 23-69.
- Iman, R.L., and W.J. Conover, 1982. A distribution-free approach to inducing rank correlation among input variables, *Commu. Statist. Simula. Computa.*, 11(3), 311-334.
- James, A.L., and C.M. Oldenburg, 1997. Linear and Monte Carlo uncertainty analysis for subsurface contaminant transport simulation, *Water Resour. Res.*, 33(11), 2495-2508.
- Johnson, N.L., and S. Kotz, 1970. Distributions in Statistics: Continuous Univariate Distributions, Vol. 1, Houghton Mifflin Company, Boston, Mass.
- Kitanidis, P., 1997. Introduction to Geostatistics: Application in Hydrogeology, Cambridge University Press, 249p.
- Kupfersberger, H., and C.V. Deutsch, 1999. Ranking stochastic realizations for improved aquifer response uncertainty assessment, *J. Hydro.*, 223, 54-65.
- Liu, H.H., Doughty, C., and G.S. Bodvarsson, 1998. An active fracture model for

- unsaturated flow and transport in fractured rocks, *Water Resour. Res.*, 34(10), 2633-2646.
- Liu, H.H., M. Zhang, P. Persoff, K. Gilkerson, Y.S., Wu, and J.S.Y. Wang, 2003. Analysis of Hydrologic Properties Data, AMR Report MDL-NBS-HS-000014 REV00, Berkeley, CA, Lawrence Berkeley National Laboratory, Las Vegas, Nevada, CRWMS M&O.
- Lu, Z., and D. Zhang, 2003. On importance sampling Monte Carlo approach to uncertainty analysis for flow and transport in porous media, *Adv. Water Resour.*, 26,1177-1188.
- Mallants, D., D. Jacques, M. Vanclooster, J. Diels, and J. Feyen, 1996. A stochastic approach to simulate water flow in a macroporous soil, *Geoderma*, 10, 299-324.
- Mckay, M.D., R.J. Beckman, and W.J. Conover, 1979. A comparison of three methods for selecting values of input variables in the analysis of output from a computer code, *Technometrics*, 21(2), 239-245.
- Mclaren, R.G., P.A. Forsyth, E.A. Sudicky, J.E. VanderKwaak, F.W. Schwartz, and J. H. Kessler, 2000. Flow and transport in fractured tuff at Yucca Mountain: numerical experiments on fast preferential flow mechanisms, *J. Contam. Hydrol.*, 43, 211-238.
- Naff, R.L., D.F. Haley, and E.A. Sudicky, 1998a. High-resolution Monte Carlo simulation of flow and conservative transport in heterogeneous porous media 1. Methodology and flow results, *Water Resour. Res.*, 34(4), 663-677.
- Naff, R.L., D.F. Haley, and E.A. Sudicky, 1998b. High-resolution Monte Carlo simulation of flow and conservative transport in heterogeneous porous media 2.

- Transport results, *Water Resour. Res.*, 34(4), 679-697.
- Nichols, W.E., and M.D. Freshley, 1993. Uncertainty analyses of unsaturated zone travel time at Yucca Mountain, *Ground water*, 31(2), 293-301.
- Oakley, J., 2004. Estimating percentiles of uncertain computer code outputs, *Appl. Statist.*, 53, 83-93.
- Painter, S.,J. Winterle, and A. Armstrong, 2003. Using temperature to test models of flow near Yucca Mountain, Nevada, *Ground Water*, 41(5), 657-666.
- Pruess, K., C. Oldenburg, and G. Moridis, 1999. TOUGH2 user's guide, version 2.0, Lawrence Berkeley Laboratory Report, LBL-43134, Berkeley, CA.
- Ritcey, A.C., and Y.S. Wu, 1999. Evaluation of the effect of future climate change on the distribution and movement of moisture in the unsaturated zone at Yucca Mountain, NV, *J. Contam. Hydrol.*, 38, 257-279.
- Sudicky, E.A., 1989. The Laplace transform Galerkin technique: a time-continuous finite element theory and application to mass transport in groundwater, *Water Resour. Res.*, 25(8), 1833-1846.
- Swiler, L.P., and G.D. Wyss, 2004. A user's guide to Sandia's Latin Hypercube Sampling software: LHS UNIX library/standalone version, Technical Report SAND2004-2439, Sandia National Laboratories, Albuquerque, NM.
- van Genuchten, M.T., 1980. A closed-form equation for predicting the hydraulic conductivity of unsaturated soils, *Soil Science Society of America Journal*, 44(5), 892-898.
- Wu, J., B. Hu, and D. Zhang, 2003. Applications of nonstationary stochastic theory to solute transport in multi-scale geological media, *J. Hydrol.*, 275, 208-228.

- Wu, Y.S., G. Lu, K. Zhang, G. Zhang, H.H. Liu, T. Xu, and E.L. Sonnenthal, 2004a. UZ Flow Models and Submodels, AMR Report MDL-NBS-HS-000006 REV02, Berkeley, CA, Lawrence Berkeley National Laboratory, Las Vegas, Nevada, CRWMS M&O.
- Wu Y.S., G. Lu, K. Zhang, and G.S. Bodvarsson, 2004b. A mountain-scale model for characterizing unsaturated flow and transport in fractured tuffs of Yucca Mountain, *Vadose Zone Journal*, 3, 796-805.
- Wu, Y.S., L. Pan, W. Zhang, and G.S. Bodvarsson, 2002. Characterization of flow and transport processes within the unsaturated zone of Yucca Mountain, Nevada, under current and future climates, *J. Contam. Hydrol.*, 54, 215-247.
- Wu, Y.S., and K. Pruess, 2000. Numerical simulation of non-isothermal multiphase tracer transport in heterogeneous fractured porous media, *Adv. Water Resour.*, 23, 699-723.
- Wu, Y.S., C.F. Ahlers, P. Fraser, A. Simmons, and K. Pruess, 1996. Software qualification of selected TOUGH2 modules, Lawrence Berkeley Laboratory Report, LBNL-39490, Berkeley, CA.
- Ye, M., S.P. Neuman, A. Guadagnini, and D.M. Tartakovsky, 2004. Nonlocal and localized analyses of conditional mean and transient flow in bounded, randomly heterogeneous porous media, *Water Resour. Res.*, 40(5), W05104.
- Zhou, Q., H.H. Liu, G.S. Bodvarsson, and C.M. Oldenburg, 2003. Flow and transport in unsaturated fractured rock: effects of multiscale heterogeneity of hydrogeologic properties, *J. Contam. Hydrol.*, 60, 1-30.

VITA

Graduate College
University of Nevada, Las Vegas

Feng Pan

Home Address:

1600 E. University Ave, Apt. #119
Las Vegas, NV 89119

Degrees:

Bachelor of Engineering, Hydrology and Water Resources, 2000
Sichuan University, China

Special Honors and Awards:

ACES (Advanced Computing and Visualization in Environmental Sciences)
Scholarship, NSF EPSCoR, 2005
The Aileen and Sulo Maki Hydrology/Hydrogeology Ph.D. Fellowship, Desert
Research Institute, 2005

Publications:

- Pan, F., C. Liang, Q. Fu, 2003. Evaluating Regional Water Resources Development Using a Fuzzy Matter-Element Model with the Euclid Approach, International Conference on Water-Saving Agriculture and Sustainable Use of Water and Land Resources (ICWSAWLR), Xi'an, China, p. 699-703.
- Pan, F., Q. Fu, C. Liang, 2003. Applying Fuzzy Matter-Element Model Based on AHP to Evaluate Bids of Water Saving Irrigation Project, Journal of Northeast Agricultural University (English Edition), vol.10 (2): 147-151.

Thesis Title: Uncertainty Analysis of Radionuclide Transport in the Unsaturated Zone at Yucca Mountain

Thesis Examination Committee:

Chair, Dr. Zhongbo Yu, Ph. D.
Co-Chair, Dr. Ming Ye, Ph. D.
Committee Member, Dr. Lambis Papelis, Ph. D.
Graduate Faculty Representative, Dr. Zhonghai Ding, Ph. D.